WRINKLING CONTROL IN METAL SPINNING THROUGH EDGE GEOMETRY AND PRE-STRAINING: EXPERIMENTS AND FINITE ELEMENT SIMULATION

by

Mai Van TRAN

PRESENTED TO ÉCOLE DE TECHNOLOGIE SUPÉRIEURE IN PARTIAL FULFILLMENT OF THE REQUIREMENTS FOR THE DEGREE OF DOCTOR OF PHILOSOPHY
Ph. D.

MONTREAL, JUNE 10TH 2026

ÉCOLE DE TECHNOLOGIE SUPÉRIEURE
UNIVERSITÉ DU QUÉBEC

BOARD OF EXAMINERS

THIS THESIS HAS BEEN EVALUATED

BY THE FOLLOWING BOARD OF EXAMINERS

Mr. Henri Champliaud, Thesis supervisor
Department of Mechanical Engineering at École de technologie supérieure

Mr. Zhaoheng Liu, Thesis Co-supervisor
Department of Mechanical Engineering at École de technologie supérieure

Mr. Simon Joncas, President of the Board of Examiners
Department of Systems Engineering at École de technologie supérieure

Mr. Mohammad Jahazi, Member of the jury
Department of Mechanical Engineering at École de technologie supérieure

Mr. Lyès Hacini, External evaluator
Hatch company

THIS THESIS WAS PRENSENTED AND DEFENDED

IN THE PRESENCE OF A BOARD OF EXAMINERS AND PUBLIC

APRIL 22TH 2026

AT ÉCOLE DE TECHNOLOGIE SUPÉRIEURE

FOREWORD

Wrinkling of the free flange remains one of the principal defects in conventional metal spinning, particularly in the first pass where circumferential compression develops in an unsupported rim. This thesis addresses wrinkle suppression and wrinkling prediction through a combined experimental and numerical approach centered on engineering the blank edge condition and ensuring reliable defect simulation.

The thesis is organized around three main studies. First, wrinkle suppression is investigated using pre-flanged-edge blanks, where the effect of flange geometry (angle and length) on edge rigidity and first-pass stability is assessed through experiments and finite element analysis. Second, edge pre-straining is studied through a comparative analysis of Edge Forming by Bending (EFB) and Edge Forming by Spinning (EFS), using microhardness mapping to quantify hardening footprints and simulations to interpret stability-relevant deformation histories. Third, the thesis examines numerical fidelity in explicit defect prediction by comparing loading-rate scaling and mass scaling, and evaluating how these acceleration choices influence wrinkling response and validation metrics.

This thesis is presented in the form of articles. The content reproduced from the above publications and manuscripts is included in accordance with the policies of École de technologie supérieure (ÉTS) and the permissions required by the corresponding publishers.

ACKNOWLEDGEMENTS

I would like to express my sincere gratitude to all those who contributed to the completion of this thesis. First and foremost, I am deeply thankful to my Ph.D. advisor, Prof. Henri Champliaud, for his outstanding guidance, encouragement, and continuous support throughout my doctoral studies. He has been the most influential person in my academic journey, impacting me both professionally and personally. His supervision and insightful advice were essential to the successful completion of this thesis.

I would also like to sincerely thank my Ph.D. co-advisor, Prof. Zhaoheng Liu, as well as Prof. Mohammad Jahazi and Dr. Sergio Elizalde, for their valuable advice, constructive discussions, and support over the years. My appreciation is also extended to Prof. Simon Joncas (Department of Systems Engineering at École de technologie supérieure) and Mr. Lyès Hacini my thesis committee.

I am grateful to Prof. Thien My Dao, Dr. Hoang Quan Tran, Dr. Huy Hoan Nguyen and Dr. Tan Dan Do for their recommendations, guidance, and knowledge shared during my Ph.D. journey. Their valuable and helpful advice is gratefully acknowledged.

I would like to thank Mr. Radu Romanica**,** Mr. Michel Orsini**,** Mr. Serge Plamondon, Dr. Alireza Khodabandeh and Dr. Neda Ghodrati for their technical assistance and support during the experimental work.

I also acknowledge with gratitude the financial support provided by the Natural Sciences and Engineering Research Council (NSERC) of Canada and the Program to Support Research and Innovation Organizations (PSO)., which made this research possible. I extend my sincere appreciation to my teachers and colleagues from the Department of Mechanical Engineering at Ho Chi Minh University of Technology and Education (HCMUTE), Vietnam, for their support and encouragement.

Finally, I wish to express my deepest thanks to my family, my wife, and my friends for their constant encouragement, understanding, and kindness, which were essential to the successful completion of my Ph.D. thesis.

CONTRÔLE DU FROISSAGE EN REPOUSSAGE MÉTALLIQUE PAR LA GÉOMÉTRIE DU BORD ET LA PRÉ-DÉFORMATION: ÉTUDE EXPÉRIMENTALE ET SIMULATION PAR ÉLÉMENTS FINIS

Mai Van TRAN

RÉSUMÉ

Cette thèse étudie le froissage de la géométrie formée lors de la première passe du repoussage conventionnel et évalue le préformage du bord comme une approche pratique pour améliorer la stabilité sans modifier l'objectif final de mise en forme. Le travail combine des expériences contrôlées et des simulations tridimensionnelles par éléments finis explicites, et s'appuie sur des mesures géométriques et mécaniques cohérentes afin d'établir le lien entre les paramètres du procédé, la pré-déformation et la réponse au froissage.

Un résultat majeur est la mise en évidence quantitative que l'introduction d'une bride préformée avant le repoussage peut supprimer les modes de flambage circonférentiel qui se développent sur des flans plats. Dans des conditions de repoussage identiques, la configuration à flan plat présente des plis marqués, tandis que la configuration à bord bridé demeure lisse et stable. La sévérité du froissage est évaluée à partir de données de numérisation tridimensionnelle au moyen d'une mesure d'amplitude crête à creux le long du bord, ce qui permet une comparaison directe entre les différentes conditions. Les résultats montrent également que le bénéfice de la bride dépend de la géométrie retenue, en particulier de l'angle et de la longueur de la bride, car ces paramètres gouvernent l'augmentation de rigidité du bord. Afin d'expliquer comment le préformage du bord améliore la résistance au froissage, la thèse reconstruit les champs de pré-déformation à l'aide d'une cartographie de microdureté et relie ces champs à l'évolution du champ de rigidité au voisinage du pied de bride. Des relations microdureté–pré-déformation calibrées et un plan d'échantillonnage structuré sur les paramètres du bord et la zone de courbure sont utilisés pour l'alliage AA5052-O. Le formage du bord par pliage et le formage du bord par repoussage augmentent tous deux l'écrouissage près de la bride externe, tandis que le formage par repoussage génère une zone durcie plusintense et plus étendue que le pliage. Ces différences spatiales justifient l'emploi de mesures de pré-écrouissage dans la bande de courbure pour comparer les conditions de préformage.

Une évaluation numérique complémentaire montre qu'une accélération modérée des simulations peut préserver des prédictions pertinentes pour les défauts, tandis qu'une accélération trop élevée accroît l'influence inertielle et réduit la fiabilité des résultats.

Dans l'ensemble, cette thèse fournit des recommandations fondées sur l'expérimentation pour concevoir des flans à bord conditionné et pour interpréter la stabilité en repoussage à partir d'éléments convergents issus de la géométrie, de la microdureté et de l'historique des contraintes et des déformations.

Mots-clés : Froissage, bordage, rigidité, microdureté, repoussage, LS-DYNA

WRINKLING CONTROL IN METAL SPINNING THROUGH EDGE GEOMETRY AND PRE-STRAINING: EXPERIMENTS AND FINITE ELEMENT SIMULATION

Mai Van TRAN

ABSTRACT

This thesis investigates flange wrinkling during the first pass of conventional metal spinning and evaluates edge preforming as a practical way to improve stability without changing the final forming objective. The work combines controlled experiments with three-dimensional explicit finite element simulations and uses consistent geometric and mechanical measurements to connect process design, prestrain, and wrinkling response.

A main outcome is the quantitative evidence that introducing a preformed flange before spinning can suppress the circumferential buckling modes that develop in flat blanks. Under identical spinning conditions, the flat configuration exhibits pronounced wrinkles, while the flanged edge configuration remains smooth and stable. Wrinkle severity is evaluated from three-dimensional scan data using a peak to valley amplitude measure around the rim, enabling direct comparison across conditions. The results also show that the benefit of the flange depends on the selected flange geometry, particularly the flange angle and flange length, since these parameters govern the added edge rigidity.

To explain how edge preforming improves wrinkling resistance, the thesis reconstructs prestrain patterns using microhardness mapping and links these patterns to the evolving stiffness field near the flange root. Calibrated hardness-based relationships and structured sampling across the rim and curvature region are used for AA5052-O. Both edge forming by bending and edge forming by spinning increase hardening near the outer flange, while edge forming by spinning produces a stronger and wider hardened region than bending. These spatial differences support compact scalar measures of prehardening in the curvature band to compare preforming conditions.

A supporting numerical assessment shows that moderate simulation acceleration can preserve defect relevant predictions, whereas aggressive acceleration increases inertial influence and reduces reliability.

Overall, the thesis provides experimentally anchored guidance for designing edge conditioned blanks and for interpreting stability in spinning through combined geometry, hardness, and stress and strain history evidence.

Keywords: Wrinkling, flanging, rigidity, micro-hardness, spinning, LS-DYNA

TABLE OF CONTENTS

Page

LIST OF TABLES

Page

LIST OF FIGURES

Page

LIST OF ABBREVIATIONS AND ACRONYMS

AA5052-O	Aluminum alloy AA5052 in annealed condition
Abaqus/Explicit	Explicit dynamic finite element solver (Abaqus)
CNC	Computer Numerical Control
EFB	Edge Forming by Bending
EFS	Edge Forming by Spinning
EI	Flexural rigidity (Young's modulus × second moment of area)
FE	Finite Element
HV0.1	Vickers microhardness at 0.1 kgf load (≈100 gf)
LR	Loading-rate scaling (explicit simulation acceleration)
LS-DYNA	Explicit finite element solver (LS-DYNA)
MS	Mass scaling (explicit simulation acceleration)
NTR-25	DENN NTR-25 CNC spinning machine
RRF	Rotating Reference Frame
R2	Backup-roller curvature radius level "R2"
R4	Backup-roller curvature radius level "R4"
R6	Backup-roller curvature radius level "R6"
STL	Stereolithography surface mesh file format (used for scanned geometry)

INTRODUCTION

Metal spinning is a rotary incremental forming process used to manufacture thin-walled axisymmetric parts with relatively simple tooling. A roller follows a prescribed toolpath while the blank rotates against a mandrel, and the part shape develops through repeated local contact and redistribution of membrane and bending actions. This flexibility is also the main difficulty. The process response depends strongly on the pass schedule and on how support conditions evolve as the rim is progressively engaged.

Flange wrinkling remains a dominant formability limit in conventional spinning of thin sheet blanks. As the roller advances, circumferential compression builds in the unsupported rim, and the flange can lose stability through out-of-plane buckling. Once the instability appears, the surface quality and geometric accuracy degrade rapidly, and the process window narrows. In practice, this defect is most critical during the early stages of forming, when the rim is still free and the stiffness distribution is highly non-uniform.

In this work, wrinkle suppression is approached by acting on the rim state before and during the critical stages of conventional spinning. Two edge pre-forming routes are considered. Edge Forming by Bending (EFB) and Edge Forming by Spinning (EFS) are used to introduce a hardened curvature region near the flange root. These routes are designed to modify the local resistance of the rim and to change how compressive demand is accommodated as the roller passes. The subsequent forming is then performed by conventional spinning. A key point of the study is that wrinkling cannot be interpreted reliably from a single global indicator. The instability emerges from the accumulation of compressive demand across repeated roller encounters, and the transition from recoverable cyclic behavior to irreversible compressive build-up is what signals loss of stability. This work therefore treats wrinkle suppression as a pass-resolved stability problem governed by rim reversibility. The analysis is performed separately for the first conventional spinning step and for the second step, because the rim enters the second step with a different stiffness state and deformation history. Distinguishing these two steps is essential for a clear interpretation of when and why instability is delayed.

To connect process physics to measurable evidence, the strengthened region created by EFB and EFS is characterized experimentally using microhardness mapping, which provides a spatial description of hardening intensity and extent. Finite element simulations are then used to extract per-revolution hoop stress and hoop strain histories at the rim and within the strengthened curvature region. Wrinkling onset is defined through a strain-recovery criterion that detects the first transition from within-cycle recoverable excursions to non-recovering compressive accumulation, and the associated boundary hoop compressive stress is used to track a height-dependent stability margin. These cycle-level indicators offer a way to interpret rim behavior consistently across the forming height and across the full parameter matrix. Because full three-dimensional explicit simulations of spinning remain computationally demanding, numerical acceleration is often required. Yet, when the target is wrinkling prediction, acceleration must be evaluated with defect sensitivity in mind, not only with force trends. This study therefore compares two widely used acceleration routes in explicit solvers, loading-rate scaling and mass scaling, under an identical process definition and toolpath, and validates predictions against experiments. Quasi-static fidelity is assessed using the kinetic-to-internal energy ratio, while prediction accuracy is evaluated using axial force histories together with wrinkle-related axial displacement measures, including the final axial displacement field and a peak-to-valley amplitude with peak count. The comparison shows that moderate acceleration can preserve low kinetic contribution and reproduce experimental force trends and wrinkle patterns, whereas aggressive scaling increases inertial effects and reduces reliability of wrinkle prediction.

Overall, the thesis provides a unified experimental and numerical framework to study flange stability in conventional spinning across two consecutive spinning steps, and to quantify how edge pre-forming routes and support curvature affect the transition from reversible rim response to instability. It also clarifies how force histories should be interpreted jointly with energy diagnostics and surface measures when selecting acceleration levels for explicit defect simulations.

CHAPTER 1

GENERAL INFORMATION AND THESIS ORGANIZATION

This chapter presents first an overview of the metal spinning process and secondly scope and structure of the thesis.

1.1 Background and motivation

Metal spinning is an established rotary incremental forming process for producing thin-walled, axisymmetric shells with simple tooling. Its industrial value comes from the combination of flexibility and efficiency. Many components as shown in Figure 1.1 can be manufactured on the same machine platform by changing the mandrel and the roller path. This flexibility is attractive when product families evolve, when batch sizes are small to medium, or when the cost and lead time of dedicated press tooling are not justified.

Figure 1.1 Typical components produced through metal spinning as used in both industrial and household applications

Reproduced from https://globalmetalspinning.com

From a process point of view, metal spinning forms a rotating blank by local contact with a tool that progressively forces the sheet onto a supporting form. The workpiece is clamped against the mandrel. The mandrel and blank rotate together, and the tool advances along a controlled trajectory. This setup highlights two essential features that guide any discussion of spinning. The first is that deformation is incremental, because the contact zone is small and travels with the tool. The second is that process response is history dependent, because stress and strain are redistributed around the circumference each time the roller passes.

In conventional spinning, the part is typically formed over multiple passes as illustrated in Figure 1.2. This multi-pass approach is not only a matter of productivity but also often a requirement for stability, especially for thin blanks, because the free rim is not fully supported during the early stages. The flange therefore behaves like a slender structural segment while it is being driven inward, and it must carry circumferential compressive demand as the roller advances. When this compressive demand exceeds what the rim can sustain, the rim does not fail by tearing first. It fails by losing stability and deflecting out of plane.

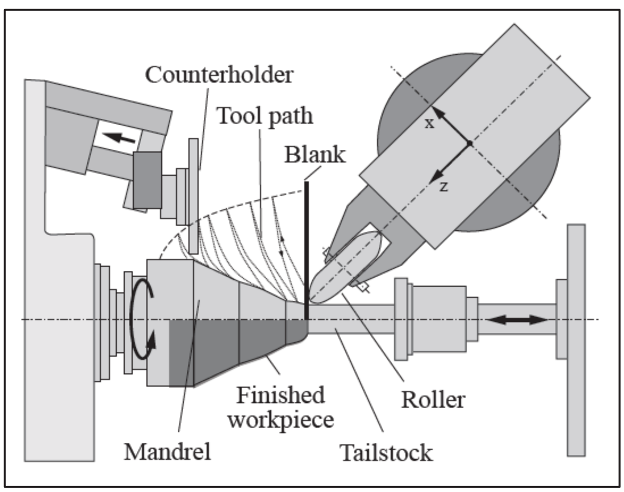

Figure 1.2 Principle of conventional spinning, showing a rotating blank clamped against a mandrel and formed locally by a tool

Reproduced from Runge (1994)

Flange wrinkling is therefore one of the most important formability issues in conventional spinning of thin sheets. It directly degrades geometric quality and can compromise subsequent forming passes, because the roller no longer interacts with a smooth, axisymmetric boundary.

A clear visual contrast between a wrinkled part and a wrinkle-free part is often enough to show why this defect matters for both research and industrial practice as presented in Figure 1.3.

Figure 1.3 Wrinkling failure versus wrinkle-free forming in conventional spinning
Reproduced from Wang (2011)

This thesis is motivated by a practical need to improve the robustness of conventional spinning when thin blanks are required. In industrial settings, avoiding wrinkling still depends heavily on experience-driven choices for pass planning and process parameters. The stability boundary can shift noticeably, even when machine-level changes appear modest. At the same time, the process is incremental and strongly history-dependent. This makes it difficult to rely on a single indicator of stability. The risk of instability is instead built progressively through repeated loading of the rim as the roller advances. Together, these observations motivate a focused study of rim stability in the early forming stages. In this phase, the flange is the most vulnerable. A clearer understanding at this stage can translate directly into more reliable process design.

1.2 Scope of the research

This thesis is limited to a two-stage forming route in which the blank edge is first conditioned and the part is then formed during the first pass of conventional spinning. The objective is to improve rim stability and suppress flange wrinkling without changing the final forming objective. The scope is therefore defined so that the three associated papers form a coherent progression from edge geometry effects, to pre-strain and hardening characterization, and finally to simulation practice required for defect-focused prediction.

1.2.1 Material, initial blanks, target geometry and geometric edge conditioning

The experimental and numerical investigations are performed on AA5052-O using thin circular blanks representative of lightweight axisymmetric spinning applications. The forming stage addressed throughout the thesis is the first spinning pass, where the flange is unsupported and wrinkling is most likely to initiate. The target parts remain within the same family of axisymmetric shapes formed by a first-pass toolpath so that stability trends can be compared consistently between conditions.

Geometric edge conditioning is introduced by pre-forming a flanged edge before spinning. This feature is treated as an intrinsic reinforcement. It increases rim rigidity. It also shifts the compressive demand away from the most unstable outer edge. Within this thesis, the geometric conditioning variables are limited to the flange angle and flange length. These parameters are used to systematically control the degree of reinforcement. The scope does not extend to a broad survey of alternative stiffener architectures or reversed flange orientations. Maintaining one consistent edge architecture is necessary. It allows first-pass behavior to be interpreted without additional boundary-condition changes.

1.2.2 Edge pre-straining routes and microhardness-based reconstruction

A second edge-conditioning approach studied in this thesis is mechanical reinforcement produced by pre-straining the edge. Two routes are considered. They are edge forming by bending (EFB) and edge forming by spinning (EFS). They are evaluated under comparable spinning objectives. This allows differences in wrinkling response to be interpreted in terms of differences in the pre-strain footprint created at the flange root and the adjacent curvature band.

To quantify this footprint experimentally, the thesis uses spatial microhardness mapping. This serves as a practical indicator of the strengthening distribution created by edge pre-forming. The mapping is performed on deformed blanks. It uses structured sampling that covers the flange region and the neighboring curvature band that are relevant to early-pass stability. The intent is to reconstruct and compare the intensity and the extent of strengthening between pre-straining routes. It is not to develop a full microstructural evolution model.

1.2.3 Explicit FE modelling, validation strategy, and numerical acceleration limits

Three-dimensional explicit finite element simulation is used as a common numerical framework across this thesis. It is used to interpret stress and strain histories associated with rim instability. It is also used to support controlled comparisons between edge-conditioning conditions. Validation is defined to include both global and defect-relevant responses. Force history is paired with surface-based wrinkle metrics extracted from post-processed geometry. In this way, simulations are judged by their ability to reproduce instability outcomes, not by force trends alone.

Full three-dimensional spinning simulations are computationally demanding. For this reason, the thesis includes a focused assessment of numerical acceleration practices used in explicit solvers. Loading-rate scaling and mass scaling are compared under an identical process definition and toolpath. Quasi-static fidelity is screened using energy diagnostics. Prediction fidelity is evaluated using the same force and wrinkling outputs used elsewhere in the thesis. This methodological component is intentionally secondary to the edge-conditioning mechanisms. It is used to establish practical acceleration levels for defect-focused predictions. It also clarifies that equal nominal scaling factors do not necessarily produce equivalent inertial content. They also do not necessarily produce equivalent wrinkling outcomes across acceleration mechanisms.

1.2.4 Key definitions and metrics used throughout the thesis

This thesis uses a consistent set of definitions and quantitative metrics. This consistency allows results from different edge-conditioning conditions to be compared on the same basis. It also allows experiments and simulations to be compared directly.

Metal spinning is understood here as a rotary incremental forming process. A clamped circular blank is progressively conformed to a mandrel. The deformation is imposed by a roller that follows a prescribed toolpath and pass schedule [Music 2010], [Wong 2003], [Xia 2014]. The focus is restricted to the first pass. This stage governs the earliest development of circumferential compression in the unsupported rim. It is therefore the most critical for instability in the studied geometries [Kobayashi 1963].

Flange wrinkling refers to the appearance of circumferential, out-of-plane undulations at the free edge during spinning. It is driven by the build-up of hoop compression. It is also influenced by the evolving stiffness of the flange as deformation proceeds [Kong 2017], [Gao 2022]. The thesis reports wrinkling state using a measurement-based classification. This classification is grounded in rim geometry. It does not rely only on qualitative observation. Wrinkle-free cases are defined by a smooth rim profile at the end of the pass. Wrinkled cases are those where the rim profile exhibits periodic circumferential patterns. These patterns must be large enough to be measured robustly. They must also persist after unloading. The classification is supported by geometric descriptors extracted from rim profiles. The same descriptors are used for experiments and for post-processed simulation geometry [Tran 2026], [Gao 2022].

Two geometric wrinkle descriptors are used throughout the thesis. The first is a peak-to-valley amplitude of the rim profile measured around the circumference. It represents wrinkle severity in a way that remains comparable across edge-conditioning conditions [Tran 2026]. The second is the number of dominant peaks around the rim. It serves as a compact indicator of wrinkle mode. It also allows pattern changes to be tracked when flange stiffness, toolpath, or numerical settings are modified [Kong 2017], [Tran 2026], [Gao 2022]. These geometric metrics are interpreted together with global responses. The primary global response is the axial forming force history. Agreement in force evolution provides a necessary baseline check. It indicates that contact and overall loading are represented consistently. This baseline is established before instability-related differences are discussed [Tran 2026].

To characterize the strengthening footprint created by edge pre-straining, the thesis employs microhardness mapping. Hardness is used as a spatial indicator of local strengthening and deformation history in the flange region. Measurements are taken on structured grids across the rim. They also cover the curvature band near the flange root. The resulting maps are reduced to band-level descriptors. These descriptors summarize both intensity and spatial extent. They are used to compare pre-straining routes under comparable spinning objectives. They are also used to connect the observed hardening footprint to subsequent wrinkling response [Wang 2012]. Hardness-based interpretation serves as a practical experimental proxy for local strengthening. It is not treated as a complete microstructural model. Its role is to support comparative reasoning across cases that share the same material condition and forming route [Gao 2022].

For numerical modelling, the thesis uses three-dimensional explicit finite element simulation as the common framework. This framework is used to predict deformation histories. It is also used to reproduce defect-relevant outcomes in spinning. The choice is consistent with established practice for large deformation, contact-dominated forming problems [Belytschko 2000], [Wang 2012]. Numerical suitability is evaluated using a validation philosophy that combines global response with defect-relevant metrics. Acceptable force levels alone are not treated as sufficient when the objective is to predict wrinkling [Tran 2026], [Wang 2012]. When accelerated explicit simulations are required, solver diagnostics and response checks are used. The goal is to ensure that predictions remain meaningful for instability. In particular, acceleration practices such as mass scaling and increased loading rate are evaluated in terms of their influence on inertia and on defect prediction reliability. This approach follows the broader forming simulation literature [Tran 2026]. The purpose of these diagnostics is to establish a defensible simulation setting for comparative studies. It is not to propose a new acceleration method.

1.3 Outline of thesis

Chapter 1 establishes the process route studied, namely edge preforming followed by conventional spinning, and defines the scope, terminology, and metrics that are used consistently throughout the thesis.

Chapter 2 reviews the background necessary to interpret the thesis results. It focuses on conventional spinning mechanics, flange instability and wrinkling criteria, edge-conditioning concepts that modify stiffness and deformation history, and explicit three-dimensional simulation practices, with particular attention to kinematic description and acceleration effects.

The core of the thesis is organized into three article chapters corresponding to the three papers. The first article chapter examines geometric edge conditioning through a pre-formed flange and its effect on wrinkling during the first spinning pass, supported by experimental measurements and simulations and interpreted using rim-profile wrinkle descriptors and stiffness-based reasoning [Tran 2026]. The second article chapter compares two edge pre-straining routes and uses microhardness mapping to reconstruct and quantify the strengthened band near the flange root, and links these differences to subsequent stability during spinning using a consistent measurement framework. The third article chapter provides supporting methodology by comparing acceleration choices commonly used in explicit simulations when computational efficiency is required, and clarifies how these choices can influence the reliability of wrinkling predictions even when global responses appear acceptable.

The final chapter consolidates the results from the three article chapters into a unified set of conclusions and recommendations. It summarizes how edge geometry reinforcement and edge pre-straining influence stability during the first pass and provides guidance for using explicit simulations responsibly when wrinkling prediction is the objective.

CHAPTER 2

LITERATURE REVIEW

Chapter 2 reviews the literature needed to frame the thesis and to interpret the experimental and numerical results reported in Chapters 3 to 5. The focus is placed on the mechanics of conventional metal spinning, with particular attention to the first pass, because this stage combines the lowest rim support with the strongest tendency for circumferential compression to accumulate in the free flange.

The review first summarizes the basic process principles and the deformation characteristics that make spinning strongly path dependent. It then discusses how flange instability develops, how wrinkling has been described mechanistically, and which analytical or semi-analytical criteria have been proposed to estimate wrinkling limits. The influence of key process and boundary-condition parameters is subsequently consolidated, since wrinkling trends reported in the literature often reflect coupled effects between toolpath, local contact conditions, and rim constraint.

Next, the chapter introduces edge-conditioning concepts that improve first-pass stability, including geometric reinforcement by preforming and mechanical reinforcement by edge pre-straining, which directly motivate the two mitigation routes studied in this thesis. Finally, the chapter summarizes investigation and modelling practices used for defect prediction in spinning, including experimental quantification of wrinkle severity and the use of three-dimensional explicit FE simulation, with attention to computational acceleration and its implications when wrinkling is the response of interest.

2.1 Conventional metal spinning and first-pass mechanics

This section introduces only the background needed to interpret flange wrinkling in the first pass and to explain why the rim is the critical region. The emphasis is on process principles, the mechanical origin of first-pass instability, and the way deformation mode and thickness evolution influence stability. The discussion is kept at a literature level and avoids repeating the experimental and modelling specifics developed later in the thesis.

2.1.1 Process principles and deformation characteristics

Conventional metal spinning is a rotary incremental forming process in which a circular sheet blank is clamped against a mandrel and shaped by a roller that follows a prescribed trajectory while the workpiece rotates. Because the roller contact is localized and migrates continuously along the surface, deformation is inherently incremental. The mechanical response is therefore governed by a combination of local contact conditions and the global constraint imposed by the mandrel and the clamping system. Comprehensive reviews describe spinning as a process where the final geometry is achieved through a sequence of localized deformation events, which makes the outcome sensitive to how the roller advances and how the pass schedule is designed rather than being determined solely by the target shape [Wong 2003], [Music 2011] [Xia 2014].

A central feature of the process is that the material under the roller undergoes coupled bending and membrane action. The roller imposes curvature changes while simultaneously driving in-plane flow that redistributes stress around the circumference and along the radial direction. This coupling explains why spinning can generate large shape changes without a closed die, but it also explains why stability limits can be reached abruptly when the unsupported flange is forced to carry compressive demand. The importance of toolpath and pass planning follows naturally from this mechanics: the trajectory determines the sequence of bending and stretching, the amount of circumferential shortening imposed per unit advance, and the redistribution of stress and strain over the flange width. Analytical frameworks developed for wrinkling prediction reinforce that the toolpath is not a secondary detail but a primary factor that defines the evolution of the stress resultants associated with instability [Li 2022].

2.1.2 First pass as the governing stability stage

The first pass occupies a special place in conventional spinning because the flange is typically most flexible and least supported at this stage. Classical work already recognized that the free rim of a spinning blank can lose stability under circumferential compression and that this instability sets a practical limit for process feasibility in conical and similar geometries [Kobayashi 1963]. Subsequent studies focused on first-pass spinning show that severe flange wrinkling can appear early when the roller feed conditions promote rapid accumulation of compressive hoop demand in a flange that has not yet developed stabilizing curvature or thickness redistribution [Kong 2017].

The literature also clarifies that the first-pass risk is not only a matter of having compression, since compression is intrinsic to drawing material inward. The key issue is whether the flange can sustain the compressive demand without converting it into an out-of-plane mode. This depends strongly on the mechanical and geometric condition of the rim. The term rim condition is used here to denote the combined state that governs the rim's resistance to out-of-plane deformation, including its local stiffness, the effective boundary condition created by support and clamping, and the deformation history already imposed on the edge. A direct demonstration that rim condition controls first-pass stability is provided by constrained spinning approaches, where additional constraint changes the effective support of the flange and expands the stable operating window for hemispherical parts [Yu 2020]. Similarly, work using flanged-edge blanks shows that modifying the edge geometry prior to spinning can suppress wrinkling under otherwise comparable first-pass conditions, which reinforces the idea that stability can be improved by conditioning the rim rather than altering the final forming objective [Tran 2026].

2.1.3 Deformation mode, thickness evolution, and stability sensitivity

A consistent conclusion across modern spinning studies is that wrinkling is tied to the evolving deformation mode of the flange and to how thickness and curvature develop during the pass.

The flange does not deform through a single mechanism; instead, the balance between bending-dominated response, membrane stretching, and in-plane flow changes as the roller progresses and as the local geometry evolves. Work that examines deformation mode and thickness variation in conventional spinning shows that thickness redistribution and curvature development are not merely consequences of forming but also contributors to the stability margin because they change the stiffness field that resists out-of-plane buckling [Gao 2022]. From this viewpoint, wrinkling should be interpreted as the outcome of an evolving structural problem in which both the compressive demand and the resistance to that demand change with the forming history.

This coupling is also apparent in modelling approaches that treat thickness evolution as part of the process mechanics. Energy-based formulations used to predict thickness variation highlight that the local work input and deformation path govern thinning and thickening trends in the contact zone and its vicinity, and these trends feed back into stiffness and stress redistribution as the pass progresses. In practice, this means that two nominally similar parts can exhibit different stability outcomes if the toolpath and pass scheduling produce different sequences of curvature development and thickness redistribution, even when the final geometry is comparable. The wrinkling prediction literature reflects this dependence by proposing models that integrate toolpath information and deformation history rather than relying solely on instantaneous stress measures [Chen 2021], [Li 2022].

For this thesis, the literature basis summarized above motivates two choices that are used consistently in later chapters. First, the first pass is treated as the governing stability stage because it combines the highest rim flexibility with rapid development of circumferential compression, and it is therefore the most direct stage at which rim conditioning strategies can be assessed [Kong 2017]. Second, stability is interpreted through combined geometric and mechanical evidence, because wrinkling is a history-dependent instability that cannot be reduced to a single force threshold or a single local variable without losing essential mechanics [Chen 2021].

2.2 Flange instability and wrinkling mechanisms in spinning

2.2.1 Mechanistic description of flange wrinkling

Flange wrinkling in conventional spinning is widely interpreted as an out-of-plane instability that occurs when circumferential compression develops in a rim region that has limited lateral support. In the first pass, the flange behaves as a relatively slender structural segment whose resistance to buckling depends on its effective bending rigidity, its boundary conditions near the contact and clamping zones, and the loading history imposed by the roller motion. Early stability treatments already framed the problem as a loss of stability of the rotating blank edge under compressive hoop stress, establishing the key idea that wrinkling is not a material failure but a structural response that emerges when compressive demand exceeds the flange's stabilizing capacity [Kobayashi 1963].

Later work focusing on first-pass spinning emphasizes that the instability is path dependent. The compressive state is not applied monotonically and uniformly. It evolves with the roller advance, local bending and unbending cycles, and the progressive development of curvature. The severity of wrinkling therefore reflects an accumulation process rather than a single instantaneous limit, which is consistent with reports of severe wrinkles forming under conditions where compression builds quickly in the unsupported region before stabilizing curvature or favorable thickness redistribution can develop [Kong 2017]. The same mechanism-based view explains why strategies that change the rim state prior to spinning, whether by increasing geometric rigidity or by altering the effective boundary condition, can suppress wrinkling under otherwise comparable forming objectives [Tran 2026], [Yu 2020]. Modern observations of deformation mode evolution and thickness variation further support the mechanistic interpretation that stability is governed by coupled geometry and stress redistribution as the pass progresses, rather than by a single scalar process variable [Gao 2022].

2.2.2 Analytical and semi-analytical wrinkling criteria

Wrinkling prediction approaches in the literature can be grouped by the physical idealization they adopt for the flange and by how they represent the evolving loading path. One family treats the flange as a structural element whose instability is governed by shell or plate-like buckling behavior under hoop compression. Within this viewpoint, the central role of rim stiffness and boundary condition is explicit, but the accuracy of predictions depends on how well the simplified model captures the actual evolution of curvature and thickness during spinning [Wang 2012].

A second family integrates the process path more directly by embedding toolpath information into the wrinkling assessment. These approaches recognize that the roller trajectory controls the history of compressive demand and the redistribution of stress resultants, which is especially important for first-pass instability. Models that couple an analytical framework with toolpath design aim to provide a practical prediction of wrinkling limits that is compatible with process planning, but they still rely on assumptions about deformation modes and stress distributions that may be challenged when the flange undergoes strong mode transitions or when the rim state is modified by preforming [Li 2022].

A third family targets robustness by combining mechanistic reasoning with calibrated or hybrid criteria. For example, more recent theoretical developments propose prediction models intended to remain reliable over broader parameter ranges by incorporating deformation features that are sensitive to wrinkling, rather than relying on a single buckling idealization. Such models can improve predictive stability windows for conventional spinning, but they still face the general limitation that wrinkling is highly sensitive to boundary conditions, local stiffness distribution, and the evolving geometry. These sensitivities become even more pronounced when the initial rim condition is intentionally altered by edge conditioning, which motivates the thesis focus on consistent metrics and comparable objectives rather than on claiming universal criteria [Chen 2021].

Across these families, the literature supports a common interpretation. Analytical and semi-analytical criteria are valuable for understanding dominant drivers and for screening process windows, but they must be used with awareness of their assumptions. They typically capture the role of hoop compression and stiffness, yet they may not fully resolve the history dependence created by incremental contact, evolving curvature, and thickness redistribution. This is one reason explicit numerical simulations are often used as a complementary tool when the goal is to interpret wrinkling mechanisms under realistic kinematics and evolving geometry, provided that validation is performed against defect-relevant measures [Tran 2026], [Wang 2012].

2.2.3 Experimental observation and quantification of wrinkle severity

Experimental studies of spinning wrinkling commonly distinguish stable and unstable outcomes by observing the rim shape after forming and, in more detailed investigations, by measuring circumferential profiles to quantify wrinkle amplitude and mode. First-pass studies reporting severe wrinkling typically describe periodic lobes around the rim that grow to a clearly detectable magnitude once instability initiates, and they relate these outcomes to forming conditions that promote compressive accumulation in the free flange [Kong 2017]. More recent investigations emphasize that the same nominal forming objective can yield wrinkle-free or wrinkled outcomes depending on the initial rim state and the deformation history, which makes comparative measurement crucial when evaluating mitigation strategies such as constrained spinning or flanged-edge blanks [Tran 2026], [Yu 2020].

Despite this progress, the literature also shows a persistent challenge. Many reported wrinkle assessments are not directly comparable across studies because measurement protocols and descriptors differ. Some works report qualitative categories, while others use quantitative descriptors such as peak-to-valley rim amplitude and the number of circumferential peaks. Differences in how the rim profile is referenced, filtered, or sampled can lead to different severity values even when the visible defect appears similar. Studies that combine experiments with numerical simulation highlight the need for defect metrics that can be extracted in a consistent way from both measured geometry and simulated surfaces, since agreement in global force trends does not guarantee agreement in instability outcomes [Tran 2026]. This motivates the thesis strategy to use consistent rim-profile based descriptors across all comparisons and to interpret wrinkle severity together with deformation mode evolution and thickness changes, reflecting the broader experimental understanding that wrinkling is an instability of an evolving flange rather than a purely geometric imperfection [Gao 2022].

2.3 Influence of key process parameters on wrinkling and deformation

The literature agrees that flange wrinkling in conventional spinning cannot be attributed to a single parameter. It emerges from how the process parameters shape the evolution of circumferential compression, how that compression is redistributed through bending and membrane action, and how the rim stiffness evolves as thickness and curvature develop. For this reason, most parameter studies report trends in terms of stability windows rather than fixed thresholds, and they emphasize interactions between toolpath, local contact conditions, and the effective boundary condition at the rim.

2.3.1 Toolpath and pass schedule effects

Toolpath and pass schedule influence wrinkling primarily by controlling the rate at which compressive demand accumulates in the unsupported flange and by controlling the time and location at which stabilizing curvature is introduced. From a mechanistic perspective, a path that imposes rapid circumferential shortening while the rim is still weakly supported tends to promote early instability, whereas a path that distributes deformation more gradually can delay the point at which compressive demand exceeds the flange’s resistance. The importance of this path dependence is consistently highlighted in review articles which treat spinning as a history-dependent process where the roller trajectory defines the evolving stress state more directly than the final geometry does [Wong 2003], [Music 2011], [Xia 2014].

In the wrinkling-specific literature, toolpath is often integrated into prediction and process planning frameworks because the local direction and magnitude of incremental deformation govern the development of hoop compression. Analytical approaches that embed toolpath information aim to translate a geometric path description into an estimate of wrinkling risk by tracking how compressive resultants evolve as the roller progresses [Li 2022]. Complementary work that develops robust wrinkling models also recognizes that stable and unstable outcomes are sensitive to the deformation history associated with the chosen pass schedule, which motivates the use of stability criteria that remain valid when the path alters thickness evolution and curvature development [Chen 2021]. Studies that examine deformation mode transitions and thickness variation reinforce this point by showing that the process does not follow a single mode throughout the pass, and that stability can change as the local balance between bending and membrane action shifts with tool progression [Gao 2022]. As a result, the literature supports a practical conclusion that toolpath is a stability lever, not only a geometric prescription.

2.3.2 Feed ratio, roller geometry and clearance effects

The second group of key parameters concerns how strongly the roller loads the flange locally and how rapidly the deformation is imposed. Feed conditions affect the incremental deformation per revolution and therefore the speed at which compressive demand and curvature changes are introduced. In first-pass studies reporting severe wrinkling, unstable outcomes are considered more likely when process settings promote rapid accumulation of hoop compression in the free flange, particularly when the flange has insufficient time or insufficient geometric evolution to develop stabilizing stiffness during the same pass [Kong 2017]. This sensitivity is reflected in broader discussions that regard feed-related variables as drivers of local strain path and stress redistribution rather than as purely productivity controls [Wang 2012].

Roller geometry contributes through contact length scale and through the distribution of bending and membrane actions near the roller. A larger effective contact region can change the degree of local bending and the spread of compressive stress, while a more concentrated contact tends to intensify local gradients. The literature, however, is not always uniform in its reported trends because roller geometry interacts with toolpath and with the level of support provided by the mandrel and clamping system. This is one reason many authors interpret parameter effects by comparing stable windows rather than attempting to rank each parameter independently. Thickness evolution models also support the idea that contact and path determine the work distribution that drives thinning and local stiffness evolution, which indirectly affects wrinkling susceptibility through the flange's evolving resistance to out-of-plane deformation. Overall, the parameter studies suggest that feed and roller geometry act through the same physical channel, which is the evolution of compressive demand and stiffness in the rim region, but the net effect can depend on the forming route and constraint conditions [Wang 2012], [Gao 2022].

2.3.3 Boundary conditions and constraint level at the rim

The third group of parameters concerns the effective boundary condition of the flange. The rim in first-pass spinning is often weakly supported, so the stability boundary is sensitive to how strongly the flange is constrained, how the blank is clamped, and whether additional support is introduced. The classical stability interpretation already implies this sensitivity because the critical buckling response of a flange depends on both stiffness and boundary condition, even when the same compressive demand is present [Kobayashi 1963]. More recent constrained spinning work makes this connection explicit by demonstrating that added constraint can suppress wrinkling and expand the feasible region for hemispherical parts, which indicates that stability limits are not only material or geometry limits but also boundary-condition limits [Yu 2020].

From a process-planning perspective, these findings mean that changing constraint level shifts stability boundaries by altering how hoop compression is distributed and how easily the flange can deflect out of plane. This also explains why studies that modify the rim state prior to spinning, either by increasing effective stiffness or by changing the edge condition, can produce substantial differences in wrinkling response under similar nominal forming objectives [Tran 2026]. The literature therefore treats boundary conditions as an essential part of any stability interpretation. It also motivates the practice of reporting wrinkling outcomes using defect-relevant measures rather than relying only on global force levels, because boundary condition changes can alter instability without producing large and easily separable differences in force history [Tran 2026], [Wang 2012].

Taken together, the literature supports the organization adopted in this chapter. Mechanistic understanding of wrinkling is necessary but not sufficient. The stability outcome depends on how toolpath, local loading conditions, and rim constraint work together to shape the evolution of compressive demand and flange resistance.

2.4 Edge conditioning concepts for improving first-pass stability

Edge conditioning is motivated by a simple stability idea that appears repeatedly in the spinning literature. First-pass wrinkling is promoted when circumferential compression develops in a flexible rim region whose out-of-plane resistance is insufficient. If the rim condition is modified before the first pass so that the same compressive demand is either reduced, redistributed, or resisted by a higher local stiffness, the onset of buckling can be delayed and wrinkle growth can be suppressed. This perspective is consistent with classical interpretations of flange instability and with more recent studies that treat stability as an outcome of the evolving rim state rather than a fixed material limit [Kobayashi 1963], [Kong 2017], [Tran 2026].

Within that broad concept, the literature can be organized into two complementary routes. One route is geometric, where the edge is reshaped to raise structural rigidity. The other route is mechanical, where a strengthened band is created near the flange root through controlled pre-straining. The present thesis positions both routes as ways to modify the initial condition of the rim prior to the first conventional spinning pass, while keeping the forming objective of the pass unchanged [Tran 2026].

2.4.1 Geometric edge reinforcement by preforming

Geometric edge reinforcement refers to any preforming step that modifies the initial edge shape so the rim behaves as a stiffer structural segment during the first spinning pass. The most direct mechanism is an increase in out-of-plane bending rigidity of the free edge region, which raises the compressive level required to trigger an unstable circumferential mode. Classical instability concepts already imply that changing the structural stiffness and boundary condition of the flange will shift the wrinkling boundary, even if the applied compressive demand is similar [Kobayashi 1963].

In practical spinning studies, geometric reinforcement is commonly implemented by introducing a flange-like preform or an edge feature that makes the rim less compliant. The effectiveness of such an approach depends on geometry variables that control the degree of structural reinforcement. Across the literature, the variables that appear most consistently are the edge angle relative to the base plane, the extent of the preformed region measured from the rim inward, and the local curvature or bend radius that defines how abruptly stiffness changes across the flange root. These variables matter because they control both the sectional rigidity of the rim and the way the rim couples to the deforming region under the roller. The same stability logic explains why constrained spinning methods can suppress wrinkling by changing the effective boundary condition at the rim, even though the edge shape is not necessarily altered in the same way [Yu 2020]. Work that demonstrates wrinkle suppression using flanged-edge blanks provides a clear example of geometric conditioning used as a stability lever for first-pass spinning [Tran 2026].

2.4.2 Mechanical reinforcement by edge pre-straining

Mechanical reinforcement focuses on altering the rim's resistance through a controlled pre-strain history introduced before the first pass. The underlying idea is not primarily geometric stiffening but the creation of a strengthened band near the flange root and adjacent curvature region. When this band is strengthened, the rim can sustain a higher compressive demand or distribute compressive stress more favorably before an out-of-plane instability develops. This concept is aligned with broader discussions in spinning reviews that emphasize incremental plastic deformation and work hardening as central to the evolving mechanical state, particularly near regions that experience repeated bending and contact-driven loading does. [Wong 2003], [Music 2011], [Xia 2014]

In the literature, the practical challenge is that pre-strain is not directly observable everywhere on the formed edge, so strengthening is often inferred through indirect indicators. Common indicators include local hardness measurements, thickness redistribution, and other spatially resolved measurements that act as proxies for deformation history. The value of such indicators is that they allow the strengthened region to be described as a footprint in space, rather than as a single average value. This becomes important when comparing different edge conditioning routes, because two routes may produce similar global outcomes but create different strengthening distributions that lead to different stability behavior during the first pass. The need to interpret rim behavior through such spatial evidence is consistent with the treatment of wrinkling as a history-dependent instability rather than a purely geometric defect [Gao 2022], [Wang 2012]. In studies that combine experiments with simulations for flanged-edge blanks, this same logic appears in the use of consistent defect metrics and global response checks to support mechanistic interpretation [Tran 2026].

2.4.3 What is still unclear for edge conditioning in spinning

Although both geometric reinforcement and mechanical reinforcement are motivated by the same stability objective, the literature often treats them as separate topics. Geometric preforming studies tend to emphasize stiffness increase and boundary condition effects, while pre-strain-oriented discussions tend to emphasize strengthening indicators and deformation history. As a result, direct comparisons between the two routes are less common, especially when comparisons require a consistent basis for wrinkling severity and a consistent way to describe the rim state that existed before the first pass [Tran 2026], [Yu 2020], [Wang 2012].

A second gap concerns the comparability of evidence. Wrinkling is frequently reported using qualitative categories or study-specific metrics, which makes it difficult to compare edge-conditioning effectiveness across different setups. At the same time, analytical prediction approaches are often developed around a particular idealization of flange mechanics or a particular process description, which can obscure how differences in initial rim condition change the deformation path and therefore the stability boundary [Chen 2021], [Li 2022]. These limitations motivate the thesis logic of evaluating edge conditioning using consistent geometric wrinkle descriptors together with consistent indicators of the strengthened region, so that geometric and mechanical reinforcement can be compared under comparable first-pass objectives without relying on incompatible metrics [Tran 2026], [Gao 2022].

2.5 Investigation techniques and modelling practice for defect prediction

The literature on conventional spinning uses three complementary evidence streams to study deformation and to predict wrinkling. Analytical models are used to interpret dominant mechanisms and to screen process windows. Experiments provide defect-grounded outcomes and calibrate what should be regarded as a meaningful stability response. Finite element simulation is used when contact, large deformation, and evolving geometry make reduced-order assumptions too restrictive. In reliable studies, these streams are not treated as interchangeable. They are combined so that simplified models guide interpretation, experiments anchor the defect metrics and simulations connect history-dependent fields to observed instability trends [Wong 2003], [Music 2011], [Xia 2014] [Wang 2012].

2.5.1 Analytical approaches used in spinning research

Analytical work in spinning typically falls into two roles. The first role is the prediction of global process response, such as approximate force levels, stress resultants, and thickness evolution under simplified kinematic assumptions. Reviews emphasize that such models help explain how the roller trajectory and incremental contact generate a coupled bending and membrane response but they also highlight that closed-form descriptions usually rely on idealized deformation modes and averaged contact conditions [Wong 2003], [Music 2011], [Xia 2014]. Energy-based formulations have been used to describe thickness variation by linking work input to deformation and by reducing the full three-dimensional contact problem to a tractable representation. These approaches are valuable for identifying tendencies in thinning and thickening and for providing a mechanistic interpretation of path sensitivity, but they generally do not aim to resolve out-of-plane instability directly.

The second role is stability assessment. Here, analytical or semi-analytical criteria treat the flange as a structural element that can buckle under circumferential compression and they seek a condition that separates stable and unstable regimes. Modern developments in this direction increasingly integrate toolpath information because the instability is driven by an evolving compressive state rather than by a single static load. Toolpath-coupled models aim to translate a planned trajectory into a wrinkling risk indicator that can be used for process planning, while robust prediction models attempt to extend reliability across broader forming conditions [Chen 2021], [Li 2022]. The limitation that remains common across these criteria is that they must assume a simplified representation of boundary conditions, deformation mode, and stiffness evolution. This makes them powerful for interpreting trends and narrowing parameter spaces, but less reliable as stand-alone predictors when the rim state is intentionally modified by preforming or pre-straining, or when mode transitions occur during the pass [Wong 2003], [Music 2011], [Xia 2014], [Wang 2012].

2.5.2 Experimental methods for spinning stability studies

Experimental investigations establish what constitutes wrinkling, how early it initiates and how strongly it develops under a given forming route. The literature commonly reports global response measures such as forming force histories alongside defect outcomes because force alone is not a sufficient indicator of stability when out-of-plane modes can grow while the overall load level remains within a typical range [Tran 2026], [Wang 2012]. For defect assessment, rim geometry is frequently inspected through circumferential profiles or surface measurements that capture the periodic character of wrinkles and provide a severity measure that can be compared across cases. First-pass studies reporting severe wrinkling use this type of evidence to link instability to conditions that promote rapid accumulation of circumferential compression in the unsupported flange [Kong 2017]. Investigations that examine deformation mode and thickness evolution rely on measurement strategies that track wall thickness variation and relate it to forming progression because thickness redistribution influences local stiffness and therefore affects stability margins [Gao 2022].

When studies aim to compare edge conditioning routes, experimental practice also extends beyond final geometry. Property indicators are often employed to infer where the edge region has been strengthened and how far that strengthening extends from the rim toward the curvature band. In the broader forming and spinning literature, such indicators are used as spatial proxies for deformation history when direct strain histories are not accessible everywhere. The key requirement, especially for stability studies, is consistency in the sampling plan and in the coordinate definition so that differences can be attributed to process variables rather than to measurement alignment or post-processing choices [Tran 2026], [Wang 2012].

2.5.3 Finite element simulation approaches for spinning

Finite element simulation is widely used in spinning because the process combines large deformation, evolving contact, frictional interaction, and strongly path-dependent loading. In this setting, explicit formulations are often adopted because they handle complex contact and incremental kinematics robustly, provided that the simulation is configured to represent quasi-static forming rather than dynamic impact behavior [Belytschko 2000]. Three-dimensional modelling becomes especially important when wrinkling is the response of interest, because instability involves out-of-plane deformation patterns that cannot be represented by axisymmetric assumptions.

The literature emphasizes several modelling choices that govern credibility. Contact treatment between roller, blank, and mandrel must maintain stable penetration control and appropriate frictional behavior over long sliding paths. Element choice and mesh strategy must balance accuracy of bending and membrane response with computational feasibility while maintaining sufficient resolution in the flange where instability initiates. Kinematic description is equally important because the roller feed, rotation, and pass scheduling define the deformation history that drives both thickness evolution and compressive stress development. These issues are often discussed in terms of good practice rather than strict prescriptions since different codes and implementations offer different contact algorithms and element technologies. The broad forming simulation literature reinforces that modelling for defect prediction generally demands stricter validation than modelling for final shape alone because small deviations in stiffness evolution or boundary condition representation can shift the predicted stability boundary [Korolakina 2025]. As a consequence, studies that combine simulation with experiments commonly validate not only global responses such as force but also defect-relevant geometric measures that reflect the wrinkling outcome [Tran 2026].

2.5.4 Computational efficiency and numerical acceleration effects

Explicit simulation of spinning can be computationally demanding because stable time steps are limited by the smallest element dimension and by the wave speed in the material. For parametric studies, acceleration techniques are therefore often applied. The literature typically distinguishes between approaches that alter inertial content, such as mass scaling, and approaches that alter the loading rate, such as time scaling. Mass scaling can reduce computational time by increasing the stable time increment, but it can also increase inertial participation and modify the balance between kinetic and internal energy, which can be critical when the response of interest is an instability phenomenon rather than a smooth deformation path [Suresh 2014]. Loading-rate changes can also affect the response because material formability and stress redistribution can be rate sensitive, even when the intended physical process is quasi-static. The broader forming literature documents that rate effects can influence deformation behavior and therefore must be treated carefully when interpreting accelerated simulations [Korolakina 2025].

Reliable practice in the literature therefore emphasizes diagnostics rather than assuming that an accelerated run remains quasi-static. Energy partitioning, especially the relative magnitude of kinetic energy to internal energy, is commonly used to judge whether inertial effects remain limited. Additional checks include monitoring numerical artifacts such as nonphysical energy contributions and verifying that global responses and defect-relevant geometric outcomes remain consistent when acceleration is varied within a moderate range. This is particularly important for wrinkling, because instability onset can shift with small changes in stiffness evolution, damping, or inertia, even when the predicted force history appears acceptable [Korolakina 2025]. From this perspective, acceleration is best treated as a controlled modelling choice that must be justified by diagnostic evidence rather than as a purely computational convenience when the objective is defect prediction in spinning [Wang 2012].

2.6 Summary and knowledge gap

2.6.1 Consolidated view of wrinkling drivers in the first pass

The literature converges on a consistent physical interpretation related to the first-pass flange wrinkling in conventional spinning. Wrinkling is an out-of-plane instability promoted by circumferential compression that develops in a rim region with limited support. The instability is not governed by a single process variable, but by the evolving balance between compressive demand and the rim's resistance, which is itself shaped by bending and membrane actions, thickness redistribution, and the progressive development of curvature during the pass [Wong 2003], [Music 2011], [Xia 2014] and [Wang 2012]. The role of rim support is repeatedly emphasized. Changes in effective boundary condition, whether through clamping, local constraint, or geometric reinforcement, shift stability boundaries by modifying how compression is distributed and how easily the flange can deflect out of plane [Kobayashi 1963], [Yu 2020]. The literature also supports the view that the instability is history dependent. Toolpath and pass planning influence the rate and location of compressive accumulation and therefore influence whether wrinkles initiate early in the unsupported stage or remain suppressed as stabilizing stiffness develops [Chen 2021], [Li 2022]. For this reason, studies that seek reliable interpretation usually combine mechanistic reasoning with defect-relevant measurements rather than relying only on global force trends [Kong 2017], [Tran 2026].

2.6.2 Gaps in edge conditioning knowledge for spinning

The literature provides multiple routes for improving first-pass stability, but two limitations remain when edge conditioning is considered as a deliberate preforming strategy. First, geometric reinforcement and mechanical reinforcement are commonly treated in separate studies. Geometric strategies are usually discussed in terms of increased rim rigidity and modified boundary conditions, while mechanical strategies are discussed in terms of strengthening indicators and inferred pre-strain histories. The absence of a unified comparison framework makes it difficult to distinguish whether stability improvements come primarily from geometry, from strengthening, or from their coupled effect on the stiffness distribution near the flange root [Tran 2026], [Yu 2020].

Second, even when the same stability goal is pursued, the evidence used to compare outcomes is often not fully consistent across studies. Wrinkling is frequently classified using qualitative outcomes or study-specific severity measures, and strengthening is sometimes inferred from local indicators without a clear spatial footprint description. This limits the ability to compare edge-conditioning routes under comparable spinning objectives and to generalize findings into design guidance. The literature therefore indicates a need for a comparison approach that uses consistent defect metrics extracted from rim geometry together with consistent spatial descriptors of the strengthened band near the flange root, so that geometric and mechanical reinforcement can be evaluated on the same basis [Kong 2017], [Tran 2026], [Wang 2012].

2.6.3 Gap in simulation practice for wrinkling prediction

Three-dimensional explicit FE simulation is widely used to study spinning because it represents large deformation and complex contact robustly, but the literature offers less consolidated guidance when simulation is accelerated for efficiency and the response of interest is wrinkling. In many forming applications, acceleration is justified using force agreement or general quasi-static checks. For wrinkling, however, the instability boundary can shift even when global force trends remain similar, because small changes in inertia participation, stiffness evolution, damping, or boundary condition representation can alter the growth of out-of-plane modes [Korolakina 2025]. This creates a gap between what is commonly checked for computational efficiency and what is required when the objective is defect prediction. The literature supports the need for diagnostic practices that explicitly judge whether acceleration preserves defect-relevant behavior, rather than assuming that a reduced runtime solution remains predictive once force curves appear reasonable [Tran 2026].

2.6.4 How Chapters 3 to 5 address the gap

The gaps identified above are addressed in this thesis through three consecutive article chapters built on a common process route, namely edge conditioning followed by conventional spinning under comparable first-pass conditions. Each chapter addresses a specific part of the problem, while maintaining a consistent experimental and numerical basis so that the results can be interpreted together rather than as isolated case studies. This organization follows the general thesis structure stated in Chapter 1 and the foreword, where the work progresses from geometric edge reinforcement, to mechanical reinforcement by pre-straining, and finally to simulation practice for defect prediction.

Chapter 3 addresses the first gap by establishing the effect of geometric edge conditioning on first-pass wrinkling. It examines pre-flanged-edge blanks through controlled experiments and finite element simulations, with particular attention to flange angle, flange length, wrinkling patterns, axial force response, hoop stress distribution, thickness variation, wrinkle amplitude, and bending rigidity. In this way, Chapter 3 provides the geometric baseline of the thesis and shows how modifying the rim shape before spinning can improve stability without changing the final forming objective.

Chapter 4 addresses the second gap by examining mechanical reinforcement through edge pre-straining. It compares EFB and EFS under comparable spinning conditions and uses microhardness mapping, curvature-band descriptors, and finite element strain-history extraction to characterize the strengthened region created near the flange root. This chapter then links that strengthened region to wrinkling initiation through a pass-resolved framework based on irreversibility of hoop strain, boundary hoop stress, wrinkling safety margin, and recovery behavior. As a result, Chapter 4 goes beyond geometric reinforcement alone and clarifies how strengthening intensity and spatial extent contribute to the stability response.

Chapter 5 addresses the third gap by focusing on simulation credibility for wrinkling prediction. It compares loading-rate scaling and mass scaling in explicit three-dimensional finite element simulation using a common model, common validation basis, and defect-relevant outputs. The assessment includes quasi-static fidelity, axial force agreement, wrinkling onset descriptors, and final displacement morphology. This chapter therefore establishes practical guidance for using accelerated simulations efficiently while preserving confidence in instability prediction, which is essential when wrinkling rather than only global forming response is the target of the analysis.

Taken together, Chapters 3 to 5 close the knowledge gaps identified in the literature by moving from geometric conditioning, to pre-strain-induced strengthening, to reliable simulation practice, all within a unified spinning framework. The chapters therefore convert the literature understanding of flange instability into experimentally anchored and numerically supported guidance for the design and assessment of rim-conditioning strategies in conventional spinning. [Tran 2026], [Wang 2012].

CHAPTER 3

WRINKLE SUPPRESSION IN METAL SPINNING USING FLANGED-EDGE BLANKS: EXPERIMENTS AND FINITE ELEMENT ANALYSIS

Mai-Van Tran, Henri Champliaud, Zhaoheng Liu, Sergio Elizalde, Mohammad Jahazi

Department of Mechanical Engineering, École de technologie supérieure,
1100 Notre-Dame Ouest, Montréal, Québec, Canada H3C1K3

Article published in *International Journal of Advanced Manufacturing Technology* vol. 142 (2026), available at https://doi.org/10.1007/s00170-026-17438-6

3.1 Abstract

Wrinkle formation is a common defect in metal spinning, particularly during conventional spinning processes. This study investigates the use of a flanged-edge blank to prevent wrinkles by increasing the blank's edge rigidity. The process forms an angled flange along the blank's periphery with a spinning roller before performing the first pass of conventional spinning. Finite Element simulations were conducted to evaluate how flange geometry influences wrinkle initiation, and corresponding experiments compared flanged-edge blanks to flat blanks. Analytical calculations of the blank's second moment of inertia indicate that adding a flange significantly increases bending stiffness. Larger flange angles and longer flanges redistribute material farther from the neutral axis, thereby elevating bending rigidity and raising the critical compressive stress threshold for buckling, which is consistent with classical plate buckling theory. Simulations and experiments confirmed that flanged-edge blanks with a 30° flange angle remained wrinkle-free, whereas flat blanks under identical conditions suffered severe wrinkling. The flange angle emerged as a key parameter in achieving the necessary rigidity and structural stability to suppress wrinkles. Overall, the results confirm that the spinning flanging technique is an effective method to improve conventional metal spinning processes, with significant potential for broader industrial applications.

Keywords: spinning flanging, flat blank, flanged-edge blank, bending stiffness, wrinkling

3.2 Introduction

Conventional spinning is an incremental sheet metal forming process that allows to produce hollow-axisymmetric components. In conventional metal spinning, one of the main defects is the formation of wrinkles along the blank's flange. The occurrence of wrinkles in spinning can be understood as a form of instability or plastic buckling in the sheet metal flange [1].

Flange wrinkling is a well-recognized problem in conventional metal spinning, often limiting the formability and quality of spun parts. As material is driven inward and upward by the roller, the flange experiences hoop compression due to the reduction in circumference, as well as radial stretching and bending [2]. Flange wrinkling initiates when compressive hoop stress exceeds the material's resistance to buckling [3]. This resistance is given by the flange's bending stiffness, characterized by thickness, diameter, elastic modulus and yield strength [4]. Once the flange cannot withstand the compressive load, it yields by buckling out of plane [5]. In essence, wrinkling is a plastic buckling failure mode where the sheet folds onto itself in a series of waves [6]. Wang [7] observed that wrinkling is induced by the formation of a plastic hinge near the roller and blank edge, indicating the flange has started to buckle locally, so if the process continues, these instabilities can develop into heavy wrinkles that ruin the part.

Given the detrimental impact of wrinkles, many researchers have explored different ways to delay wrinkling.

Firstly, increasing blank thickness or adopting dual-material strategies directly elevates the bending rigidity of the workpiece, thereby enhancing its resistance to buckling instability [8–10]. A higher feed ratio promotes greater compressive strain on the flange per revolution, hastening instability, whereas a lower feed ratio spreads deformation more gradually, decreasing the tendency to wrinkling [8]. Xu [9] and Li [10] demonstrated that thicker blanks or composite structures effectively reduce wrinkling by enhancing material stiffness; however, this approach inevitably results in higher material costs, increased weight, and complicates downstream manufacturing steps.

Secondly, Kleiner [11] presented that wrinkling is highly dependent on the diameter-to-thickness ratio. They showed that a larger diameter-to-thickness ratio is more susceptible to wrinkling. Experimental observations by Xia [12] confirmed that wrinkling tendency increases as thickness decreases or as feed ratio increases. However, this approach inevitably results in higher material costs, increased weight, and complicates downstream manufacturing steps.

On the other hand, Wang [13] reported that carefully designed roller paths significantly improve the uniformity of thickness distribution, reducing critical stresses. Similarly, Watson [14] employed the Box–Behnken design to quantify the influence of roller path parameters on wrinkle formation, highlighting the effectiveness of optimized processing routes. Russo [15, 16] further emphasized advanced tool-path design principles, reinforcing the critical role of optimized roller trajectories in controlling wrinkling defects. Nevertheless, these methods may increase production cycle times, and achieving consistent wrinkle-free outcomes remains challenging with thinner materials.

Another class of wrinkle mitigation techniques involves the use of auxiliary supports or devices to constrain the flange. Khaled [17] introduced a deep spinning technique incorporating a blank holder with constant clearance to improve formability and reduce wrinkling. This method constrained the flange throughout the process, ensuring a uniform deformation. While effective, the approach required a dedicated setup, and the altered stress state introduced a different failure mode which the flange can jam at extremely high feed ratio. Yu [4] proposed a flange-constrained spinning technique. One or more backup rollers support the flange during hemispherical spinning of aluminum-alloy parts. Constraining the flange on one or both sides increases its effective stiffness and delays or prevents buckling. Simulations and experiments showed large gains in spinnability. The rollers counteracted the flange’s tendency to wrinkle. However, coordinating an auxiliary roller with the main forming roller increases machine complexity. The flange must remain accessible, so some part geometries cannot accommodate a support roller. The method also has drawbacks. A single backup roller delays wrinkling but does not eliminate it under aggressive parameters; wrinkles reappear once compressive stress builds. Dual opposing rollers prevent wrinkling more effectively, but they impose high through-thickness tension and strong circumferential restraint. Parts then fail by cracking rather than wrinkling. In short, over-constraint suppresses wrinkles but can induce axial splitting when the material cannot accommodate the imposed deformation.

This study demonstrates that a pre-flanged blank enables wrinkle-free conventional spinning within clearly defined operating windows and to explore the underlying mechanisms using Finite Element (FE) simulations and experimental trials. By evaluating flanged-edge blanks against flat blanks, this research examines wrinkle formation, stress patterns, and material flow across different spinning conditions. This work contributes a practical technique for wrinkle-free spinning and offers new insights into wrinkling mechanics by showing how blank geometry modifications enhance material stability. The findings aim to advance manufacturing practices and theoretical understanding of sheet metal forming instabilities.

3.3 Materials and methods

3.3.1 Material and mechanical characterization

The material selected for this investigation was aluminum alloy AA5052, which underwent an annealing heat treatment at 412°C for a duration of 2 hours, followed by air cooling. To determine its mechanical properties, uniaxial tensile tests were conducted according to the ASTM-E8/E8M standard geometry, utilizing a universal tensile testing machine. Three tensile specimens were prepared and tested to ensure reproducibility and reliability of results, as depicted in Figure 3.1a and Figure 3.1b. The resulting true stress-true strain curves for the three specimens, illustrated in Figure 3.1c, provided the basis for deriving key mechanical properties, including the yield strength, ultimate tensile strength, and strain-hardening behavior. The consistency of the curves across the three specimens confirmed the reliability of the experimental setup and material preparation.

To model the plastic deformation behavior of AA5052-O, the Hollomon strain-hardening law was adopted, as described by Equation (3.1)

$$\sigma = K\varepsilon^n \tag{3.1}$$

where σ is the effective stress, K = 356.85 N/mm^2 is the strength coefficient, ε represents the effective strain and n = 0.2926 is the strain-hardening exponent. These parameters were validated by plotting the fitted Hollomon curves against the experimental true stress-true strain data, as shown in Figure 3.1c. For FE simulations, the AA5052-O alloy was modeled as a homogeneous and isotropic material to simplify the analysis while capturing the essential mechanical behavior. The elastic response was defined using Hooke's law, with Young's modulus E = 70 GPa and Poisson's ratio ν =0.33 determined from the initial linear portion of the stress-strain curves.

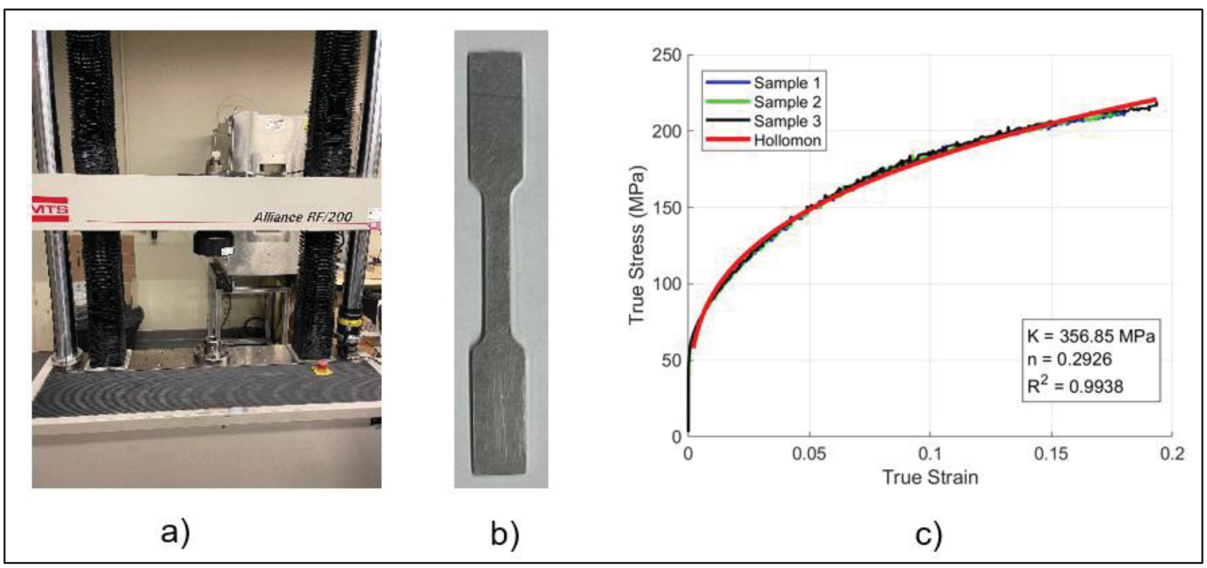

Figure 3.1 Tensile test of aluminum alloy AA5052-O

a) Tensile testing machine; b) tensile sample; c) true stress – true strain curve

3.3.2 Experimental setup and procedures

All spinning experiments were performed on a DENN NTR-25 two-axis CNC spinning machine at room temperature, as shown in Figure 3.2a. The horizontal lathe is equipped with a primary forming roller and a retractable back-up roller. The retractable backup roller shown in Figure 3.2 is used only during the pre-flanging operation to form the prefabricated rim. It is retracted prior to the conventional spinning pass, which is conducted without active flange restraint.

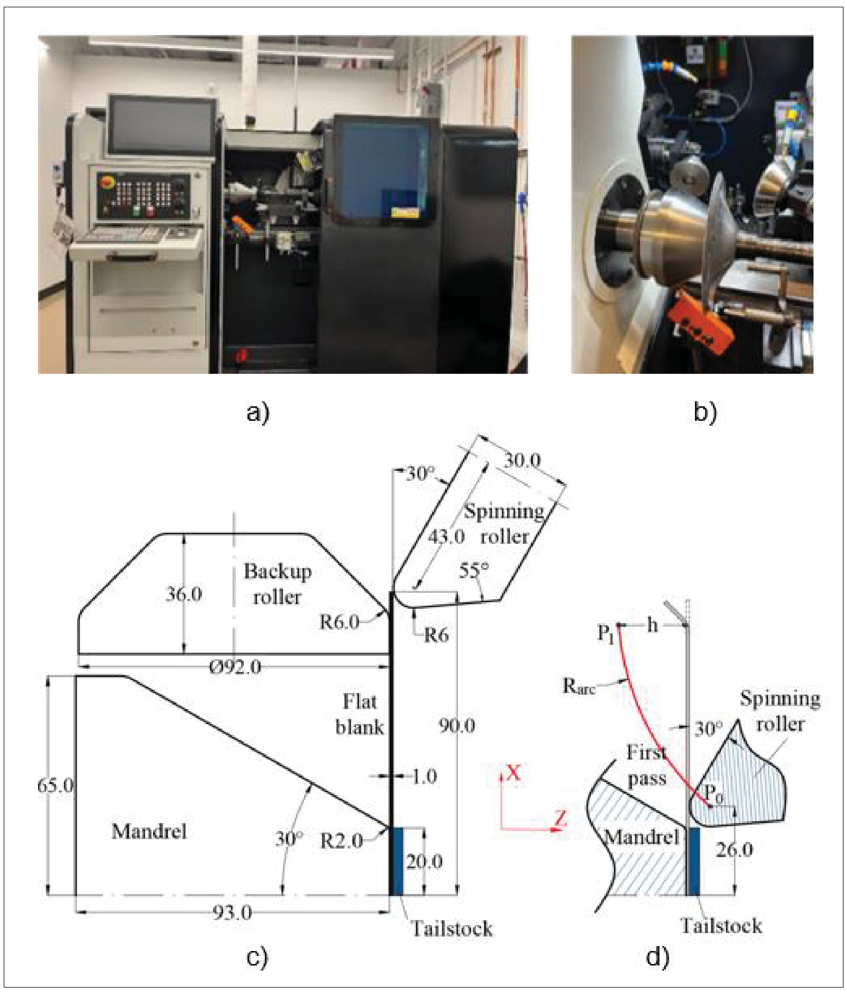

Figure 3.2 Set up for experiment a) Horizontal spinning machine NTR-25;
b) tools for experiments; c) set up for spinning flanging operation;
d) conventional spinning of flat blank or flanged-edge blank

The pre-flanged rim is oriented toward the headstock or mandrel in Figure 3.2d**.** This configuration improves first-pass stability on the present machine and avoids early roller–edge interference during initial engagement. The opposite orientation is often used for very large shells when auxiliary supports are available to flatten or restrain the rim during diameter reduction. The present study focuses on wrinkle suppression in the first pass through geometric stiffening, introduced by a prefabricated edge without additional restraint. Although the current work employs a flange produced by the selected pre-forming step, the key requirement is the existence of a stiffened edge, rather than a specific manufacturing route. Comparable edge stiffeners can be introduced by other established forming operations, such as bending-based flanging, incremental flanging, or rim beading and hemming. These alternatives are not examined here in order to keep one consistent edge architecture and one orientation for the first-pass analysis. Their influence, together with reverse orientation, is therefore identified as a direction for future study.

Circular blank discs of 180 mm diameter and 1.0 mm thickness were cut from AA5052 by laser. Each blank was centered on a steel mandrel and clamped against the mandrel face with the tailstock, ensuring a secure hold and preventing slip during rotation.

The process parameters were kept constant for all trials to enable consistent comparisons. A single-pass tool path was used for each stage of forming. For the flanging stage (pre-forming the flange), the spindle speed was set to 400 rpm. For the subsequent conventional spinning stage, the spindle speed was 200 rpm. In both stages, the roller feed ratio was 1 mm per revolution. Figure 3.2c and Figure 3.2d show the initial setup positions of the tools for the flanging operation and the conventional spinning pass, respectively. A lubrication oil was applied to the blank and tool surfaces to reduce friction and wear during forming, reflecting typical industrial practice. Throughout each experiment, the axial forming force was recorded by the machine's built-in load sensor and logged via DENN Data acquisition software. These force measurements were later used to compare the FE model results with the measured force–displacement curves.

3.3.3 Flanging operation and parameterization

To improve the blank's resistance to wrinkling, a spinning-flanging operation was conducted as a separate pre-forming step before the subsequent conventional spinning pass. In this study, the conventional spinning stage is limited to the first pass, where wrinkling typically initiates. The prefabricated rim is therefore introduced to increase edge rigidity and stabilize the flange during this first-pass deformation. In this flanging operation, an outward flange was formed around the blank's circumference by a dedicated spinning step. The procedure, illustrated in Figure 3.3, involved two sequential stages.

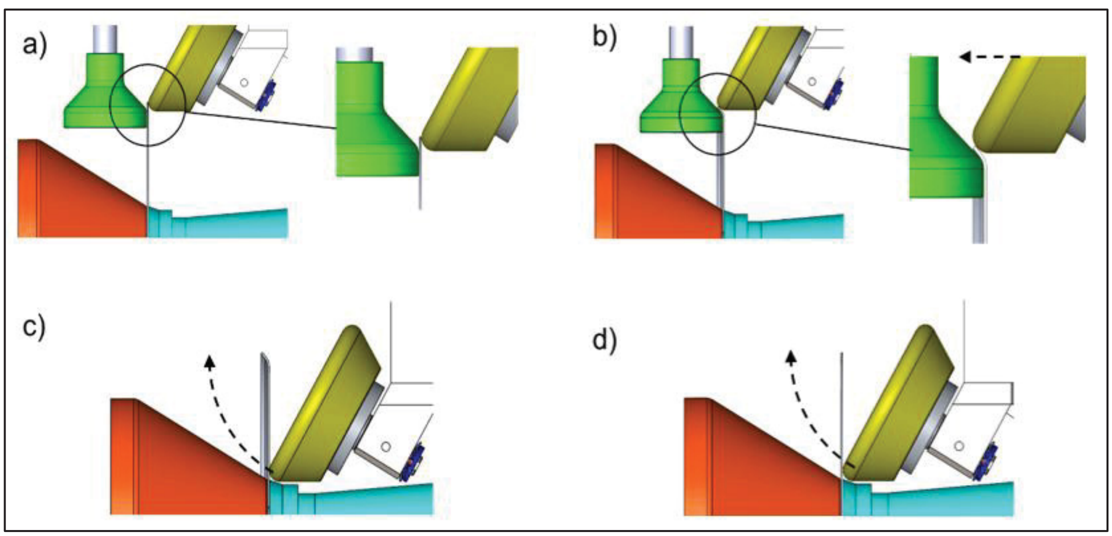

Figure 3.3 Two-step conventional spinning; a) Initial state of flanging, b) end-state of flanging, c) conventional spinning of a flanged-edge blank and d) conventional spinning of a flat blank

First, the blank's outer edge was gradually bent outward against a rounded back-up roller to create an inclined flange as presented in Figure 3.3a and Figure 3.3b The spinning roller pushed the material outward and backward, wrapping the edge of the blank around the curvature of the back-up roller to the desired flange angle. Next, the back-up roller was retracted, and the part underwent a conventional spinning pass as shown in Figure 3.3c. In this second stage, the main roller pressed the pre-formed flange inward and downward against the mandrel, continuing the shaping process. For reference, a baseline trial was also conducted in which a flat blank (with no pre-formed flange) was subjected to the same conventional spinning pass as illustrated in Figure 3.3d. This baseline allowed a direct assessment of how the flanged edge influences wrinkling under identical spinning conditions. It is noted that the material displaced into the flange is not removed from the blank. Instead, it remains an integral part of the workpiece. During subsequent passes, this material is progressively incorporated into the final geometry of the part, thereby preserving both volume and thickness distribution.

3.3.3.1 Flange geometry parameters

The geometry of the flange created in the first stage can be described by three key parameters such as the flange angle α, the flange length ρ, and the remaining unflanged length δ. These are depicted in the schematic of Figure 3.4. The flange angle is defined as the angle between the formed flange and the plane of the original flat blank (effectively, the inclination of the flange). The flange length refers to the radial length of the bent portion (measured along the blank from the bend initiation point to the outer edge of the flange). The remaining unflanged length denotes the width of the flat region of the blank that is left undeformed at the flange's base, between the end of the flange and the point of contact with the roller at the completion of flanging. Maintaining a small unflanged margin is important for process stability because if the roller were to work all the way to the exact edge of the blank, the lack of any supporting material could lead to edge instability or defects (such as splits or burrs). In the setup, δ was chosen such that point C, the roller's contact point at the end of the flanging stroke, was slightly inboard from the blank's true edge, ensuring the outermost rim was not directly impacted.

To achieve a precise flange geometry, careful coordination of the tool path was required. The center of the roller nose was used as a reference to control the roller position throughout flanging. Knowing the target flange angle α and flange length ρ, the initial coordinates of the roller (prior to contact) were calculated so that the roller would follow a path resulting in the desired flange. This calculation assumed that the flange's final dimensions (ρ and δ)

would remain essentially unchanged after springback. Geometric relations were derived to relate the flange angle and length to the roller's path and the backup roller geometry (Figure 3.4). In particular, the roller's starting position (point M) was set such that the roller's nose would end at point N (the final contact position) corresponding to point C on the blank when the flange angle reached α. Variables such as the roller nose radius (6 mm), the radius of curvature of the flange (governed by the backup roller diameter), and the sheet thickness (1 mm) were accounted for in these calculations. This analytical approach ensured that the flange was formed to the intended specifications and that the transition into the remaining flat portion was smooth and controlled.

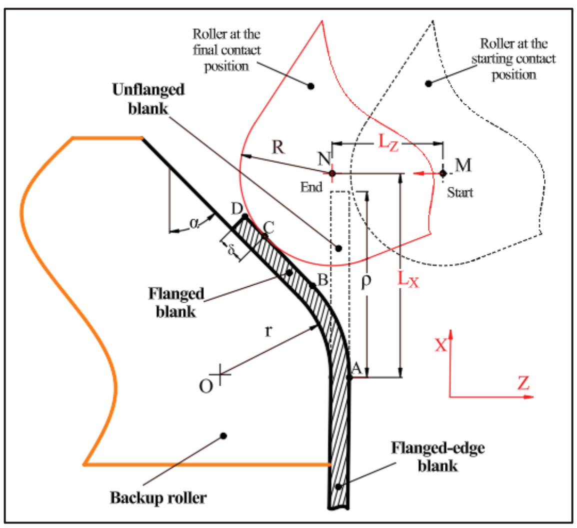

Figure 3.4 Parameters of the flanging operation

To simplify the calculation of the initial position of the roller based on the parameters α, ρ and δ, it is assumed that the flange length and free-end length of the flange remain unchanged after flanging. The equations to derive the initial coordinates of the roller's position along the X and Z axes are given by Equations 3.2 and 3.3

$$L_Z = (R + r + t) \cdot (1 - \cos\alpha) + (\rho - \delta - (r + t) \cdot \alpha) \cdot \sin\alpha \tag{3.2}$$

$$L_X = (R + r + t) \cdot \sin\alpha + (\rho - \delta - (r + t) \cdot \alpha) \cdot \cos\alpha \tag{3.3}$$

where ρ denotes the distance measured in the X direction from the edge of the blank to either the roller's contact point or the center O of the backup roller's curvature, δ is the remaining distance after the spinning flanging process, α denotes the flange angle, R is the roller nose radius, r is the radius of curvature of the flanged blank, and t is the thickness of the blank. M and N represent the roller's center at the initial and final contact positions, respectively. These equations capture the geometric interactions and spatial relationships between the roller and the flanged blank, enabling precise control over the flanging operation. By adjusting α , ρ and δ , the flange geometry can be tailored to optimize the blank's stiffness.

3.3.3.2 Flange parameter selection

A range of flange angles and lengths was explored in this study to investigate their effect on wrinkle prevention. Preliminary trials indicated that very shallow flange angles (below about 25°) do not provide a significant increase in edge rigidity. In fact, a blank flanged at 20° still exhibited wrinkling behavior similar to a flat blank, suggesting that 20° is near the lower threshold for effectiveness. Therefore, flange angles of 30° and above were the focus for achieving a wrinkle-free outcome. The 20° case was retained as a reference to illustrate the onset of instability at low flange angles. Seven flange angles were tested in total: 20°, 25°, 30°, 45°, 60°, 75°, and 90°. Similarly, the flange length must be sufficient to boost the blank's bending stiffness, but an excessively long flange can introduce its own issues. Flanges shorter than approximately 8 mm added only minimal bending resistance (insufficient to counter wrinkling), whereas flanges longer than about 14 mm would modify considerably the target geometry. Extremely large flanges would also require modified tooling and add complexity. Accordingly, the analysis focused on flange lengths of 8 mm, 10 mm, 12 mm, and 14 mm. Throughout these trials, the remaining flat length was kept constant at a small value to avoid edge effects, and the same was used for all flange geometries to ensure a consistent basis for comparison. According to Rentsch [18], when the roller moves toward the rim, the local stiffness decreases dramatically compared with the central region. As a result, the flange may bend excessively, producing a local cup-away effect that can compromise part quality if it becomes severe. The 14mm-flange-length served as the practical upper limit for our blank thickness; in general, for thicker or thinner blanks, the maximum useful flange length may be adjusted since the propensity for wrinkling and buckling is thickness-dependent. By systematically varying α, ρ and δ within these ranges, the experimental design isolated the influence of flange geometry on the spinning process outcomes.

3.3.4 Conventional spinning trials

After the flanging operation was completed for a given blank, a first pass of conventional spinning was performed. In this stage, the blank whether pre-flanged or flat was spun against the mandrel using the primary roller following a standard one-pass tool trajectory.

The present study focuses on the first conventional spinning pass, where wrinkling typically nucleates. Accordingly, a single-pass toolpath is used for each stage to isolate the effect of the prefabricated edge on first-pass stability. Multi-pass diameter-reduction scheduling for thickness control is not evaluated in the present dataset and is identified as future work. Both the flanged-edge blanks and the flat blanks were subjected to identical spinning parameters so that their performance could be directly compared. For the flanged-edge blank, the presence of pre-formed flange altered the deformation behavior during this pass. Initially, flanged blank can be conceptually divided into three regions including the peripheral flange itself, a curved transition zone connecting the flange to the rest of the blank and the remaining inner region of the blank which was still flat and unformed after the flanging step. The conventional spinning pass needed to draw the flange and transition region in against the mandrel and then continue to deform the inner region to achieve the desired final shape. A tailored roller path was used to accomplish this smoothly. As illustrated in Figure 3.2d, the roller followed a circular arc path when shaping the blank. The path was defined by a starting point at the flange's tip and an ending point near the mandrel, with the roller moving along an arc of radius 80 mm. This arc path led to a vertical displacement of h = 30 mm by the end of the pass. This displacement was chosen to reach the intended geometry without overstressing the flanged region.

3.3.5 Finite element modeling

To gain further insight into the process and to predict wrinkle formation, a detailed FE model of the two-stage spinning process was developed. The simulations were carried out using LS-DYNA, employing an explicit dynamic time-integration scheme. The FE model was designed to closely match the experimental setup, including both the flanging and conventional spinning stages.

3.3.5.1 Model setup and element selection

The blank was modeled with solid elements to capture through-thickness stresses and bending behavior. An eight-node hexahedral element formulation was used for the blank. To accurately represent bending and avoid artificial stiffness, the blank thickness was divided into three element layers. The blank's in-plane mesh was refined in critical areas to resolve the wrinkling deformations. To simulate the clamping condition at the blank's center, a 34 mm diameter circular hole was introduced at the center of the FE model blank. All nodes along the edge of this hole were fixed. This hole diameter is slightly smaller than the actual clamped area with 40 mm, ensuring that the fixed nodes cover the entire contact region. Omitting the very center of the blank in the model also allowed a higher mesh quality in that low-deformation zone, which improves computational efficiency. The spinning mandrel and both rollers were modeled as rigid bodies. The motion of the tools in the simulation replicated the experimental process.

Contact interactions between the blank and the tools were defined using a surface-to-surface contact algorithm with a Coulomb friction model. To reflect the lubricated conditions of the experiments, low friction coefficients were assigned at the interfaces. A distinction was made between the mandrel–blank contact and the roller–blank contacts. The mandrel–blank interface was given a friction coefficient of $\mu = 0.2$, representing a slightly higher friction to prevent slipping of the blank on the mandrel. The interfaces between the blank and the forming roller, and between the blank and the backup roller, were assigned $\mu = 0.01$. These lower values simulate a well-lubricated contact for the sliding of the blank.

3.3.5.2 Mesh density and regions

An adaptive meshing strategy was employed to balance accuracy and computational cost. Following the approach of Nguyen [19], the blank was divided into two concentric radial regions with different mesh densities. The inner region extended from the center of the blank up to the start of the flange area (this covers the main deformation zone in conventional spinning). This inner zone L_B was meshed with relatively coarser elements in the radial direction (r) with 32 elements between the center and the flange base but a bias factor of 3 was used to gradually decrease element size toward the outer edge. The outer region of the blank corresponded to the flange and the immediately adjacent material. This zone (of length equal to the flange length plus the small remaining flat length) was meshed more finely, with 12 elements across that width L_C. A bias factor of 1.5 was applied in this outer zone to further refine the elements toward the extreme edge. In the circumferential direction θ, 180 divisions were used and the elements were arranged uniformly around the circumference. The mesh layout is illustrated in Figure 3.5. This meshing scheme provided high resolution in the critical flange area to capture wrinkling phenomena.

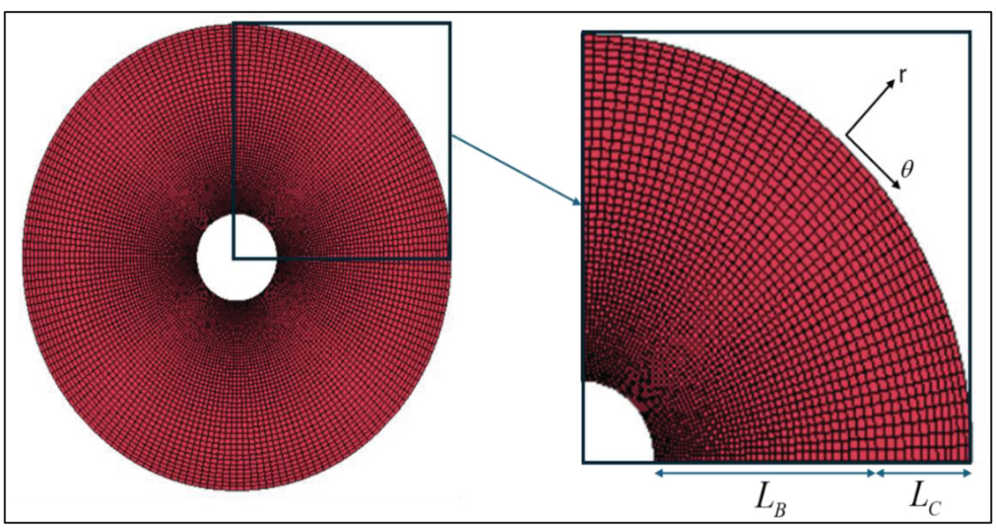

Figure 3.5 Meshing technique

3.3.5.3 Simulation procedure and loading rate scale

In the initial analysis, the flanging operation was modeled, with the mandrel and blank rotating around the central axis as the forming roller traced a designated toolpath to form the flange against a fixed backup roller. Upon completion of the flange, the first analysis was terminated, and the deformed blank's mesh, incorporating plastic strains, stresses, and geometry, was exported. For the second analysis, this deformed blank was imported as the starting point for the conventional spinning pass. The blank remained stationary in a non-rotating reference frame, with the forming roller moving radially, and no backup roller present. The spinning simulation was configured to ensure quasi-static deformation, minimizing inertial effects. To improve computational efficiency, a loading rate scaling technique was applied, increasing the roller feed speeds in the FE model by a factor of 10 to reduce simulation duration [20]. This method assumes rate-independent material behavior, ensuring deformation results remain unaffected by the increased speed. By avoiding conventional mass scaling, which artificially raises element density and may distort outcomes [19], simulation accuracy was preserved. All simulations utilized an explicit dynamics solver in LS-DYNA, with a stable time step automatically determined by the smallest element size. Outputs such as displacement fields, thickness variations, and wrinkle profiles were post-processed for direct comparison with experimental results.

3.3.6 Measurement of thickness after conventional spinning

After spinning trial, the wall thickness distribution and any wrinkling of both flanged-edge blanks and flat blanks were measured to quantitatively assess the effects of the flange. A Hexagon portable coordinate measuring arm equipped with a high-resolution laser scanner was used for this purpose as shown in Figure 3.6a. Each spun part was scanned on both the interior and exterior surfaces, producing a dense three-dimensional point cloud of the entire geometry.

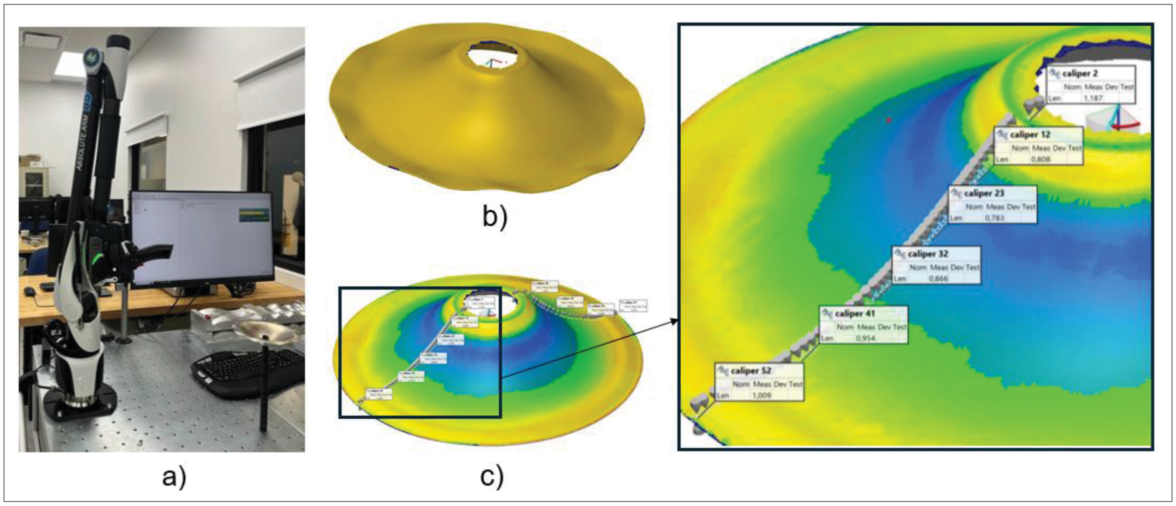

Figure 3.6 Measurement of thickness

a) Laser scanner machine, b) Flat spun part and c) Flanged-edge spun part

The scan data captured fine details of the part's shape, including local thickness. To extract the wall thickness, cross-sectional slices were taken through the point cloud at several radial positions. Specifically, at predefined radial distances from the center, the coordinates of the inner and outer surface points were used to calculate the local sheet thickness. The measurement for evaluating the thickness along a radial line on both a conventional flat spun part and a flanged-edge spun part is illustrated in Figure 3.6b and Figure 3.6c respectively. These experimental thickness profiles were then compared to the thickness predictions from the FE simulations.

In addition to thickness, wrinkle amplitude was measured to quantify the severity of any wrinkling around the flange region. Using the 3D scan data, the circumferential contour of the part's edge was analyzed. If wrinkling was present, the flange or rim of the part would exhibit a wavy profile around the circumference. To measure this, a circular path corresponding to the flange's approximate location was extracted from the point cloud. The deviations of the flange in the axial direction were then evaluated. The difference between the highest peak and the deepest valley of the wavy edge essentially the peak-to-valley height of the wrinkles was computed as h_W , an indicator of wrinkle intensity as shown in Figure 3.7b.

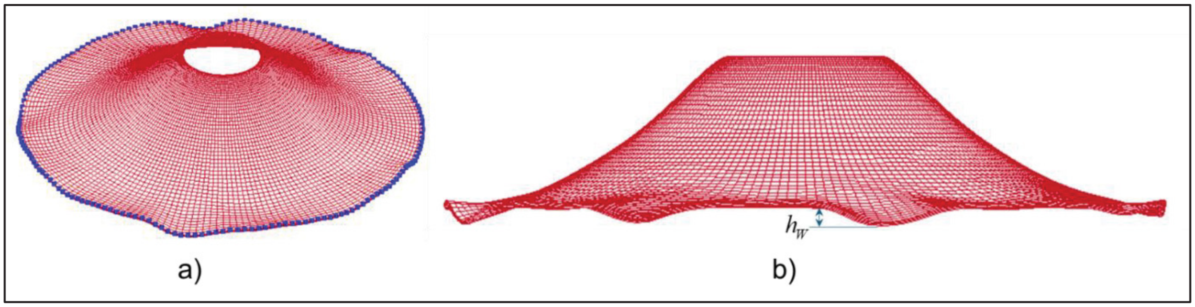

Figure 3.7 Measurement of wrinkle. a) circumferential nodes and b) wrinkle height

For example, a part that remained perfectly flat at the edge would have a negligible peak-to-valley value, whereas a part with pronounced wrinkling would show a larger amplitude. This procedure was performed at the same radial position for all samples to ensure consistency. The wrinkle measurement method based on the scanned node coordinates around the circumference as presented in Figure 3.7a provided a numerical value that could be directly compared between the flanged-edge blank and the flat blank. All measured data were documented for correlation with the simulation results and for evaluating the effectiveness of the flanged-edge blank approach.

3.4 Results

The FE simulations and experiments show strong agreement, revealing clear differences between flat and flanged-edge blanks in stress distribution, deformation, and wrinkle formation. Key results are presented below with side-by-side comparisons of simulation and experimental outcomes of each case and highlights the stabilizing influence of the added flange.

3.4.1 Wrinkling patterns and onset of instability

Both the simulations and experiments confirmed that adding a flange prior to spinning effectively eliminated wrinkling during the first pass. As shown in Figure 3.8, the simulated part geometries closely mirror the experimental outcomes. During the initial flanging stage

(Figure 3.8c), the blank (Figure 3.8a) is formed into an upturned flange with matching profiles, and in the subsequent conventional spinning pass the flat blank develops severe circumferential wrinkles (Figure 3.8b) whereas the flanged-edge blank remains smooth and wrinkle-free (Figure 3.8d). The flat blank's flange quickly becomes corrugated as the roller advances, while the flanged blank's flange retains a uniform shape. This side-by-side comparison highlights the flange's stabilizing effect on the deformation process. FE model accurately captured the wrinkling behavior of the flat blank observed in the experiment.

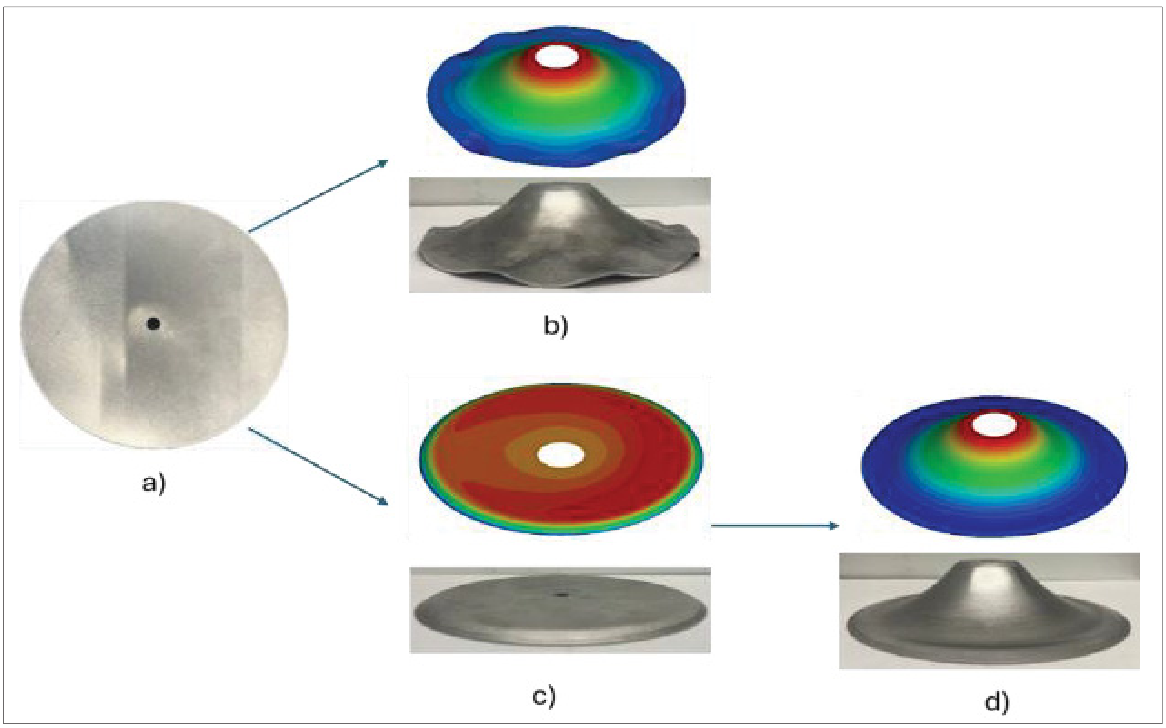

Figure 3.8 Geometry states of spun parts in both simulation and experiment.

a) original flat blank; b) flat blank after conventional spinning;
c) flanged-edge blank formed by the flanging operation and d) flanged-edge blank after conventional spinning

At the end of the spinning pass, the spun part from the flat blank exhibits multiple large wrinkles around its flange, as shown by the experimental result (Figure 3.9a). The simulation reproduces these wrinkles at the same locations and with similar wavelengths (Figure 3.9b). Stage 1 corresponds to the earliest point at which the roller induces appreciable plastic strain in the blank, thereby initiating incipient instability within the flat sheet. Almost immediately thereafter, stage 2 records a pronounced shift in behavior: the first wrinkles appear precisely when the compressive hoop stress at the rim surpasses its critical buckling threshold. The tiny distance separating stages 1 and 2 reveals how abruptly instability is triggered, whereas the wider interval before Stage 3 signals a more gradual accumulation of deformation. Between stages 2 and 3 the process advances appreciably, often settling into a quasi-stable regime or adopting an alternative deformation mode. The final fifth of the toolpath, extending from stage 3 to 4, completes the forming operation at the rim. By the end of the pass, the spun part from flat blank was heavily corrugated with several pronounced peaks and valleys, which the simulation captured with high fidelity. A comparable trend was documented by other researchers [19], who observed that when the toolpath gradient became less steep, wrinkle magnitude diminished while the count of wrinkle peaks grew.

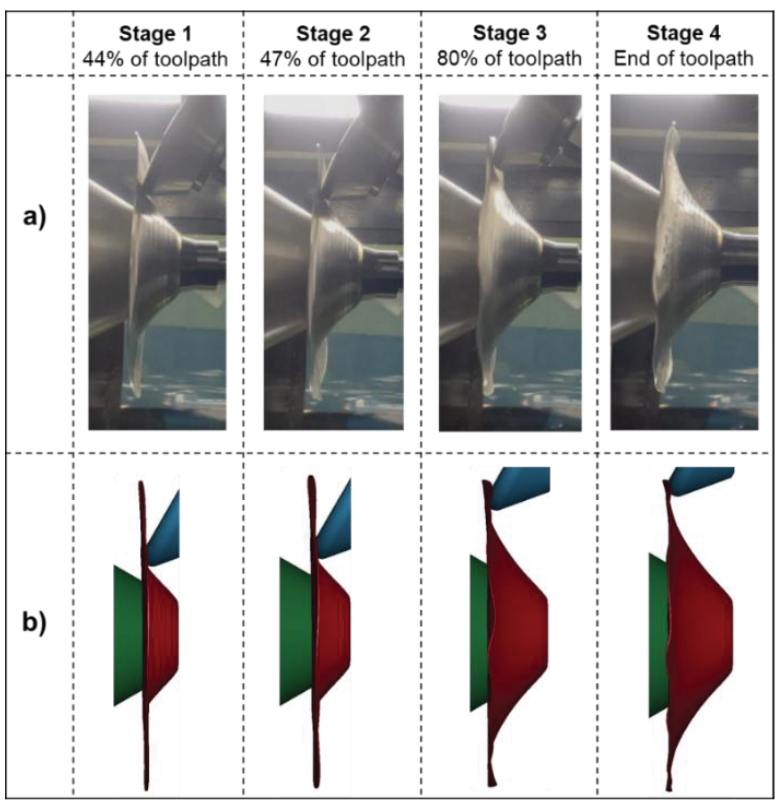

Figure 3.9 Wrinkling patterns of the flat blank during spinning process
a) experiment and b) simulation

In contrast, both the experiment (Figure 3.10a) and simulation (Figure 3.10b) presented that the flanged-edge blank remained wrinkle-free throughout the process. The pre-formed flange prevented significant out-of-plane deformation at the edge as well as retained a smooth, continuous profile with only negligible waviness with maximum height of 1.3 mm, which is attributed to the normal material bending in metal spinning rather than buckling instability. The results show that a flange with sufficient out of plane section provides enough rigidity to suppress the flange buckling. For instance, a 20° flange was found to be insufficient because its behavior was similar to the flat blank with wrinkles forming, whereas flange angles of 30° and above completely prevented wrinkling. Thus, under the given conditions, a flange angle of roughly 30° appears to be the minimum threshold for effective wrinkle suppression. The strong agreement between simulation and experiment in this study highlights the reliability of the FE approach for predicting wrinkling phenomena in spinning processes, providing confidence in its accuracy and applicability.

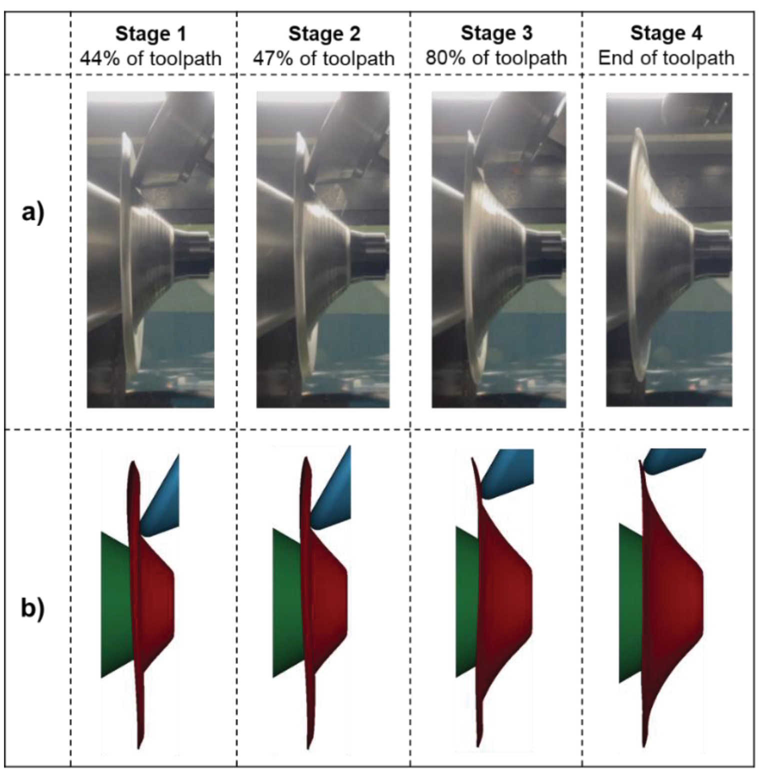

Figure 3.10 Geometry of the flanged-edge blank during spinning process
a) experiment and b) simulation

3.4.2 Axial force response

The comparison of axial forces in conventional spinning for flat and flanged-edge blanks revealed little differences in force requirements, with the flanged-edge blank necessitating higher forces. This behavior, observed in both experimental and simulation results as shown in Figure 3.11, highlights the influence of the flange on deformation mechanics. However, the simulation consistently overestimated forces, due to simplifying assumptions such as load rate scaling, material homogeneity and constant friction. In reality, variations in material properties like thickness and grain structure and dynamic frictional changes during spinning, influenced by factors such as temperature and lubrication, contribute to deviations from the idealized model. A similar trend was noted by Elizalde [21] in his shear spinning studies, where force predictions deviated by approximately 20% from experimental values. Despite these discrepancies, the simulation accurately captured the overall force-displacement trend, closely aligning with the forces registered by the DENN DATA software integrated with the DENN spinning machine. This consistency validates the simulation's ability to represent the general mechanics of the spinning process while highlighting areas for refinement in modeling assumptions.

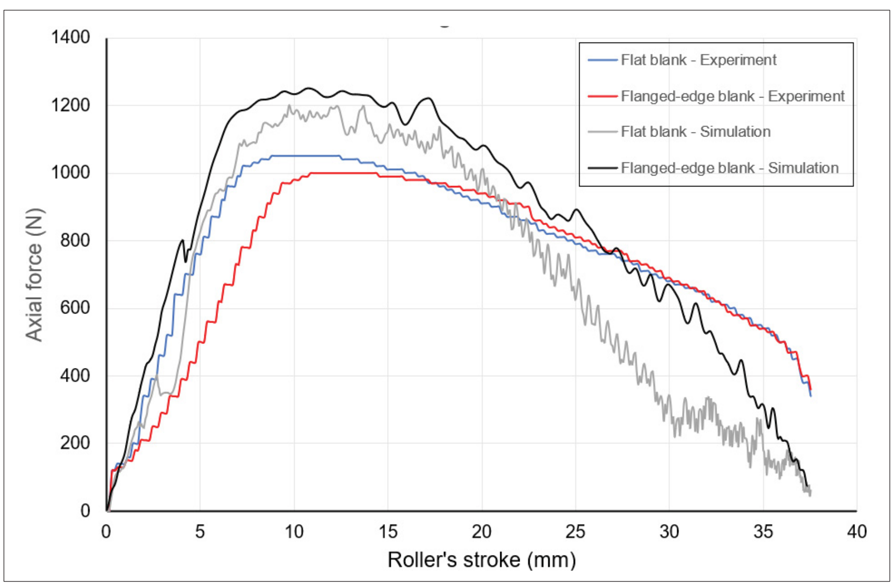

Figure 3.11 Axial force in conventional spinning

3.4.3 Stress distribution

Differences in hoop stress between the flat and flanged blanks explain why only the flat blank wrinkled. Figure 3.12 compares the simulated hoop stress fields in the two cases during the spinning pass. In the flat blank (Figure 3.12a), large compressive hoop stresses concentrate at the outer rim just ahead of the roller. Essentially, as the roller pushes inward, the unsupported flange of the flat blank is placed in compression. This leads to a highly localized band of intense compressive stress near the free edge. Once this stress exceeds the critical buckling stress of the material, the flange buckles outward and forms wrinkles. The peak compressive stress in the flat blank was predicted to occur around the same point that wrinkles first appeared, linking the simulation's stress criterion with the observed onset of instability.

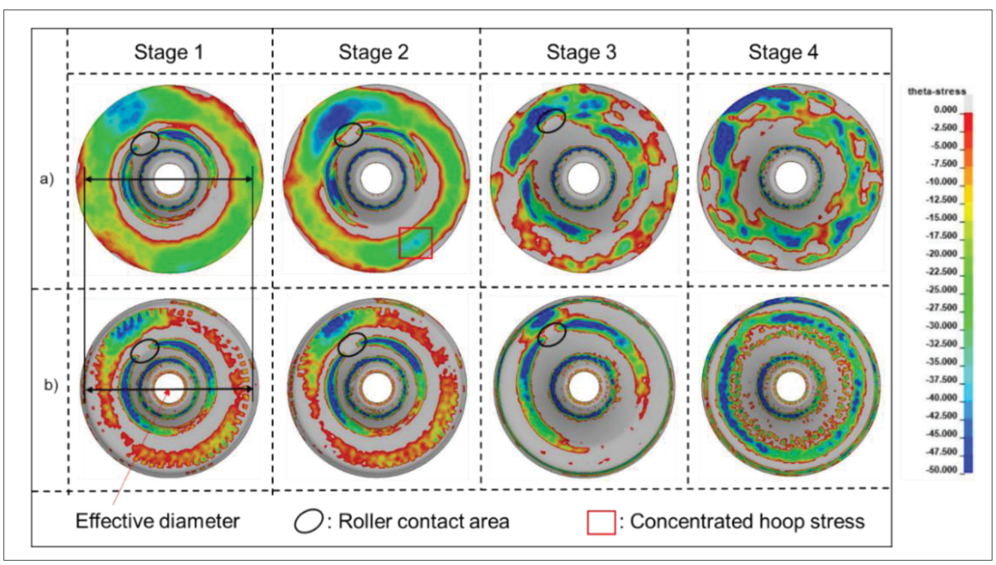

Figure 3.12 The hoop stress pattern of a) the flat blank and b) the flanged-edge blank during spinning process

By contrast, the hoop-stress field is far more diffuse in the flanged-edge specimen, as illustrated in Figure 3.12b. The upturned rim reshapes the load path so that a narrow band along the bent edge carries tensile hoop stress, while the compressive stresses that arise ahead of the roller are both lower in magnitude and distributed over a broader sector of the blank. Acting as a structural stiffener, the flange prevents the outer perimeter from being driven into the severe compression observed in the flat sheet. Rather than a single, highly concentrated compressive band at the rim, the flanged edge exhibits a moderate compressive gradient that is shared between the curvature and the flange itself, and the extreme outer edge even experiences mild tension generated by bending. This balanced distribution keeps the maximum compressive level well below the threshold for wrinkle initiation. FE predictions confirm that the flanged-edge blank never reaches the critical compressive hoop stress recorded in the flat specimen. Although direct stress measurement is not feasible in the experiment, the correspondence between numerical results and experimental observations (wrinkles in the flat case and a smooth surface in the flanged case) provides strong corroboration.

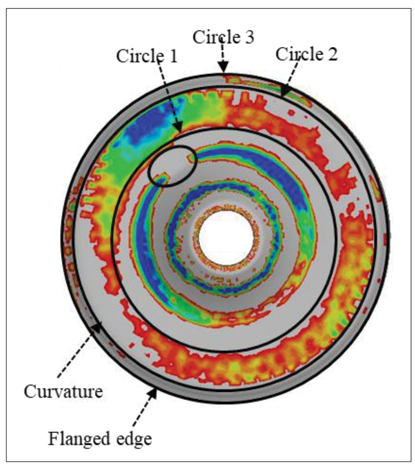

Figure 3.13 In-depth analysis of the hoop stress distribution in the flanged-edge blank during stage 2

Figure 3.13 partitions the hoop-stress distribution of the flanged-edge blank into three characteristic zones. The tensile strip at the extreme edge, labelled circle 3, offsets the compressive stresses in the interior zones, circles 1 and 2, that lie adjacent to the roller. This internal compensation prevents any region from surpassing the critical load for buckling and thereby suppresses wrinkle formation. The pre-formed flange therefore reorganizes the entire stress field, eliminating the sharp peaks that trigger instability in the flat blank. The close agreement between simulated stress patterns and observed surface morphologies affirms that the model captures the essential deformation physics with a high degree of fidelity.

3.4.4 Thickness distribution

Introducing a peripheral flange markedly reshapes the wall-thickness profile after spinning. Figure 3.14 compares the final thickness distribution along the normalized radius for flat and flanged blanks, bringing together experimental measurements and FE predictions. The flat specimen undergoes thinning within the spun zone, where the wall falls from its initial 1 mm to about 0.7 mm, a reduction of roughly thirty percent. The minimum occurs near twenty percent of the normalized distance, confirming intense material stretching during inward flow. Thickness then rises toward the rim as material accumulates at wrinkle crests after buckling.

In contrast, the flanged blank exhibits a smoother profile. The thinnest section measures close to 0.75 mm, a maximum reduction of twenty-five percent and following a gentle gradient instead of the instable drop seen in the flat blank. This uniformity stems from the flange distributing deformation more evenly and preserving material. Measurements verify that the flanged configuration retains thickness better and therefore diminishes the excessive thinning and wrinkle initiation.

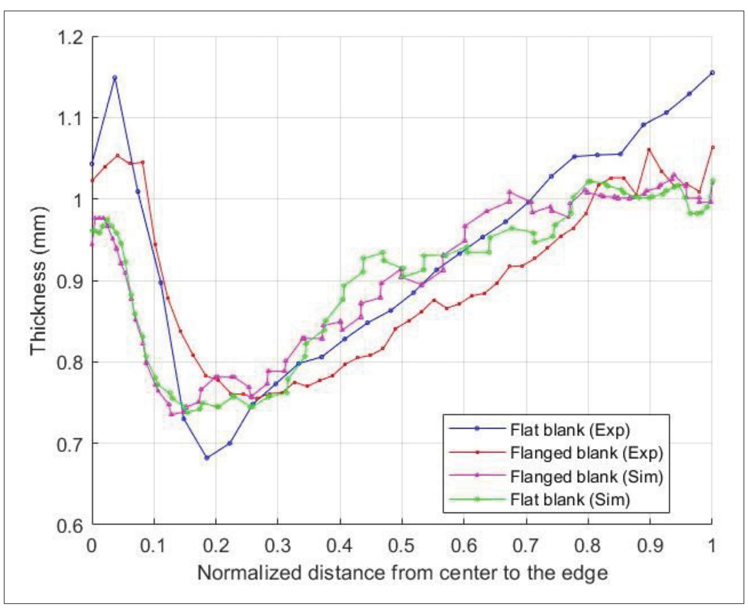

Figure 3.14 The thickness variation of the flat blank and the flanged-edge blank

The FE model captures these trends with high fidelity, demonstrating that the chosen constitutive description and volume-constancy enforcement reliably reproduce stretching and thinning mechanics. In the flanged case, thin spots and stress concentrations are largely removed, whereas the flat blank still develops localized necks that foster instability. The close agreement between simulation and experiment highlights the flange's beneficial impact on structural integrity.

3.4.5 Wrinkle amplitude and final flanged deformation

The flat blank exhibited severe wrinkling. In Figure 3.15a, the experimental data for the flat blank show significant oscillations in the Z-coordinate around the circumference, generally ranging within 30.2 mm and 34.8 mm. The FE simulation for the flat blank mirrors this pronounced oscillatory behavior and exhibits a similar oscillatory trend, but at a higher absolute Z level, generally ranging within 33.5 mm and 38.5 mm, indicating substantial, non-uniform flange deformation. Accordingly, the comparison of wrinkling severity is interpreted primarily from the circumferential variation in Figure 3.15b rather than the absolute Z offset in Figure 3.15a. Figure 3.15b further quantifies this waviness. The experimental height of the flat blank's flange varies dramatically, with peak-to-valley differences locally about 5 mm (e.g., from -2.5 mm to +2.5 mm). The simulation captures this trend of large amplitude variations. The 3D displacement plot for the flat blank visually confirms the formation of multiple, large wrinkles across the flange surface. The consistency between the experimental data and the FE simulation results underscores the model's ability to accurately predict the significant wrinkling instability inherent in flat blanks.

In contrast, the flanged-edge blank demonstrated exceptional resistance to wrinkling. As shown in Figure 3.15a, both the experimental and the simulated Z-coordinate remain relatively constant around the circumference, fluctuating only slightly (e.g., between approximately 35 mm and 36 mm for the experimental data). This indicates a much more stable and uniform flange edge. Similarly, in Figure 3.15b, the height variation for the flanged-edge blank is minimal, generally staying within a ±0.5 mm band. This signifies only minor waviness rather than distinct wrinkle formation. The 3D displacement plot for the flanged-edge blank (bottom right panel) shows a smooth, uniformly deformed flange, with a notable overall Z-displacement but without the localized peaks and valleys characteristic of wrinkling. This deeper, more uniform draw, combined with the minimal circumferential variation, highlights the flange's effectiveness in suppressing buckling and severe wrinkling. The maximum observed wrinkle amplitude in the flanged-edge blank was drastically reduced compared to the flat blank.

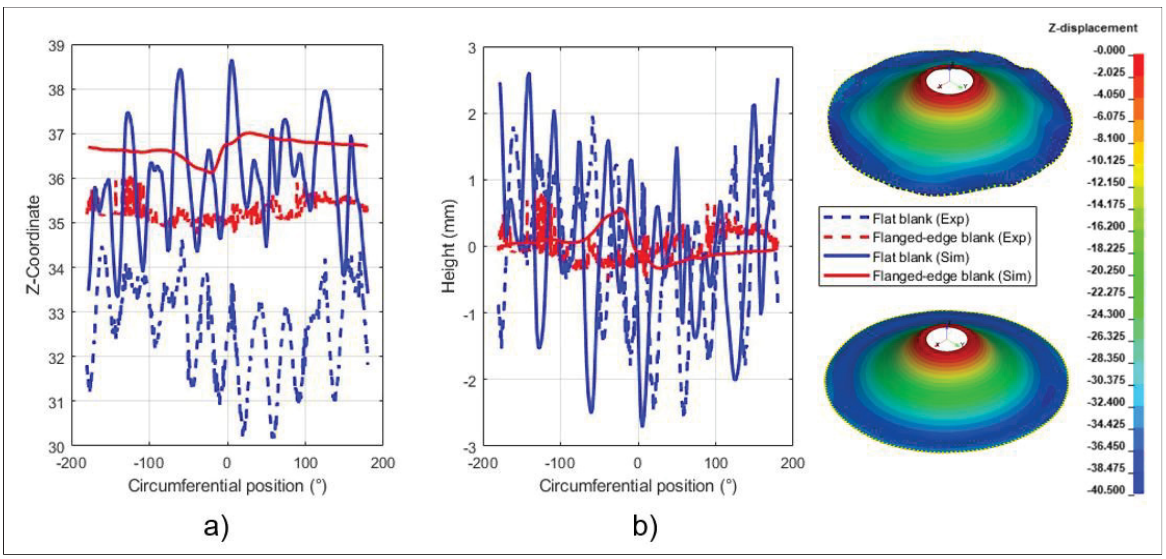

Figure 3.15 Amplitude of the wrinkle of the flat and flanged-edge blank at the final state along the circumferential position. a) Z-coordinate and b) corresponding height variation

Figure 3.16 illustrates the evolution of overall wrinkle amplitude (amplitude variation) as a function of roller movement for both blank types, accompanied by snapshots of the blank's deformed shape at various stages. The flat blank shows a rapid and substantial increase in amplitude variation almost from the beginning of the roller movement. The amplitude quickly rises, exceeding 11 mm after approximately 10 mm of roller travel, and continues to oscillate with high values (peaking around 15 mm) throughout a significant portion of the process. This behavior is indicative of the early onset and continuous development of severe wrinkling, as visually confirmed by the progressive distortion in the accompanying 3D shape snapshots for the flat blank.

Conversely, the flanged-edge blank maintains a significantly lower and more stable amplitude variation throughout the entire roller movement. The amplitude variation for the flanged blank generally remains below 5 mm, and for a large part of the process, it is well under 4 mm. This demonstrates the flanged edge's consistent ability to suppress the growth of wrinkles from the initial stages of deformation through to the final roller stroke. The 3D shape snapshots for the flanged-edge blank confirm a much smoother and more controlled deformation process.

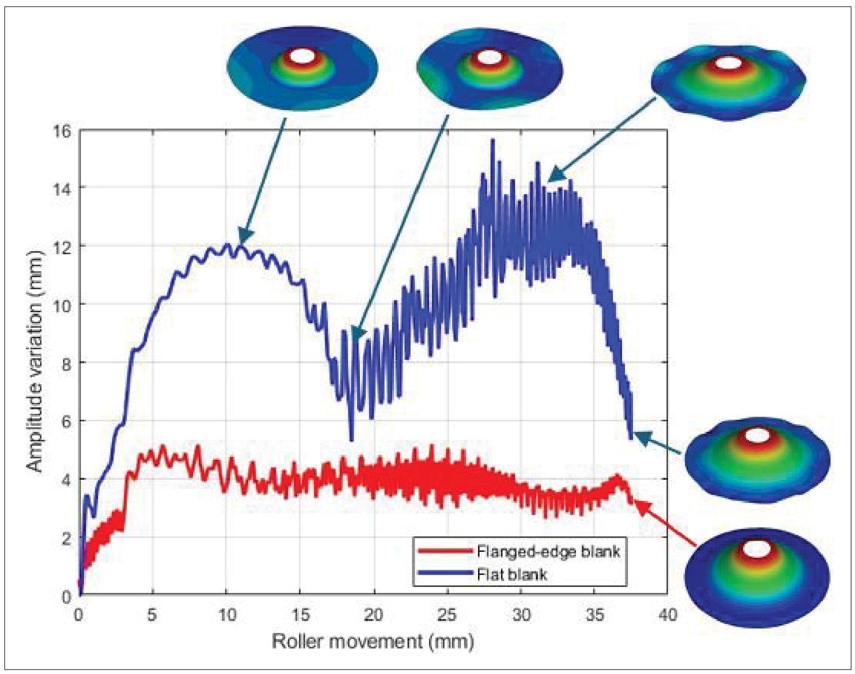

Figure 3.16 Evolution of wrinkle amplitude of a flat blank and a flanged-edge blank with increasing roller stroke

3.4.6 Influence of flange geometry on bending rigidity

Bending rigidity, a fundamental property in structural mechanics, is defined as the product of a material's Young's modulus and its second moment of inertia, expressed as EI. This parameter quantifies a structure's resistance to bending deformation under applied loads. In the context of spinning flanging, a sheet metal forming process, a flat sheet is plastically deformed to create flanges-raised edges that alter the cross-sectional geometry (Figure 3.17). This geometric change increases the second moment of inertia, thereby enhancing the bending rigidity of the resulting component. The increased rigidity improves the structural integrity of the part and plays a critical role in suppressing wrinkles during subsequent spinning process. For a flat sheet, I is minimal because the material is concentrated close to the neutral axis. However, when flanges are formed through flanging operation, material is displaced farther from the neutral axis, significantly increasing I. This principle mirrors observations in related sheet metal forming techniques. For instance, Liu [22] demonstrated that embossing-a process that introduces periodic concavities and convexities-enhances bending rigidity by similarly increasing I, through geometric modification.

To evaluate the effect of spinning flanging on the second moment of inertia I, analytical calculations were conducted for a range of flange lengths and flange angles. The cross-section was modeled as a symmetric structure comprising a main sheet and two inclined flanges, with a total length of 180 mm conserved across all configurations. The cross-section moment of inertia was calculated using the parallel axis theorem, which accounts for the contributions of both the main sheet and the flanges to the overall I about the neutral axis. Figure 3.17 shows the cross-section of the flanged-edge blank after flanging.

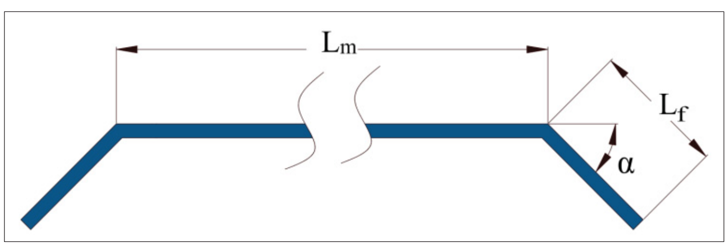

Figure 3.17 Schematic of cross section moment of inertia after flanging

Before calculating the second moment of inertia for a flanged structure after spinning flanging, the following assumptions are made to simplify the analysis

1 Symmetry: The flanged structure is symmetric about the central axis, allowing the contributions of the two flanges to be mirrored in the calculation.

2 Uniform material: The material has uniform thickness t and consistent properties (e.g., density) across the main sheet and flanges.

3 Negligible bend radius: The bend radius at the junction between the main sheet and the flanges is assumed to be negligible, treating the transition as a sharp angle.

4 Known geometry: The flange length L_f, flange angle α, main sheet length L_m, and thickness t are fixed and known for the calculation.

5 Conservation of length: The total length of the sheet remains constant $L = L_m + 2L_f\, cos\,\alpha = 180mm$, where L_m is adjusted based on L_f and α parameters.

These assumptions enable a tractable analytical approach while maintaining reasonable accuracy for engineering purposes. For the flat blank I_{flat} is calculated in equation (3.4)

$$I_{flat} = \frac{L \cdot t^3}{12} \tag{3.4}$$

For a flanged structure after spinning flanging operation, second moment of inertia of the flanged-edge blank $I_{total-flange}$ is calculated in equation (3.5) by summing the contributions of the main sheet and the two flanges. Equation (3.6) gives the position of the global centroid.

$$I_{total-flange} = \left[\frac{L_m t^3}{12} + \left(L_m t\right)\left(\bar{y} - \frac{t}{2}\right)^2\right] + 2\left[\frac{tL_f^3 \sin^2\alpha}{12} + \frac{L_f t^3 \cos^2\alpha}{12} + \left(L_f t\right)\left(\bar{y} - t - \frac{L_f}{2}\sin\alpha - \frac{t}{2}\cos\alpha\right)^2\right] \tag{3.5}$$

$$\bar{y} = \frac{\frac{L_m t}{2} + L_f\left(L_f \sin\alpha + t\cos\alpha\right)}{L_m + 2t} \tag{3.6}$$

Detail of the calculation is given in the appendix.

Figure 3.18 shows that the second moment of inertia rises sharply when flange length increases because more material is distributed farther from the neutral axis and also increases with larger flange angles, particularly in the moderate-to-steep range about 60°–75°. Beyond 75°, the incremental gains diminish. Within the explored range (flange length ≤ 14 mm), the highest stiffness observed occurred near the upper end of length and at angles around 60°–70°. Longer flanges were not evaluated here, so this should be interpreted as a local optimum within the tested range, not a global maximum.

For a flat blank, the second moment of inertia is minimal with $I_{flat} = 15mm^4$. In contrast, for a flanged-edge blank, $I_{total-flange}$ rises sharply with increasing flange length due to greater material displacement from the neutral axis. Beyond $\alpha = 75^{\circ}$, gains diminish as the flange approaches a vertical orientation, suggesting an optimal range of $\alpha = 60^{\circ} - 75^{\circ}$ for maximum stiffness. These results demonstrate that flanging significantly enhances bending rigidity, with flange length exerting a stronger influence than angle within practical limits, correlating with improved wrinkle resistance observed in subsequent spinning passes.

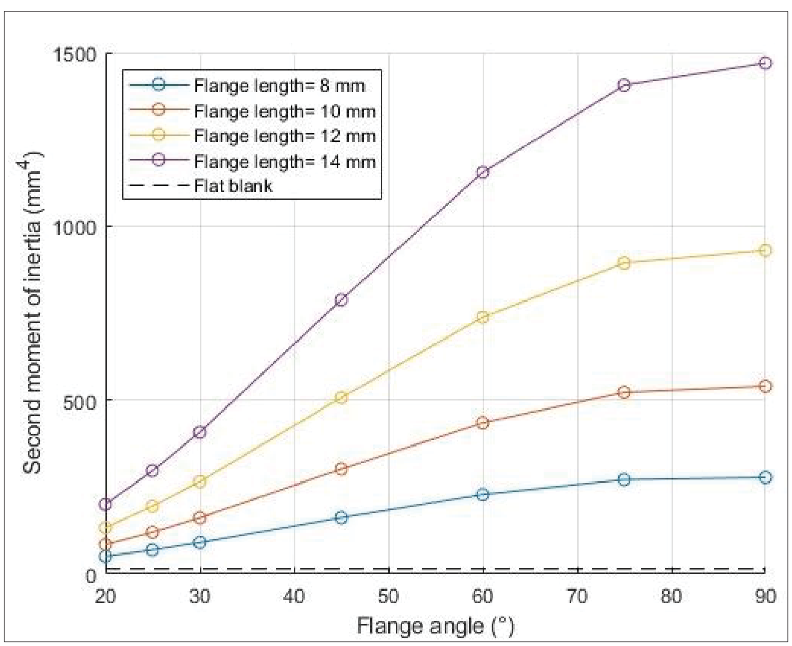

Figure 3.18 Second moment of inertia of flanged edge blank after flanging

3.5 Discussion

The pronounced difference in wrinkling behavior between conventional flat blanks and flanged-edge blanks is fundamentally linked to how the flanged geometry alters deformation mechanics at the blank's periphery. By introducing an upturned flange prior to spinning, the blank's edge gains significant out-of-plane stiffness, which in turn redistributes compressive stresses and delays the onset of buckling. In essence, the flanged-edge design raises the wrinkling threshold, the critical condition at which compressive hoop stress causes instability, keeping the blank in a stable deformation regime under conditions that would readily buckle a flat blank.

3.5.1 Stress distribution and bending rigidity

In the flat blank, the flange is a wide, free sheet region, so as the roller pushes inward, the compressive hoop stress tends to concentrate near the outer edge of the flange since that edge is free and cannot sustain tension, it "bunches up". This leads to a high peak circumferential stress $\sigma_{\theta,\max}$ at the flange edge, which rapidly reaches the critical level and triggers buckling. In the flanged-edge blank, however, the upturned flange acts like a reinforcing rim. The flange's edge is bent upward, giving it a greater bending rigidity (higher second moment of inertia) about the circumferential axis. This increased bending stiffness means the edge offers resistance to out-of-plane deflection and effectively behaving like a built-in stiffener rather than a free edge. As a result, when compressive forces develop, the flange can deform in a more distributed manner instead of one localized zone taking all the compression and buckling. As a result, some of the strain energy is absorbed in bending the flange lip and the compressive load is spread more evenly across the flange width. The FE simulations confirmed that in the flanged blank, the hoop compressive stress was more uniformly distributed and the peak value was significantly lower than in the flat blank at equivalent stages of forming. In fact, a portion of the flange near the bent lip experienced a slight tensile stress due to the bending constraint, which helped counteract the compression in the rest of the flange. This contrasts with the flat blank, where essentially the entire flange is under compression during forming.

According to plate buckling theory [23], increasing thickness achieved by the flange geometry will increase the critical stress $\sigma_{\theta,cr}$ required to initiate wrinkling.

$$\sigma_{\theta,cr} = -\frac{\sigma_s \cdot t}{\sqrt{3} \cdot f \cdot \cos\alpha} \tag{3.7}$$

where σ_s is the yield stress of material; t is the plate thickness; f is the feed ratio; α is the half angle of the mandrel.

In conventional spinning, the thicker the material is, the more bending rigidity it gets. In our case, the flanged-edge blank's periphery had a far higher bending rigidity than the flat blank's, meaning it could withstand much greater compressive force before yielding to buckling. In effect, the flanged-edge blank's flange possesses a higher critical load and stress for buckling. This was evident in the simulations where the flat blank began to wrinkle at a very small compressive load whereas the flanged blank, with its stiffened edge, showed no wrinkling even at the maximum load/stroke of the first pass. The increased bending rigidity provided by the flange not only delays the onset of wrinkling but also ensures that any out-of-plane deflection remains minimal and self-limiting. This benefit carries into subsequent passes as well. The flanged edge is able to maintain structural integrity under repeated loading, whereas a flat edge with low stiffness would collapse further once wrinkling starts.

3.5.2 Effective compressive region and critical stress

The flanged edge changes how compressive stress is distributed across the flange width during spinning. Figure 3.16 presented the reduced effective diameter of the flanged-edge blank after flanging operation. In the flat blank, as the roller forces the material, the excess circumferential length of the flange since it must shrink to a smaller radius is mostly accommodated by in-plane compression of the flange. This compression tends to concentrate in a relatively wide band of the flange, leading to a high peak circumferential stress in the material. Essentially, the entire unsupported flange acts as the effective compressive region in the flat blank case. It is all prone to compression and thus can buckle in a long wavelength mode involving multiple large wrinkles. In contrast, the flanged-edge blank can redistribute some of the deformation into bending of the flange lip rather than purely in-plane compression. The stiff flanged lip forces the compressive deformation to spread more evenly and over a smaller effective length of the flange. The result is a lower maximum hoop stress at any given stage and a narrower zone of the flange in true compression. Our simulation results confirmed that throughout the process the peak hoop stress in the flanged blank's flange was significantly lower than that in the flat blank, and the flanged blank's stress distribution was more uniform. In fact, near the outer bent edge of the flange, the material in the flanged blank experienced slight tension or much reduced compression due to the bending resistance of the lip counteracting the compressive strain, whereas the flat blank's outer edge was the locus of maximum compression. This means the flanged blank avoided highly localized compressive overstress in the critical outer region. Moreover, because part of the flange is geometrically constrained, the length of flange under effective compression is reduced. According to the energy-based buckling models, a shorter compressive span raises $\sigma_{\theta,cr}$ which is similar to how a shorter plate or column is more stable [24]. In other words, the flanged blank's flange behaves as if it has a built-in support that segments the would-be buckling mode into a smaller section. Kong [25] analysis explicitly showed that by narrowing the effective compressive region (Figure 3.12), the wrinkling threshold stress increases. Therefore, the flanged-edge design benefits from both a reduction in the applied peak compressive stress and an increase in the critical stress needed for buckling. This ensures that throughout the forming process the condition $\sigma_{\theta,\max} < \sigma_{\theta,cr}$ is maintained for the flanged blank, whereas the flat blank quickly violates this condition.

The flanged-edge design essentially provides a built-in countermeasure to wrinkling by altering the flange's structure. Instead of needing an external tool to support the flange [4], the flange's own geometry provides the own support. This has practical advantages such as it simplifies the process because the flange is formed with the same roller in a preceding step and avoids additional tooling, while still achieving the goal of wrinkle suppression. It is worth noting that in our study the flange angle was 30°, which was sufficient to prevent wrinkles. A smaller flange might not provide as much stiffness, whereas a larger flange such as steeper angle or longer lip could further increase rigidity. Indeed, our findings align with the observation by Chen [3] that a stronger reinforcement of the flange with increased bending stiffness or reduced effective length raises the wrinkling threshold. There may be an optimal flange geometry beyond which additional stiffness yields diminishing returns or could cause other issues such as difficulty in forming the flange. However, within the tested range, the flanged-edge proved highly effective.

3.6 Conclusions

This study has demonstrated that pre-forming a flange on the blank effectively eliminates wrinkles during the first pass of conventional spinning. Both FE simulations and experiments have shown that flanged-edge blanks remain essentially wrinkle-free, whereas flat blanks develop severe circumferential buckling under identical conditions. The flanged shape functions as a built-in reinforcement by enhancing the second moment of inertia of the edge region, which boosts bending stiffness and shifts compressive hoop stresses away from the unsupported outer rim. As a result, the critical buckling threshold is raised and the blank deforms smoothly with uniform thickness. The close agreement between simulation and experiment validates the model and confirms the effectiveness of flanging as a wrinkle-prevention strategy.

Parametric analysis highlighted the critical roles of flange angle and length. A moderate flange angle (around 30°) was sufficient to suppress wrinkling completely, whereas a shallow flange (about 20°) behaved similarly to a flat blank and still wrinkled. Increasing the angle further to about 60–70° continued to improve stiffness, although gains diminished beyond roughly 75°. Extending the flange length also increased bending stiffness by moving material away from the neutral axis, whereas flanges shorter than approximately 8 mm provided negligible benefit. Overall, within the practical range studied, flange length had a stronger impact on edge rigidity than angle. These geometric effects promote a more uniform stress and strain distribution during spinning, thereby preventing localized buckling and maintaining dimensional accuracy.

The practical implications for industry are significant. By simply adding a pre-formed flange to the blank, manufacturers can produce thin-walled metal components with far fewer wrinkles. This approach is compatible with standard spinning equipment and tooling, implying straightforward implementation. The validated FE model provides a predictive design tool to optimize flange parameters and tool paths for new parts. In practice, adopting flanged-edge blanks could reduce scrap rates and enable more aggressive forming schedules, thereby enhancing productivity and reliability of metal spinning operations.

Future work will first validate that flanged-edge blanks can be carried through a full conventional multi-pass diameter-reduction schedule, including later passes in which the roller traverses closer to the rim. Pass-by-pass thickness evolution, force histories, and intermediate geometries will be documented to quantify any interaction between rim rigidity and standard material-transfer behavior. This will be followed by a matched-condition benchmark that contrasts passive stabilization by a prefabricated rim with state-of-the-art active restraint provided by a backup roller on flat blanks. It will also assess hybrid routes that couple roller-assisted pre-flanging with tuned flange-constrained passes. Finally, the edge-design space will be expanded by comparing flange orientation and other prefabricated edge stiffeners. The comparison will include edge features produced by established rim-forming operations, such as bending-based flanging, incremental flanging, beading, and hemming. Where necessary, pass-by-pass toolpath refinement will be applied to improve robustness and repeatability.

3.7 References

1. Kobayashi S (1963) Instability in conventional spinning of cones. J Eng Ind 85:44–48. https://doi.org/10.1115/1.3667585
2. Gao PF, Yan XG, Li FG, Zhan M, Ma F, Fu MW (2022) Deformation mode and wall thickness variation in conventional spinning of metal sheets. Int J Mach Tools Manuf 173:103846. https://doi.org/10.1016/j.ijmachtools.2021.103846

3. Chen SW, Zhan M, Gao PF, Ma F, Zhang HR (2021) A new robust theoretical prediction model for flange wrinkling in conventional spinning. J Mater Process Technol 288:116849. https://doi.org/10.1016/j.jmatprotec.2020.116849
4. Yu ZQ, Zhao Y, Du C, Liu R, Evsyukov SA (2020) Study on flange-constrained spinning process for hemispherical aluminum alloy part. J Mater Process Technol 278:116515. https://doi.org/10.1016/j.jmatprotec.2019.116515
5. Music O, Allwood JM, Kawai K (2010) A review of the mechanics of metal spinning. J Mater Process Technol 210:3–23. https://doi.org/10.1016/j.jmatprotec.2009.08.021
6. Li ZH, Long H (2022) An analytical model integrated with toolpath design for wrinkling prediction in conventional spinning. J Mater Process Technol 300:117399. https://doi.org/10.1016/j.jmatprotec.2021.117399
7. Wang L (2012) Analysis of material deformation and wrinkling failure in conventional metal spinning process. PhD thesis, Durham University. http://etheses.dur.ac.uk/3537/
8. Elizalde S, Coyoy P, Casas C, Puigjaner B, Cabello D, Cabrera JM (2025) Study of the effect of the process parameters on the forming limit in shear spinning processes. Int J Adv Manuf Technol. https://doi.org/10.1007/s00170-025-15041-9
9. Xu Y, Li H, Chen W, Chen J (2019) Determination of formability considering wrinkling defect in first-pass conventional spinning with linear roller path. J Mater Process Technol 266:6–15. https://doi.org/10.1016/j.jmatprotec.2018.10.003
10. Huang J, Jin J, Deng L, Wang X, Gong P, Zhang M, Gao C (2021) Theoretical prediction of flange wrinkling in the first-pass conventional spinning of dual-metal sheets. J Manuf Process 62:368–377. https://doi.org/10.1016/j.jmapro.2020.12.044
11. Kleiner M, Gobel R, Kantz H, Klimmek C, Homberg W (2002) Combined methods for the prediction of dynamic instabilities in sheet metal spinning. CIRP Ann Manuf Technol 51:209–214. https://doi.org/10.1016/S0007-8506(07)61501-7
12. Xia Q, Shima S, Kotera H, Yasuhuku D (2005) A study of the one-path deep drawing spinning of cups. J Mater Process Technol 159:397–400. https://doi.org/10.1016/j.jmatprotec.2004.05.027

13. Wang L, Long H (2011) A study of effects of roller path profiles on tool forces and part wall thickness variation in conventional metal spinning. Mater Des 32:2140–2151. https://doi.org/10.1016/j.jmatprotec.2011.07.013
14. Watson M, Long H, Lu B (2015) Investigation of wrinkling failure mechanics in metal spinning by Box-Behnken design of experiments using finite element method. Int J Adv Manuf Technol 78:981–995. https://doi.org/10.1007/s00170-014-6694-6
15. Russo IM, Cleaver CJ, Allwood JM (2020) The influence of part asymmetry on the achievable forming height in multi-pass spinning. J Mater Process Technol 275:116354. https://doi.org/10.1016/j.jmatprotec.2019.116350
16. Russo IM, Cleaver CJ, Allwood JM (2021) Seven principles of toolpath design in conventional metal spinning. J Mater Process Technol 295:117156. https://doi.org/10.1016/j.jmatprotec.2021.117131
17. Ahmed KI, Gadala MS, El-Sebaie MG (2015) Deep spinning of sheet metals. Int J Mach Tools Manuf 97:72–85. https://doi.org/10.1016/j.ijmachtools.2015.07.005
18. Rentsch B (2018) Virtual design and adaptive control of metal spinning processes. PhD thesis, ETH Zurich. https://doi.org/10.3929/ethz-b-000267320
19. Nguyen HH, Champliaud H, Le VN (2024) Effect of intermediate path on post-wrinkle initiation of the multi-pass metal spinning process: Analysis in the rotating reference frame. J Manuf Mater Process 8(1):19. https://doi.org/10.3390/jmmp8010019
20. Uzun, M.C., Music, O. Shear spinning: numerical modelling and process mechanics. *Int J Adv Manuf Technol* **135**, 4015–4033 (2024). https://doi.org/10.1007/s00170-024-14682-6
21. Elizalde Huitrón SA (2024) Study on the forming limit on shear spinning process. PhD thesis, Universitat Politècnica de Catalunya. https://doi.org/10.5821/dissertation-2117-421221
22. Liu WY, Suzuki Y, Iizuka T, Shiratori T, Komatsu T (2018) Variation of tensile and bending rigidities of a duplex embossed steel sheet by small uniaxial tensile deformation. J Mater Process Technol 261:123–139. https://doi.org/10.1016/j.jmatprotec.2018.05.014

23. Tsien LH, Tsoon WS (1963) The limit analysis in solid mechanics and a suggested generalized variational principle. Acta Mech Sin 4:287–303
24. Cao J, Wang X (2000) An analytical model for plate wrinkling under tri-axial loading and its application. Int J Mech Sci 42(3):617–633. https://doi.org/10.1016/S0020-7403(98)00138-6
25. Kong Q, Yu Z, Zhao Y, Wang H, Lin Z (2017) A study of severe flange wrinkling in first-pass conventional spinning of hemispherical part. Int J Adv Manuf Technol 93(1–4):3583–3598. https://doi.org/10.1007/s00170-017-0744-9

3.8 Appendix of this chapter

The second moment of inertia quantifies a structure's resistance to bending and depends on how its cross-sectional area is distributed relative to the neutral axis. For a flanged structure after spinning flanging, $I_{total-flange}$ is calculated by summing the contributions of the main sheet and the two flanges, adjusted to the global centroid using the parallel axis theorem. Below are the steps to compute $I_{total-flange}$.

Step 1: Define the geometry and coordinate system

Consider a flanged structure with a horizontal main sheet of length L_m and thickness t, and two identical flanges of length L_f inclined at an angle α from the horizontal. The neutral axis (global centroid, $\bar{y}$) is determined relative to the bottom of the main sheet.

Step 2: Calculate the global centroid $\bar{y}$ by summing the area-weighted y-coordinates of the main sheet and flanges

$$\bar{y} = \frac{\frac{L_m t}{2} + L_f \left(L_f \sin\alpha + t\cos\alpha \right)}{L_m + 2t} \tag{3.8}$$

In which A_m and A_f is the main sheet area and each flange area respectively, y_m and y_f is the main sheet centroid and the centroid of flange respectively. The y-coordinate of a flange's centroid is $y_f = \frac{L_f}{2}\sin\alpha + \frac{t}{2}\cos\alpha$ (distance from the bottom of the main sheet to the flange's midpoint, accounting for the angle).

Step 3: Calculate the main sheet contribution I_m

$$I_m = I_{m,own} + A_m d_m^2 = \frac{1}{12} L_m t^3 + L_m t\left(\bar{y} - \frac{t}{2}\right)^2 \tag{3.9}$$

In which $I_{m,own}$ is the moment of inertia about its own centroid and $d_m = |\bar{y} - y_m|$ is the distance from main sheet centroid to global centroid.

Step 4: Calculate the flange contribution I_f for each flange.

$$I_{f,own} = \frac{1}{12} t L_f^3 \sin^2\alpha + \frac{1}{12} L_f t^3 \cos^2\alpha \tag{3.10}$$

With moment of inertia about its own centroid:

$$I_{f,own} = \frac{1}{12} t L_f^3 \sin^2\alpha + \frac{1}{12} L_f t^3 \cos^2\alpha \tag{3.11}$$

In which L_f is the width of the inclined rectangle and thickness t, inclined at α and the distance from flange centroid to global centroid:

$$d_f = |\bar{y} - y_f| = \left|\bar{y} - \left(t + \frac{L_f}{2}\sin\alpha + \frac{t}{2}\cos\alpha\right)\right| \tag{3.12}$$

Step 5: Calculate total second moment of inertia of flanged-edge blank

$$I_{total-flange} = I_m + 2I_f = \left[\frac{L_m t^3}{12} + \left(L_m t \right) \left(\bar{y} - \frac{t}{2} \right)^2 \right] + \tag{3.13}$$

$$2\left[\frac{t L_f^3 \sin^2 \alpha}{12} + \frac{L_f t^3 \cos^2 \alpha}{12} + \left(L_f t \right) \left(\bar{y} - t - \frac{L_f}{2} \sin \alpha - \frac{t}{2} \cos \alpha \right)^2 \right]$$

CHAPTER 4

EFFECT OF EDGE-PREFORMING ROUTE ON PRE-STRAIN DEVELOPMENT AND WRINKLE SUPPRESSION DURING A SUBSEQUENT SPINNING PASS

Mai-Van Tran, Henri Champliaud, Zhaoheng Liu, Sergio Elizalde, Mohammad Jahazi

Department of Mechanical Engineering, École de technologie supérieure,
1100 Notre-Dame Ouest, Montréal, Québec, Canada H3C1K3

Article accepted for publication in The *International Journal of Advanced Manufacturing Technology*, May 2026

4.1 Abstract

Wrinkling remains a limiting defect in spinning processes because the unsupported rim is subjected to repeated circumferential compression, local bending, unloading, and partial recovery during roller contact. This study examines how the edge-preforming route affects pre-strain development, local strengthening, and pass-level wrinkle suppression during a subsequent spinning pass of AA5052-O blanks. Two edge-preforming routes are compared, namely edge forming by bending and edge forming by spinning. Although both routes produce a flanged edge, they impose different deformation histories near the flange root and curvature band. Controlled spinning experiments, Vickers microhardness mapping, and pass-resolved finite element analysis were combined to relate the inherited curvature-band condition to the subsequent wrinkling response. The results show that edge forming by spinning produces a broader prestrained region and a higher level of retained local strengthening than edge forming by bending. This inherited condition improves rim stability during the investigated pass by promoting a more recoverable hoop-strain response and reducing the severity of final circumferential waviness. Edge forming by bending gives an intermediate response, while the flat blank reaches the critical wrinkling condition earlier. The inclined-gap schedule delays late-stage instability for cases close to the wrinkling limit, but it does not change the route-dependent stability order established by edge preforming. The experimental results are therefore evidence of improved pass-level wrinkle suppression, not proof of complete multi-

pass conventional-spinning formability. Further validation is required to assess inward material flow, diameter reduction, wall-thickness evolution, residual stress development, and final part accuracy over a complete forming route.

Keywords: conventional spinning, flange wrinkling, edge pre-straining, microhardness mapping, rim reversibility

4.2 Introduction

Metal spinning is a rotary incremental sheet-forming process used to manufacture axisymmetric hollow components by deforming a rotating blank with one or more rollers. Because deformation is concentrated near the moving roller contact, the process offers flexible tooling, relatively low forming loads, and high material utilization [1]. Depending on the forming objective, tool trajectory, material flow, and thickness evolution, spinning processes include conventional spinning, deep drawing spinning, shear spinning, and dieless spinning [1,2]. In conventional spinning, the blank is progressively formed over a mandrel, usually through several passes, while the wall thickness is intended to remain nearly unchanged [3]. In shear spinning, by contrast, wall-thickness reduction is imposed according to the mandrel angle and roller clearance [4]. This distinction is important because the present work does not aim to define a shear spinning forming limit. Instead, it examines how different edge preforming routes modify the inherited blank condition before a subsequent spinning pass.

Process design in metal spinning remains difficult because the local deformation state changes continuously as the roller advances. The roller path affects contact location, forming force, wall-thickness variation, shape development, and the deformation imposed on the unsupported flange [3,5]. Toolpath design also depends on force control, feed ratio, flange angle, and pass sequencing, which explains why experience-based design remains common in many spinning operations [6]. Multi-pass spinning can improve spinnability by distributing deformation over successive passes, but the response of a later pass also depends on the geometry, strain state, and hardening inherited from earlier deformation [7]. Therefore, the flange condition before a subsequent pass begins becomes an important factor in the stability of the forming process.

Flange wrinkling is one of the main defects limiting conventional spinning and related spinning processes. It develops when circumferential compression in the unsupported rim exceeds the stabilizing effects of sheet thickness, material strength, local curvature, and flange stiffness [8,9]. Early analytical work described wrinkling as a plastic instability caused by compressive circumferential stress in the flange [9]. Later models improved wrinkling prediction by considering blank geometry, feed ratio, material properties, and roller path effects [10,11]. These models are useful for defining process limits, but they provide limited information on how a preconditioned flange root modifies the response of a subsequent spinning pass.

Wrinkling in spinning also differs from uniform annular buckling because the roller applies localized and moving contact. During each revolution, a material point in the unsupported rim can experience bending, reverse bending, compression, tension, shearing, unloading, and partial recovery [8,12]. For this reason, wrinkling needs to be examined through the pass-resolved deformation history rather than only through the final rim shape. Feed ratio is particularly important because a higher feed per revolution increases the deformation imposed during each local roller passage and accelerates instability accumulation in the flange [13]. Severe flange wrinkling is critical because small waves may be reduced by later roller action, whereas severe wrinkles can remain as permanent defects and reduce forming quality [14].

Recent work has shown that the deformation mode and wall-thickness variation in conventional spinning are not constant during forming [15]. Shear deformation, compression-shear deformation, and tension-shear deformation can appear successively as the flange constraint evolves during the pass [15]. A strain-based wrinkling criterion has also been proposed for spinning, where wrinkle initiation is associated with the circumferential strain history in the unsupported flange during roller feeding [16]. This view is relevant because hoop-strain recovery can be extracted from finite element (FE) analysis.

Several methods have been proposed to delay flange wrinkling. Toolpath design can reduce harmful circumferential compression by controlling local deformation, forming depth, and contact direction [6,11]. Blank-holder-assisted spinning [17] and flange-constrained spinning

[18] can increase the effective stiffness of the unsupported rim and delay instability. Intermediate path design can also affect post-wrinkling development by changing wrinkle amplitude and peak number in multi-pass spinning [19]. Studies on shear-spinning forming limits further show that process windows depend on the combined effects of feed rate, radial force, roller attack angle, and thickness reduction [4]. These works indicate that flange stability depends on the imposed path, support condition, material state, and forming parameters.

Microhardness mapping provides an experimental basis for comparing retained local strengthening after edge preforming, although it does not directly represent the local stress or strain field. The literature has established a relationship between hardness and flow stress in metals, and studies in metal-forming have shown that Vickers hardness can be used to assess changes in material resistance to plastic deformation [20]. In the present work, microhardness mapping is therefore used as a comparative descriptor of retained strengthening near the flange root and curvature band, and is combined with finite element estimates of equivalent plastic strain and hoop-strain history to evaluate how each edge-preforming route modifies the blank before the subsequent spinning pass.

Most wrinkling studies consider blanks that enter the forming pass as flat or nearly unconditioned sheets. Less attention has been given to modifying the flange root before a subsequent spinning pass. This point is important because the flange root and unsupported rim deform together during roller contact. If the flange root is prestrained and locally strengthened before the subsequent pass, the storage, redistribution, and recovery of hoop strain in the rim can change. More broadly, earlier deformation and modified stress states are known to affect forming force, formability, springback, and later bending response in metal forming [21].

Earlier work on flanged-edge blanks showed that adding a flange along the blank periphery can improve wrinkle resistance by increasing edge rigidity and bending stiffness [22]. However, that work mainly examined the benefit of adding a flange and did not establish full applicability to a complete multi-pass conventional-spinning route. Progressive inward material flow, final blank diameter reduction, wall-thickness evolution, residual stress development, and final part accuracy over several passes remain necessary for complete process validation [23]. This distinction is important in the present paper because improved rim stability during one investigated pass cannot be used alone as evidence that a complete conventional-spinning route can be achieved.

This study examines how the edge-preforming route affects pre-strain development and local strengthening at the flange root, and how this inherited condition influences wrinkling during a subsequent spinning pass of AA5052-O blanks. Two edge-preforming routes are compared. Edge forming by bending (EFB) forms the edge mainly through localized bending near the flange root. Edge forming by spinning (EFS) introduces travelling roller contact along the edge-forming path. Although both routes produce a flanged edge, they generate different pre-strain distributions and strengthening levels in the curvature band. Therefore, visible flange geometry alone cannot define the blank condition before the subsequent pass.

Controlled spinning experiments, Vickers microhardness mapping, and three-dimensional FE analysis are combined to evaluate these effects. Microhardness mapping compares the local strengthening retained in the flange root and curvature band after edge preforming. The FE model examines equivalent plastic strain after preforming and hoop-strain evolution during the subsequent spinning pass. The wrinkling response is assessed using final defect classification and hoop-strain recovery. The main contribution is to connect the edge-preforming route, the inherited flange-root condition, and pass-level wrinkle suppression during the investigated spinning pass.

4.3 Materials and methodology

4.3.1 Material and tensile characterization

The workpiece material was AA5052-O aluminium alloy sheet in the fully annealed condition. Circular blanks with a nominal thickness of 1.0 mm and an initial diameter of 180 mm were prepared for the edge-preforming and subsequent spinning tests. Tensile specimens were machined along the rolling direction and tested at room temperature under quasi-static loading. The measured engineering stress–strain response was converted into true stress–true plastic strain form and used to identify the material parameters adopted in the FE model.

The plastic response was represented using the Hollomon law:

$$\bar{\sigma} = K\bar{\varepsilon}_p^n \tag{4.1}$$

where $\bar{\sigma}$ is the true stress and $\bar{\varepsilon}_p$ is the equivalent plastic strain. This constitutive description is used subsequently in the FE model and follows the modelling basis used for the present material system in previous work [22]. Figure 4.1 shows the tensile response of AA5052-O adopted in the present study.

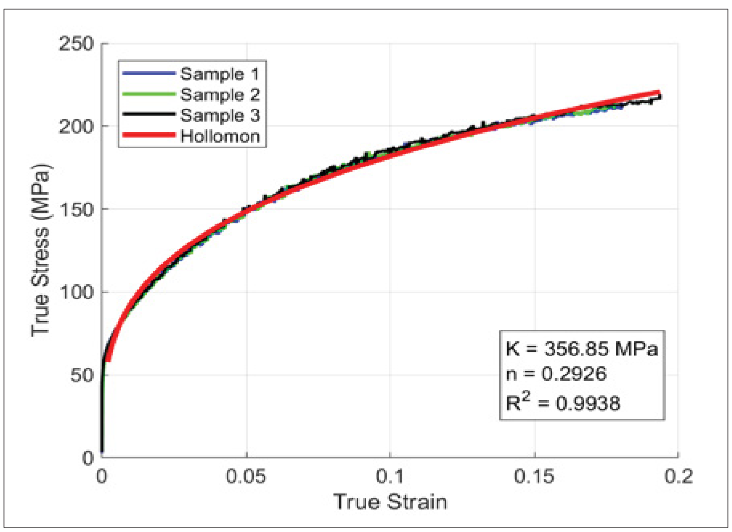

Figure 4.1 Tensile test of aluminum alloy AA5052-O [33]

4.3.2 Edge preforming methods and process variables

Two edge preforming routes were investigated in this study, namely edge forming by bending (EFB) and edge forming by spinning (EFS). Both routes were designed to produce a flanged edge before the subsequent spinning pass. However, they differ in the direction of roller motion and in the local deformation history imposed near the flange root. This distinction is important because the subsequent wrinkling response is expected to depend not only on the final flange geometry, but also on the pre-strain and local strengthening retained in the curvature band.

All preforming trials were carried out on the same CNC spinning machine under identical clamping and oil lubrication conditions. The tooling system consisted of a 30° conical mandrel, a forming roller with a diameter of 100 mm and a nose radius of 6 mm, and interchangeable backup rollers. Three backup roller curvature radii were examined, R2, R4, and R6, together with two target flange angles, 40° and 45°. The backup roller angle was fixed at 45° for all tests. The target flange angle was imposed through the programmed roller trajectory. The complete experimental matrix for the preforming stage is given in Table 4.1.

Table 4.1 Experimental edge-preforming matrix

Route	Backup roller radius	Flange angle α
EFB or EFS	R2, R4 or R6	40° or 45°

The common tooling arrangement is shown in Figure 4.2. Figure 4.2(a) presents the CNC spinning machine, Figure 4.2(b) shows the experimental setup with the clamped blank and tooling arrangement, and Figure 4.2(c) shows the interchangeable backup rollers with radii R2, R4, and R6.

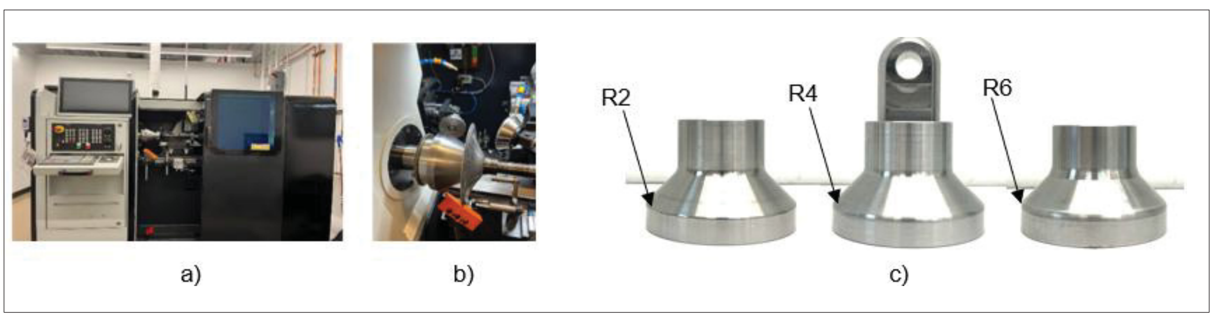

Figure 4.2 Experimental equipment an d tooling used in the spinning tests
a) spinning machine, b) experimental setup for the spinning trials and (c) backup rollers with different radii, denoted as R2, R4, and R6

The route schematics are shown in Figure 4.3. In EFB, the forming roller advances parallel to the mandrel axis, and the edge is formed mainly by localized bending near the flange root. In EFS, the roller advances parallel to the local surface direction of the backup roller, producing travelling contact along the edge forming path. Therefore, although EFB and EFS generate comparable flanged edge geometries, they do not impose the same local deformation mode.

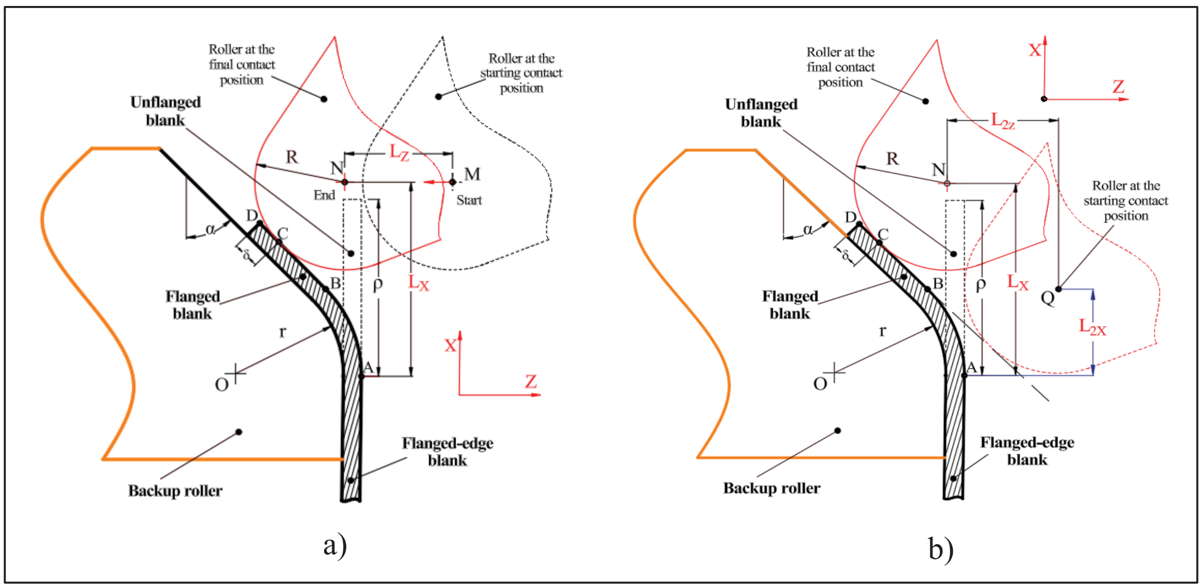

Figure 4.3 Schematics of a) EFB and b) EFS

For both routes, the roller mandrel gap during preforming was set equal to the initial sheet thickness in order to maintain a consistent through thickness forming condition. The preforming spindle speed and feed ratio were fixed at 400 rpm and 1 mm/rev, respectively. These constant process settings were used to ensure that the comparison between EFB and EFS was governed mainly by the preforming route, backup roller radius, and target flange angle.

To describe the roller kinematics on a common basis without changing the route-specific geometry, the roller-center path was expressed in the machine X-Z plane using a cumulative toolpath coordinate s. For a given route j, where j= EFB or EFS, s is defined as:

$$s_j(t) = \int_0^t \sqrt{\left(\frac{dX_j}{d\tau}\right)^2 + \left(\frac{dZ_j}{d\tau}\right)^2}\, d\tau \tag{4.2}$$

where X_j and Z_j are the programmed roller-center coordinates for route j. The roller-center position along each route is then written as:

$$x_j(s) = \begin{bmatrix} X_j(s) \\ Z_j(s) \end{bmatrix}, \qquad 0 \le s \le s_{f,j} \tag{4.3}$$

where $s_{f,j}$ is the total programmed travel length required to reach the target flange angle for route j. The total route length is therefore:

$$s_{f,j} = \int_{\text{route}j} ds, \qquad j \in \{EFB, EFS\} \tag{4.4}$$

This formulation allows the two preforming routes to be compared using the same scalar path coordinate while preserving their different programmed directions of roller motion. Thus, the difference between EFB and EFS is introduced through the route specific roller centre path, not by assuming that the two routes generate the same deformation history.

4.3.3 Subsequent spinning tests and wrinkling classification

After edge preforming, the blanks were subjected to one subsequent spinning pass to evaluate how the inherited flange root and curvature band conditions affected rim stability. The same mandrel and primary forming roller were used for all blank conditions, so that the influence of the preforming route could be compared under the same tooling configuration. Three feed ratios were tested, namely 1.0, 1.5, and 2.0 mm/rev. The spindle speed during the subsequent pass was fixed at 200 rpm.

As shown in Figure 4.4, the roller centre followed the same straight trajectory parallel to the conical mandrel for the flat, EFB, and EFS blanks. The path started near the flange root entry region and continued toward the tailstock side rim. The pass geometry was therefore kept constant for all tested conditions. Only the roller mandrel clearance schedule was varied. This design allowed the effect of local support to be examined without changing the nominal toolpath.

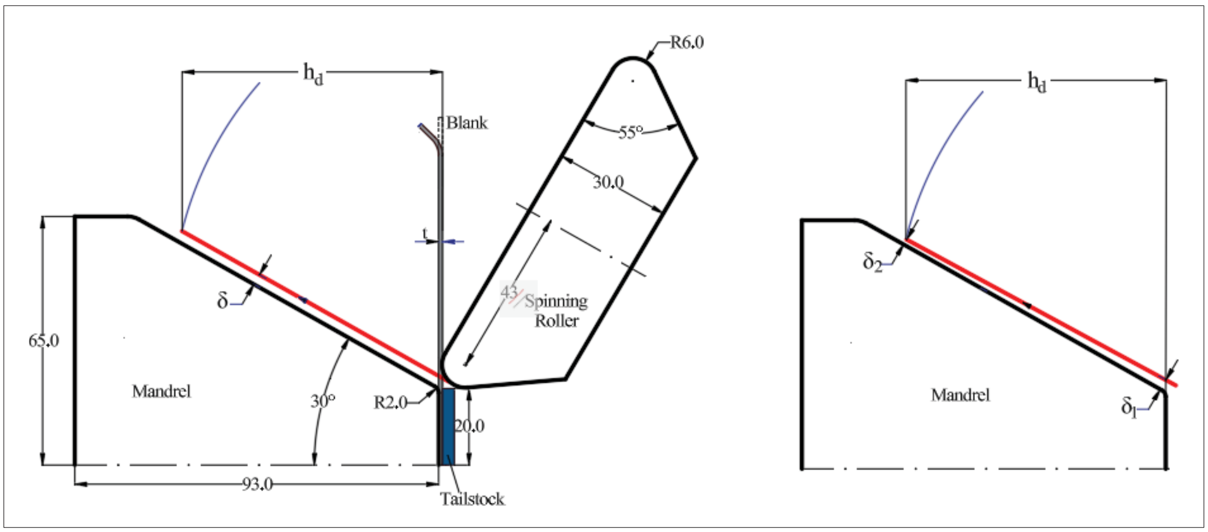

Figure 4.4 Common toolpath used in the subsequent spinning pass and roller–mandrel clearance schedules: (a) constant-gap schedule and (b) inclined-gap schedule. The roller path is identical in both cases; only the clearance evolution differs

The subsequent pass was used as a controlled comparative condition for evaluating the wrinkling response after edge preforming. It was not intended to validate a complete multi pass conventional spinning route. In particular, this section evaluates rim stability during the investigated pass, whereas the broader limits related to inward material flow, diameter reduction, wall thickness evolution, and final part accuracy are discussed in Section 4.5.4.

Two roller mandrel clearance schedules were considered. In the constant gap schedule, the clearance remained unchanged along the full pass. In the inclined gap schedule, the clearance decreased progressively from the initial clearance at the beginning of the pass to the final clearance at the end of the pass. The inclined gap schedule was introduced to increase local support progressively during forming while maintaining the same nominal roller trajectory. Therefore, Figure 4.4 compares two support conditions applied to the same pass geometry.

Wrinkling at the end of the main pass was quantified from the circumferential rim profile. The peak-to-valley waviness amplitude was calculated by Eq. (4.5).

$$\Delta = z_{\max} - z_{\min} \tag{4.5}$$

where $z_{\max}$ and $z_{\min}$ are the maximum and minimum axial positions measured along the circumferential rim profile after forming. To compare blanks with different local flange widths, the waviness amplitude was normalized using the local flange width L_f, giving the wrinkling index

$$I_w = \frac{\Delta}{L_f} \tag{4.6}$$

where I_w is the normalized wrinkling index and L_f is measured from the final cross-section along the mid-thickness path between the flange-root transition and the rim.

The final wrinkling state was classified using the normalized wrinkling index,

$$\textit{Wrinkling state} = \begin{cases} \textit{wrinkle-free}, & I_w < I_{w,L} \\ \textit{slight wrinkling}, & I_{w,L} \le I_w < I_{w,U} \\ \textit{severe wrinkling}, & I_w \ge I_{w,U} \end{cases} \tag{4.7}$$

where $I_{w,L}$ and $I_{w,U}$ are the lower and upper classification thresholds. The same thresholds were applied to all blank conditions in order to maintain a consistent basis for comparing the pass level wrinkling response.

This classification was used to assess relative rim stability during the investigated pass. Severe wrinkling was treated as a critical instability during this pass, not as a successful forming condition. The classification therefore provides a comparative measure of wrinkle suppression for the tested process window, while complete process applicability is addressed separately in the discussion.

4.3.4 Microhardness mapping and curvature-band descriptors

Vickers microhardness mapping was used to characterize the local strengthening introduced by edge preforming. The purpose of this measurement was to compare the inherited mechanical condition in the flange root and curvature band before the subsequent spinning pass. Since EFB and EFS can generate a similar flanged edge geometry while imposing different local deformation histories, hardness mapping was used as an experimental indicator of the local strengthening retained after preforming.

Measurements were performed on polished meridional cross sections extracted from the preformed blanks. The section geometry was described in the R−Z plane, where R denotes the radial direction and Z denotes the axial direction. Indentations were performed using the HV0.1 condition with a 100 gf load. The measurement region covered the parent sheet, the flange root, the curvature band, and the adjacent rim region, as illustrated in Figure 4.5. For reproducibility, a total of 6 indentation points were used for each mapped section. The measurement was repeated on 3 specimen sections for each selected condition. The base material hardness, HV_0, was measured away from the flange root region.

To compare EFB and EFS on a consistent geometric basis, a local reference system was defined from the flange root. The flange root reference point was selected at the transition between the near flat parent sheet and the curvature band. This reference point was used because small differences in the final preformed profile may occur between routes, backup roller radii, and target flange angles. Therefore, the measurement positions were compared relative to the local curvature band geometry rather than only by their absolute coordinates in the machine frame.

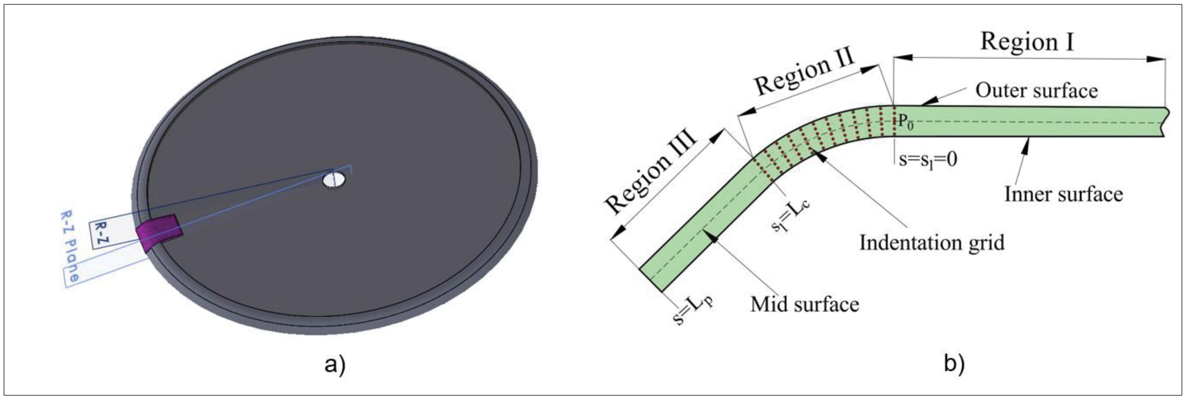

Figure 4.5 Microhardness mapping methodology and representative hardness distributions: (a) specimen extraction from the preformed blank and (b) meridional cross-section showing the indentation layout across the sheet, curvature band, and rim

A normalized arc length coordinate was defined along the mid thickness path of the curvature band as

$$\lambda = \frac{s_i}{L_{CB}} \tag{4.8}$$

where s_i is the local arc length from the flange-root reference point to sampling location *i*, and L_{CB} is the total mid-thickness arc length of the curvature band. With this definition, $\lambda = 0$ corresponds to the flange-root reference point, while $\lambda = 1$ corresponds to the outer end of the curvature band.

Two scalar descriptors were then defined to summarize the inherited curvature-band condition. The first descriptor was the mean equivalent plastic strain in the curvature band, obtained from the FE-estimated strain field at the sampling positions:

$$\bar{\varepsilon}_{p,CB} = \frac{1}{N}\sum_{i=1}^{N}\bar{\varepsilon}_{p,i} \tag{4.9}$$

where N is the number of sampling locations in the curvature band and $\bar{\varepsilon}_{p,i}$ is the equivalent plastic strain at sampling location i. This descriptor represents the average pre-strain introduced into the curvature-band region during edge preforming.

The second descriptor was the normalized curvature-band hardness ratio:

$$H_{CB}^{*} = \frac{\bar{H}_{CB}}{HV_0} \tag{4.10}$$

where $\bar{H}_{CB}$ is the mean Vickers microhardness measured in the curvature band and HV_0 is the base-material hardness measured away from the flange-root region. Reporting H_{CB}^{*} reduces the influence of small variations in the absolute hardness level and provides a consistent basis for comparing EFB and EFS.

The hardness ratio was not treated as a direct substitute for the local stress or strain field. Instead, it was used together with the FE estimated equivalent plastic strain to assess how each preforming route modified the curvature band before the subsequent spinning pass. This combined assessment connects the experimentally measured local strengthening with the numerically estimated pre-strain retained near the flange root, which is related to the pass resolved hoop strain response and wrinkling classification.

4.3.5 Finite element model

Three-dimensional explicit FE simulations were performed for the edge-preforming step and the subsequent spinning pass to support interpretation of the experimental results and to extract local deformation histories that cannot be measured directly during forming. The numerical framework followed the previously validated model developed for the same AA5052-O material system and spinning configuration [22]. The simulations were conducted in LS-DYNA. The blank was modelled as a deformable body, whereas the mandrel and rollers were treated as rigid bodies. The blank was discretized using eight-node solid elements with three elements through the thickness. A central hole with a diameter of 34 mm was introduced to represent the clamped region, and the nodes along this inner boundary were fixed [22].

The simulation procedure consisted of two sequential stages, as shown in Figure 4.6. In the first stage, the edge-preforming operation was simulated according to the programmed kinematics of either EFB or EFS. In the second stage, the deformed blank obtained after edge preforming was imported as the initial blank condition for the subsequent spinning pass. This transfer retained both the preformed geometry and the plastic strain field generated during edge preforming. Therefore, the subsequent numerical response included the inherited curvature-band condition produced by each preforming route.

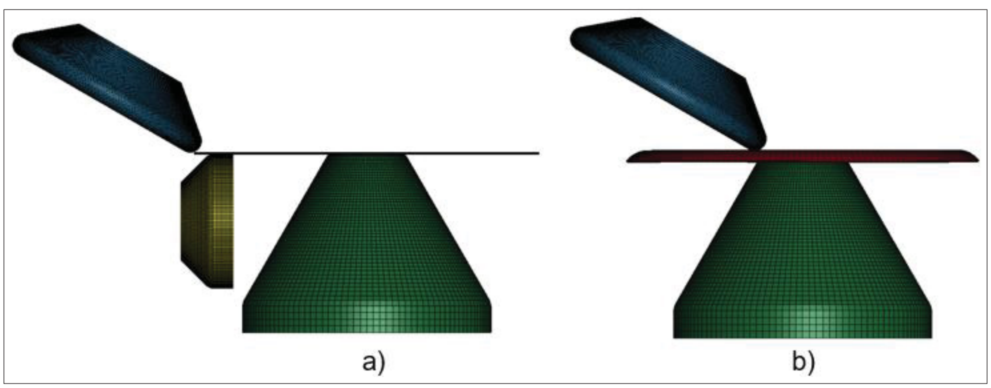

Figure 4.6 Two-stage FE framework used in the present study: (a) edge-preforming simulation, in which the route-specific EFB or EFS deformation is imposed, and (b) subsequent spinning simulation, in which the inherited geometry and plastic strain from preforming are retained as the initial state

The mesh strategy, contact treatment, and friction conditions were kept consistent with the previously validated model [22]. Loading-rate scaling by a factor of 10 was used to improve computational efficiency while preserving the quasi-static character of the deformation. The same scaling factor was applied to all simulated cases so that the comparison among the flat, EFB, and EFS blanks was not affected by different numerical acceleration conditions.

In this study, the FE model was used mainly to extract the pass resolved hoop strain history in the wrinkling prone outer flange region. This choice follows the strain based wrinkling approach proposed by Li and Long [16], in which the circumferential strain history in the unsupported flange is used to identify the beginning of wrinkle development during spinning. Therefore, the present study does not introduce an independent critical hoop stress threshold. Instead, the hoop strain response is used as the primary numerical indicator for comparing when each blank condition begins to lose cyclic recovery during the investigated pass.

For each simulated case, a representative sensor element was selected near the unsupported rim where wrinkling was observed experimentally. The hoop strain at this location was extracted as a function of forming time or normalized forming height. The same sensor selection procedure was applied to the flat, EFB, and EFS cases to maintain a consistent comparison. The extracted strain history was then used in Section 4.3.6 to calculate the cycle resolved hoop strain descriptors and to identify the first sustained loss of hoop strain recovery. Figure 4.7 defines the sensor location, the local hoop strain directions, and the reference instants used for post-processing.

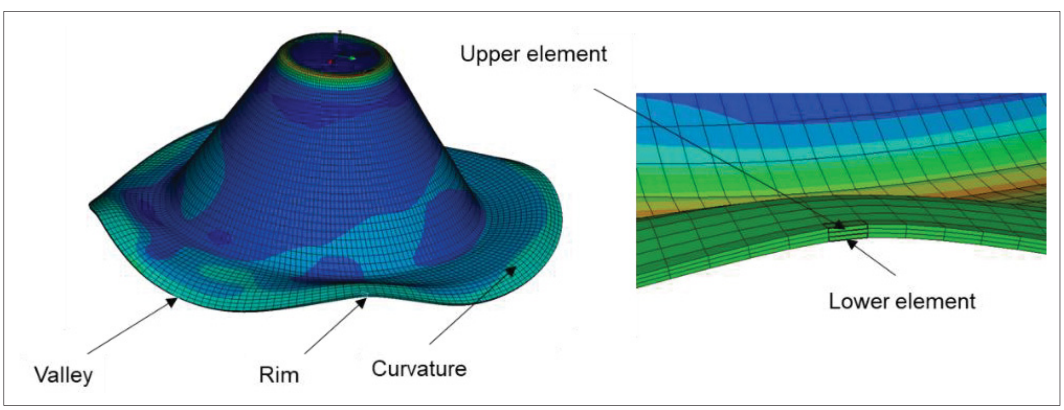

Figure 4.7 Definition of the representative sensor element in the FE model and reference cycle instants used for pass-resolved post-processing. The cycle is divided into a contact interval and a subsequent recovery interval

The FE results were used as local deformation indicators, not as a stand alone forming limit model. The final experimental rim profile classification remained the basis for confirming the observed wrinkling state. In this way, the numerical model was used to connect the inherited edge preformed condition with the timing of hoop strain accumulation and loss of cyclic recovery during the subsequent spinning pass.

4.3.6 Pass-resolved instability descriptors

During the subsequent spinning pass, the unsupported rim is subjected to repeated local loading and unloading as the roller approaches, contacts, and leaves a given material point. Under this moving contact condition, the rim does not deform through a single monotonic loading path. Instead, each material point experiences a local cycle composed of roller contact, strain excursion, unloading, and partial recovery before the next roller passage. Therefore, wrinkle initiation was evaluated from the cycle resolved hoop strain history of a representative rim element rather than from the final deformed shape alone.

The hoop strain, ε_θ, was extracted from the FE model at the same rim sensor location for all blank conditions. The subscript θ denotes the circumferential direction, and the cycle index k denotes the mandrel revolution. The same extraction procedure was applied to the flat, EFB, and EFS blanks so that the wrinkle initiation position could be compared on a common basis.

For each revolution, three reference instants were defined from the local roller blank interaction. The pre-contact instant, t_k^-, corresponds to the state immediately before the roller reaches the selected rim element. The post contact instant, t_k^+, corresponds to the state immediately after the roller passes the selected element. The next pre-contact instant, t_{k+1}^-, corresponds to the state carried into the following roller passage. The corresponding hoop strain states are

$$\varepsilon_{\theta,k}^{-} = \varepsilon_{\theta}\left(t_{k}^{-}\right) \tag{4.11}$$

$$\varepsilon_{\theta,k}^{+} = \varepsilon_{\theta}\left(t_{k}^{+}\right) \tag{4.12}$$

$$\varepsilon_{\theta,k+1}^{-} = \varepsilon_{\theta}\left(t_{k+1}^{-}\right) \tag{4.13}$$

The interval from t_k^- to t_k^+ represents the contact driven part of the cycle, while the interval from t_k^+ to t_{k+1}^- represents the recovery part of the cycle. This separation allows the strain imposed by roller contact to be distinguished from the strain retained after unloading.

The contact-induced hoop-strain increment was defined as

$$\Delta\varepsilon_{\theta,k}^{con} = \varepsilon_{\theta,k}^{+} - \varepsilon_{\theta,k}^{-} \tag{4.14}$$

This descriptor quantifies the hoop-strain change imposed by local roller contact during revolution *k*. The recovery hoop-strain increment was defined as

$$\Delta\varepsilon_{\theta,k}^{r} = \varepsilon_{\theta,k+1}^{-} - \varepsilon_{\theta,k}^{+} \tag{4.15}$$

which represents the strain change after roller separation and before the next contact. The most compressive hoop strain reached during the same revolution was defined as

$$\varepsilon_{\theta,k}^{\min} = \min_{t_k^- \le t \le t_{k+1}^-} \varepsilon_{\theta}\left(t\right) \tag{4.16}$$

This value identifies the largest compressive excursion experienced by the selected rim element during one contact and recovery cycle. However, this value was not used alone to define wrinkle initiation because a large compressive excursion does not necessarily produce instability if the rim recovers before the next roller passage.

To determine whether the rim progressively retained non-recovered hoop strain from one revolution to the next, the cycle-to-cycle drift of the pre-contact state was defined as

$$D_{\theta,k} = \varepsilon^{-}_{\theta,k+1} - \varepsilon^{-}_{\theta,k} \tag{4.17}$$

A small value of indicates that the rim element returns close to its previous cyclic reference state before the next roller passage. By contrast, a sustained positive or negative drift indicates that the rim does not fully recover after roller contact. A positive drift represents tensile accumulation, while a negative drift represents compressive accumulation. In the present analysis, the key indicator is not the sign alone, but the persistence of the drift over successive cycles.

The hoop-strain recovery ratio was defined as

$$R_{\theta,rec} = \frac{|\Delta\varepsilon^{r}_{\theta,k}|}{|\Delta\varepsilon^{c}_{\theta,k}|} \tag{4.18}$$

where values close to unity indicate that most of the contact induced hoop strain excursion is recovered before the next roller passage. Lower values indicate greater retention of non recovered deformation in the unsupported rim. This ratio was used as a comparative descriptor among the flat, EFB, and EFS blanks, rather than as an independent forming limit.

Wrinkle initiation was identified from the first sustained loss of cyclic hoop strain recovery in the selected rim element. In a stable response, the hoop strain may vary strongly during roller contact, but it returns close to a stationary local reference level after the roller leaves the element. This reference level does not have to be zero because the rim may already contain inherited strain from edge preforming or from earlier stages of the same pass. Therefore, the criterion does not require the hoop strain to recover exactly to zero. The response is considered stable when ε_{θ} oscillates around a nearly stationary reference level without sustained cycle to cycle drift.

By contrast, wrinkle initiation is assigned when the hoop strain changes during roller contact and does not return close to its previous pre-contact state during recovery. If this non recovered state remains in the following cycle or in successive cycles, the selected rim element is considered to have reached the wrinkle initiation condition. The accumulated strain after initiation may develop toward either tensile or compressive drift. In both cases, the common mechanical feature is the loss of cyclic hoop strain recovery.

The wrinkle initiation position was recorded using the forming height associated with the first sustained non recovered state,

$$h_{wi} = h\left(k_{wi}\right) \tag{4.19}$$

where k_{wi} is the first cycle satisfying the sustained non-recovery condition. The same criterion was applied to the flat, EFB, and EFS blanks so that the initiation position could be compared on a common pass-resolved basis.

Figure 4.8 illustrates the one cycle hoop strain history used for this analysis. It defines the pre-contact, post contact, and next pre-contact states, together with the contact interval, the recovery interval, the contact induced strain increment, the recovery increment, and the sustained drift used to identify wrinkle initiation.

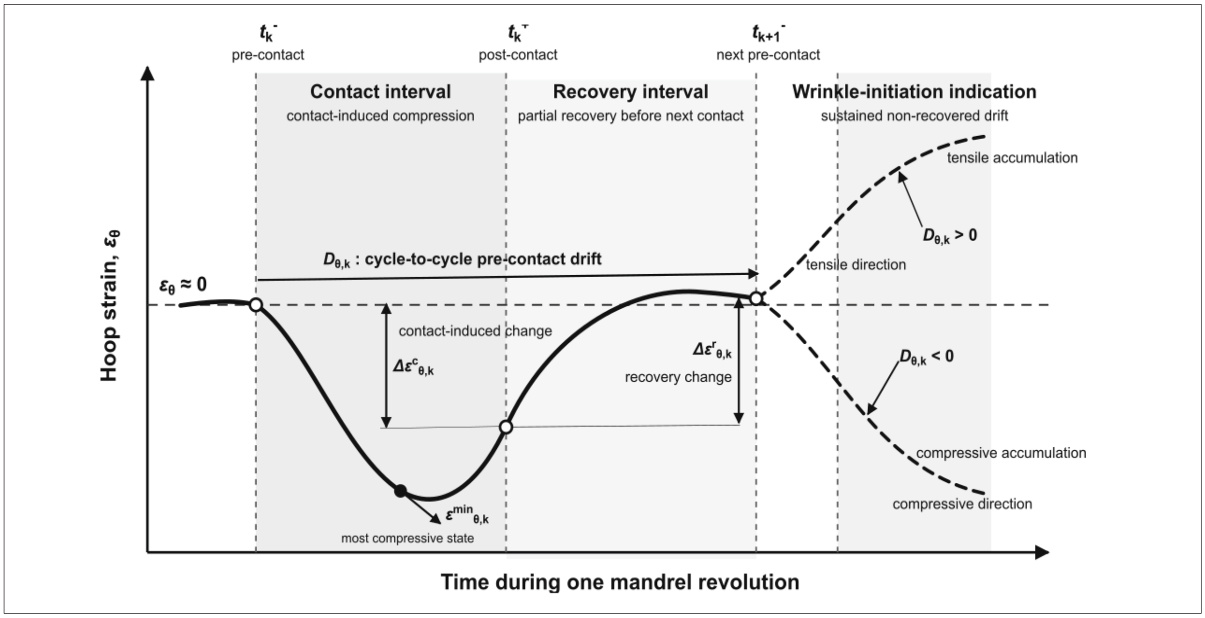

Figure 4.8 Schematic one-cycle hoop-strain history showing the pre-contact, post-contact, and next pre-contact instants, together with the contact-induced compression interval and the subsequent recovery interval

Figure 4.9 summarizes the workflow linking the inherited blank condition, FE extracted hoop strain history, cycle partitioning, recovery descriptors, wrinkle initiation position, and final experimental rim profile classification.

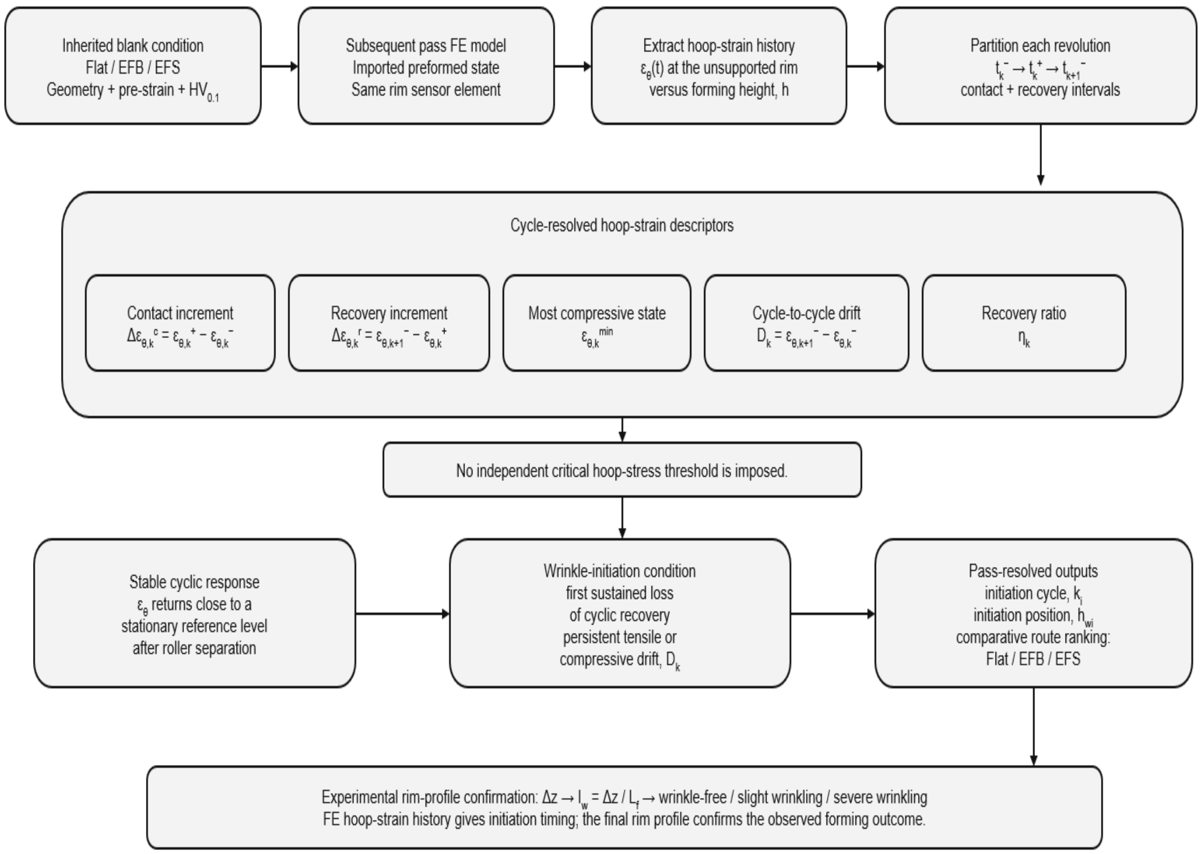

Figure 4.9 Post-processing workflow used to determine the pass-resolved wrinkling state during the subsequent spinning pass. The workflow links the inherited blank condition, FE-extracted hoop-strain history, cycle partitioning, recovery descriptors, sustained non-recovered drift, wrinkle-initiation position, and final experimental rim-profile classification

The FE-based hoop-strain criterion was used to identify the stage at which each blank condition started to lose rim stability during the investigated pass. The final rim-profile classification was retained as the experimental evidence for confirming the forming result. This approach connects the inherited edge-preformed condition to the timing of hoop-strain accumulation while avoiding the introduction of an unvalidated critical hoop-stress threshold.

4.4 Results

4.4.1 Curvature-band conditioning after edge preforming

The first set of results examines the mechanical condition introduced in the curvature band by EFB and EFS. This region is located between the flange root and the unsupported rim, and it is carried into the subsequent spinning pass as part of the inherited blank condition. This subsection therefore focuses on the preformed state before the subsequent pass begins.

Figure 4.10 shows the stage resolved equivalent plastic strain fields obtained from the FE simulations for the representative R6 backup roller condition. For both preforming routes, plastic strain develops progressively as the edge is formed. However, the spatial distribution of the plastic strain differs between EFB and EFS. In EFB, the equivalent plastic strain remains concentrated near the flange root transition. This localized strain field is consistent with the bending dominated nature of the route. In EFS, the strain field extends over a larger portion of the curvature band, which is consistent with the travelling roller contact imposed along the edge forming path.

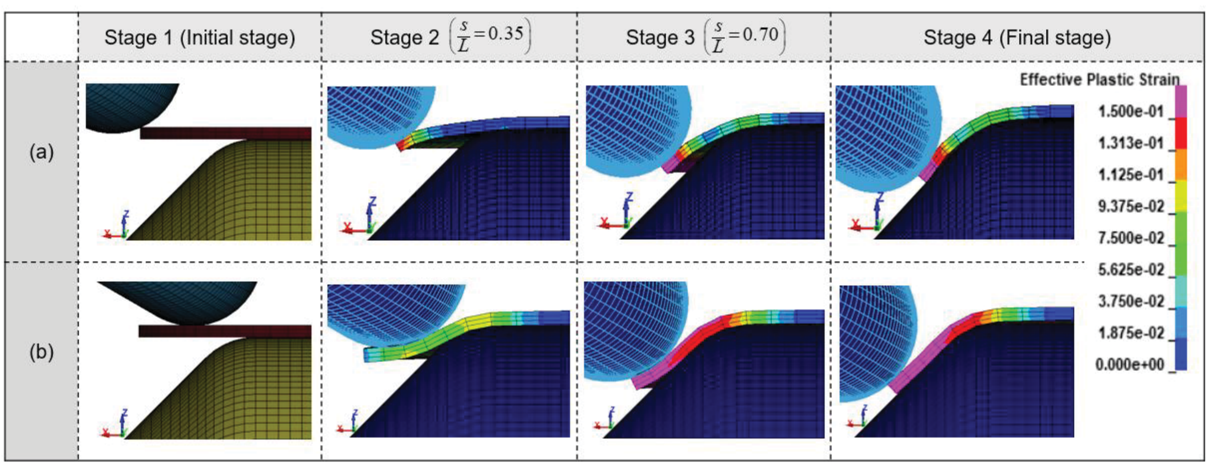

Figure 4.10 Stage-resolved equivalent plastic strain fields during edge preforming for the representative case with $\alpha = 45^{\circ}$ and backup-roller radius R6; a) EFB and b) EFS

The microhardness results in Figure 4.11 provide experimental evidence of the local strengthening retained after edge preforming. For all preformed blanks, the curvature band hardness is higher than the base material hardness measured away from the flange root region. This confirms that both EFB and EFS introduce local strengthening in the curvature band. Under comparable backup roller radius and flange angle conditions, EFS gives higher mean curvature band hardness than EFB, indicating stronger retained local strengthening after the preforming step.

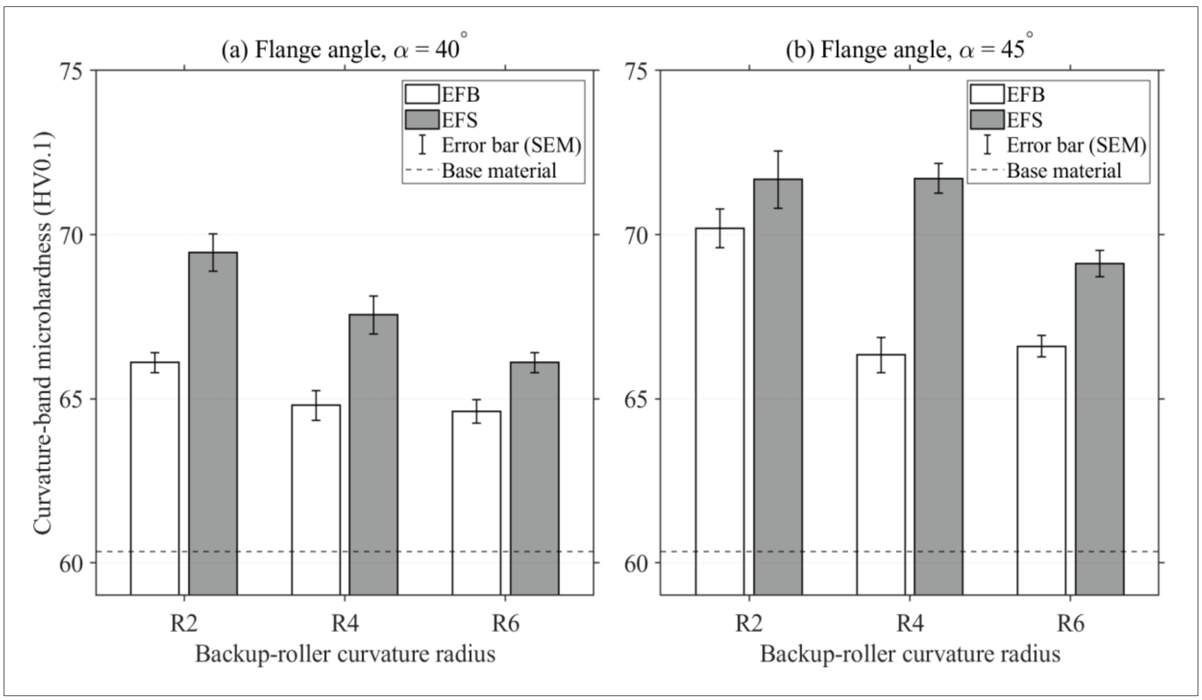

Figure 4.11 Curvature-band microhardness, HV0.1, for EFB and EFS as a function of backup-roller radius R2, R4, and R6 and target flange angle. Bars represent the mean hardness over the curvature-band indentation set, and error bars represent ±1 standard deviation

Figure 4.12 compares the equivalent plastic strain distribution along the normalized curvature band coordinate defined in Eq. (4.8). The EFB curves show a narrower high strain region located close to the flange root reference point. In contrast, the EFS curves show elevated equivalent plastic strain over a larger portion of the curvature band. The route effect is therefore not limited to the maximum strain value. It also affects the spatial extent of the prestrained zone. This distinction is important because two blanks with similar final flange geometry can carry different mechanical states into the subsequent spinning pass.

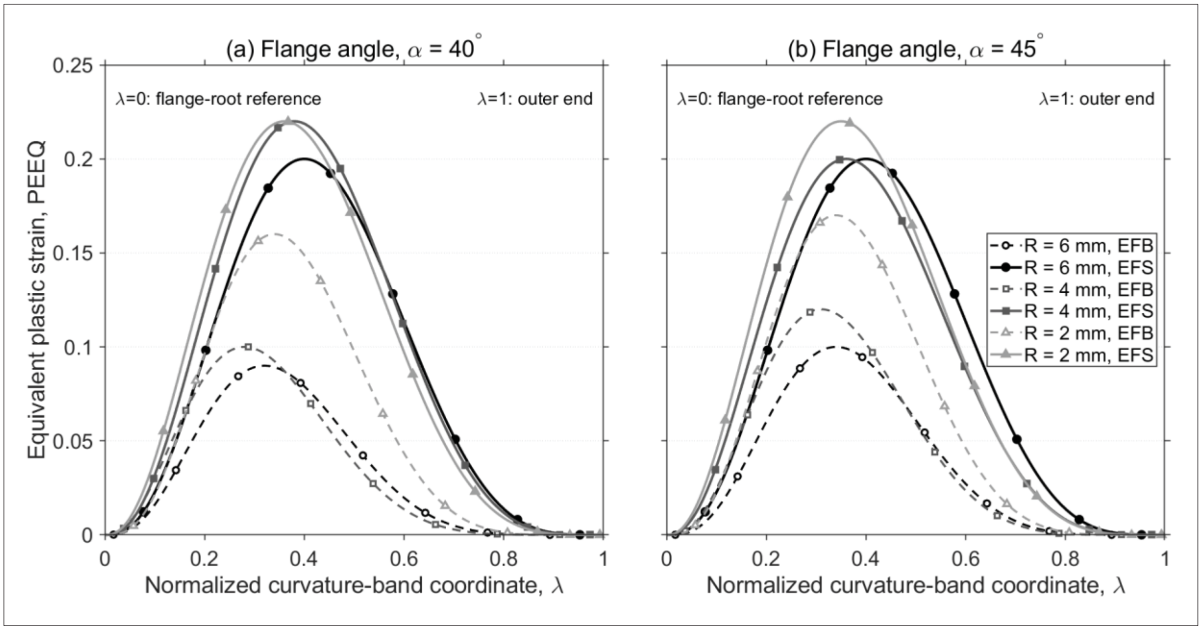

Figure 4.12 Peak equivalent plastic strain (PEEQ) distribution along the normalized curvature-band coordinate after edge preforming for EFB and EFS. The coordinate $\lambda = 0$ corresponds to the flange-root reference point, and $\lambda = 1$ corresponds to the outer end of the curvature band

Table 4.2 summarizes the quantitative descriptors of the inherited curvature band condition for the tested preforming routes, backup roller radii, and flange angles. The table includes the mean equivalent plastic strain in the curvature band, the peak equivalent plastic strain (PEEQ), the mean microhardness, and the hardness ratio. These descriptors show that the preforming route and backup roller radius both affect the inherited curvature band condition. Across the tested conditions, EFS generally produces higher mean PEEQ, higher peak PEEQ, and higher hardness ratio than EFB. The backup roller radius R2, R4, and R6 further modifies the local severity of curvature band conditioning, but it does not remove the route dependent difference between EFB and EFS.

These results show that EFB and EFS do not generate the same inherited blank condition, even when both routes produce a flanged edge. EFB produces a more localized conditioned zone near the flange root, while EFS produces a broader prestrained and locally strengthened curvature band. This difference provides the basis for the subsequent comparison of pass level wrinkling response and hoop strain recovery.

Table 4.2 Quantitative descriptors of the inherited curvature-band condition after edge preforming

Route	Radius	Flange angle	PEEQ in curvature band	Peak PEEQ	Microhardness HV0.1	Hardness ratio
EFB	R6	40°	0.0341	0.09	64.606	1.071
EFS	R6	40°	0.0791	0.20	66.096	1.095
EFB	R4	40°	0.0366	0.10	64.79	1.074
EFS	R4	40°	0.0863	0.22	67.55	1.119
EFB	R2	40°	0.0614	0.16	66.096	1.095
EFS	R2	40°	0.0854	0.22	69.449	1.151
EFB	R6	45°	0.0384	0.10	66.596	1.104
EFS	R6	45°	0.0791	0.20	69.108	1.145
EFB	R4	45°	0.0450	0.12	66.327	1.099
EFS	R4	45°	0.0776	0.20	71.711	1.188
EFB	R2	45°	0.0652	0.17	70.189	1.163
EFS	R2	45°	0.0849	0.22	71.677	1.188

4.4.2 Experimental forming outcomes at the discriminating feed ratio

The second set of results evaluates whether the inherited curvature band conditions identified in Section 4.4.1 are reflected in the final wrinkling response after the subsequent spinning pass. The forming state was classified from the final circumferential rim profile. The peak to valley waviness amplitude, Δ, was normalized by the local flange width, L_f, according to Eq. (4.6), and the resulting wrinkling index, I_W, was used for the classification defined in Eq. (4.7). The same classification limits were applied to all flat, EFB, and EFS blanks to maintain a consistent comparison of pass level wrinkling resistance.

The preliminary feed ratio screening showed that the tested process window included both stable and critical forming conditions. At a feed ratio of 1.0 mm/rev, most cases remained stable, which limited the ability to distinguish the effect of the preforming route. At 2.0 mm/rev, the imposed deformation became excessive, and cracking or severe damage occurred in the most critical cases. Therefore, a feed ratio of 1.5 mm/rev was selected as the discriminating condition. This feed ratio was severe enough to reveal differences among blank conditions while still allowing the effects of preforming route and roller mandrel gap schedule to be compared.

Table 4.3 summarizes the forming results obtained at this feed ratio. A consistent route dependent order is observed within the tested process window. EFS provides the highest resistance to wrinkling, EFB gives an intermediate response, and the flat blank reference remains the most critical condition. This order is maintained under both constant gap and inclined gap schedules. The gap schedule changes the severity of rim waviness, but it does not reverse the effect introduced by the inherited preformed state.

For the 40° flange angle, the response is highly sensitive to both preforming route and clearance schedule. Under the constant gap schedule, the EFB blanks remain in the severe wrinkling range for all three backup roller radii. Under the same flange angle, the EFS blanks show reduced wrinkling severity, with the strongest improvement observed among the preformed cases. When the inclined gap schedule is applied, the EFB cases shift toward lower wrinkling severity, while the EFS cases move further toward the wrinkle free range. This comparison shows that the inclined gap schedule improves pass level stability near the wrinkling limit, but the route effect remains evident.

For the 45° flange angle, the forming response becomes more stable for both EFB and EFS. The EFS cases reach the wrinkle free range for R2, R4, and R6 under both clearance schedules. The EFB cases also improve compared with the 40° condition, but they remain mainly in the slight wrinkling range. This result indicates that increasing the flange angle improves rim stability during the investigated pass, while the route dependent difference between EFB and EFS remains.

Table 4.3 Experimental forming outcomes at the discriminating feed ratio of 1.5 mm/rev, including the peak-to-valley waviness amplitude, local flange width, wrinkling index, and final classification

Flange angle	Radius	Route	Gap schedule	Δ (mm)	L_f (mm)	I_w	Class
40°	R6	EFB	Constant gap	7.2	10	0.72	Severe
40°	R6	EFB	Inclined gap	3.2	10	0.32	Slight wrinkling
40°	R6	EFS	Constant gap	3.1	10	0.31	Slight wrinkling
40°	R6	EFS	Inclined gap	2.8	10	0.28	Slight wrinkling
40°	R4	EFB	Constant gap	7	10	0.7	Severe
40°	R4	EFB	Inclined gap	3.1	10	0.31	Slight wrinkling
40°	R4	EFS	Constant gap	3	10	0.3	Slight wrinkling
40°	R4	EFS	Inclined gap	1	10	0.1	Wrinkle-free
40°	R2	EFB	Constant gap	6.7	10	0.67	Severe
40°	R2	EFB	Inclined gap	2.9	10	0.29	Slight wrinkling
40°	R2	EFS	Constant gap	1.1	10	0.11	Wrinkle-free
40°	R2	EFS	Inclined gap	0.9	10	0.09	Wrinkle-free
45°	R6	EFB	Constant gap	3.3	10	0.33	Slight wrinkling
45°	R6	EFB	Inclined gap	3	10	0.3	Slight wrinkling
45°	R6	EFS	Constant gap	1.1	10	0.11	Wrinkle-free
45°	R6	EFS	Inclined gap	0.9	10	0.09	Wrinkle-free
45°	R4	EFB	Constant gap	3.2	10	0.32	Slight wrinkling
45°	R4	EFB	Inclined gap	2.9	10	0.29	Slight wrinkling
45°	R4	EFS	Constant gap	1.1	10	0.11	Wrinkle-free
45°	R4	EFS	Inclined gap	0.9	10	0.09	Wrinkle-free
45°	R2	EFB	Constant gap	3	10	0.30	Slight wrinkling
45°	R2	EFB	Inclined gap	2.7	10	0.27	Slight wrinkling
45°	R2	EFS	Constant gap	1	10	0.1	Wrinkle-free
45°	R2	EFS	Inclined gap	0.8	10	0.08	Wrinkle-free

Figure 4.13 shows representative final rim morphologies corresponding to the classification used in Table 4.3 The wrinkle free cases show stable pass level forming within the tested condition. The slight wrinkling cases show limited circumferential waviness, whereas the severe wrinkling cases show larger and more irregular rim deformation. The severe cases correspond to nonuniform circumferential wrinkling during the investigated pass. Their uneven amplitudes indicate localized loss of flange stability rather than regular annular buckling or complete collapse of the workpiece.

The flat blank baseline provides a useful reference for separating the effect of the gap schedule from the effect of edge preforming. At the same discriminating feed ratio, the thinner flat blanks crack or wrinkle severely, whereas wrinkle-free forming is reached only for the thicker flat blank under the more favorable support condition. This comparison indicates that the improved response of the preformed blanks cannot be attributed to the inclined-gap schedule alone. The preforming route modifies the inherited flange-root condition before the subsequent pass, and this inherited condition affects the final wrinkling severity.

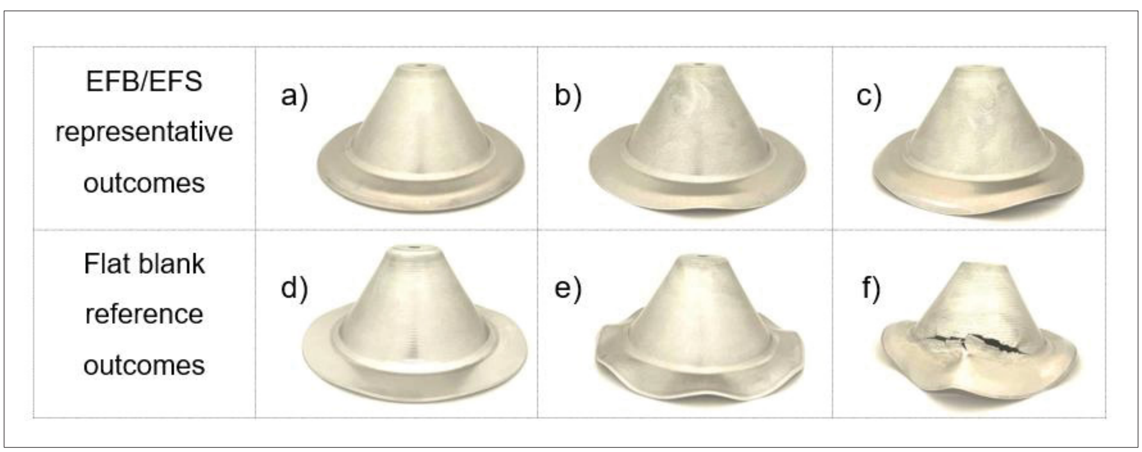

Figure 4.13 Representative final outcomes after the investigated subsequent spinning pass: (a) wrinkle-free preformed blank, (b) slight wrinkling in a preformed blank, (c) severe nonuniform circumferential wrinkling in a preformed blank, (d) wrinkle-free flat blank reference, (e) severe wrinkling in the flat blank reference, and (f) damaged flat blank reference

The experimental results show that edge preforming improves wrinkle resistance during the investigated subsequent spinning pass, with EFS providing the strongest improvement. However, these results must be considered as pass specific forming results. They do not demonstrate completion of a full multi pass conventional spinning route because total inward material flow, progressive blank diameter reduction, wall thickness evolution over successive passes, and final part accuracy were not evaluated.

4.4.3 Cycle-resolved hoop-strain reversibility

The experimental classification in Section 4.4.2 identifies the final wrinkling state after the subsequent spinning pass, but it does not show when the rim first begins to lose stability. To clarify this point, the hoop strain history was extracted from the representative rim element defined in the FE model. The analysis focuses on the recoverability of the unsupported rim after repeated roller contact, because the same material point experiences a sequence of contact, unloading, and partial recovery during each revolution.

Figure 4.14 presents the pass resolved hoop strain response for the representative R6 and 40° condition at a feed ratio of 1.5 mm/rev. This condition is useful because it is severe enough to distinguish the route dependent response of EFB and EFS. The full strain history shows that both preformed blanks undergo repeated hoop strain excursions during roller passage. However, wrinkle initiation is not identified only from the largest compressive strain reached during contact. A compressive excursion can still remain stable if the rim returns close to its previous pre-contact state before the next roller passage.

The local cycles shown in Figure 4.14 reveal the main difference between the two preforming routes. In the EFB blank, the next pre-contact state begins to shift from the previous reference level earlier in the pass. This indicates that part of the contact induced deformation remains stored in the rim after roller passage. In the EFS blank, this drift appears later, which means that the rim maintains cyclic recovery over a longer portion of the pass. This delayed loss of recovery is consistent with the experimental observation that EFS provides better wrinkling resistance than EFB under comparable conditions.

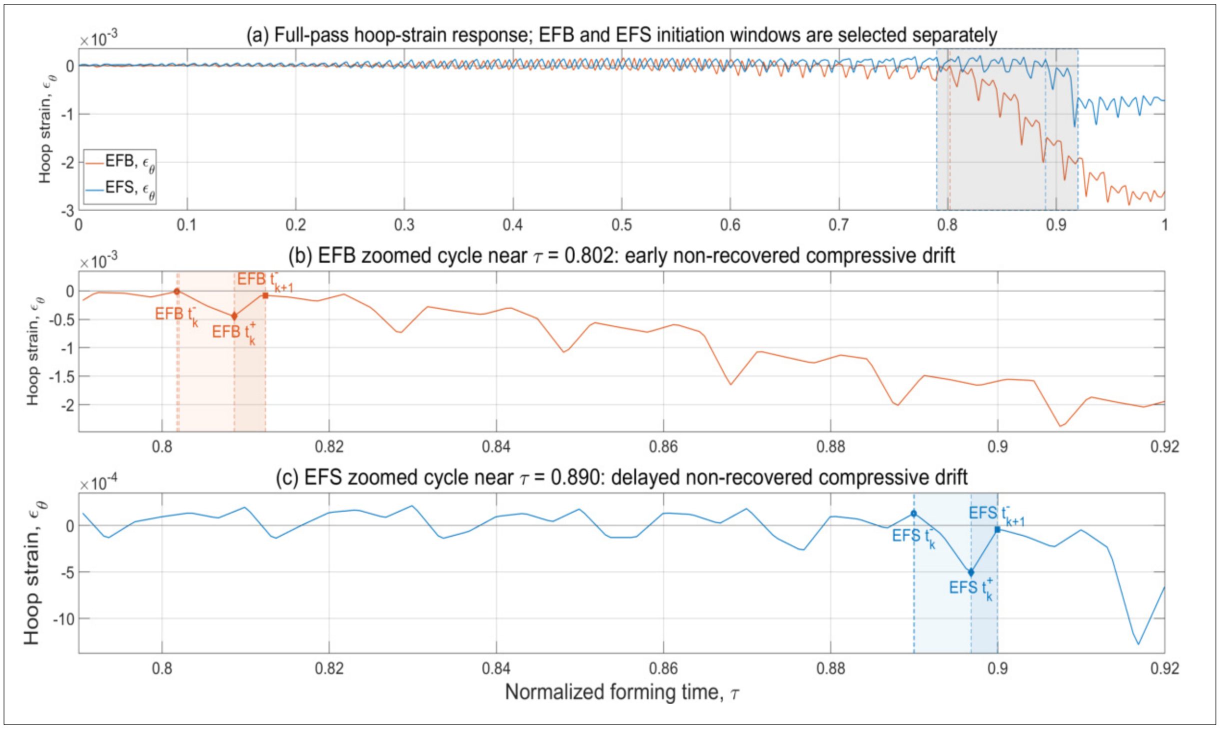

Figure 4.14 Pass resolved hoop strain history extracted from the representative rim element during the subsequent spinning pass for the R6 and 40° condition at f=1.5 mm/rev. The full pass response is shown in (a), while the selected local cycles for EFB and EFS are shown in (b) and (c), respectively. The pre-contact, post contact, and next pre-contact states indicate whether the rim recovers after roller passage or retains non recovered hoop strain. Sustained drift of the next pre-contact state marks the onset of loss of cyclic recovery in the unsupported rim

Figure 4.15 quantifies this response using the hoop strain recovery ratio. A higher value indicates that a larger part of the contact induced hoop strain excursion is recovered before the next roller passage. A lower value indicates greater retention of non recovered deformation. For the R6 and 40° condition, the EFB blank shows an earlier reduction in recovery ratio than the EFS blank. The same route dependent tendency is also observed for the R6 and 45° condition, where the EFS cases remain wrinkle free while the corresponding EFB cases show slight wrinkling.

These results show that the onset of wrinkling during the investigated pass is better described by sustained loss of hoop strain recovery than by peak compressive strain alone. The critical change occurs when the pre-contact state progressively shifts from one revolution to the next, because this means that the rim is no longer recovering from the previous roller passage. The FE results therefore support the experimental classification by showing how the inherited preformed state affects the timing of hoop strain accumulation.

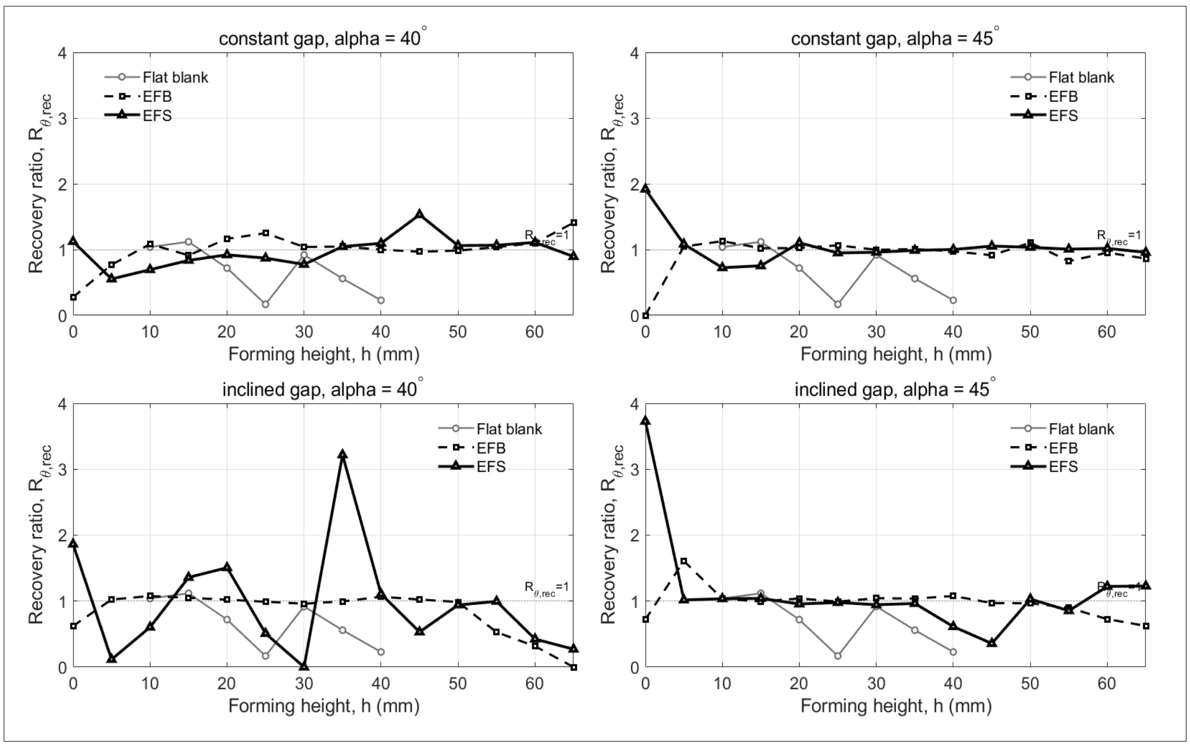

Figure 4.15 Hoop strain recovery ratio during the subsequent spinning pass for EFB and EFS blanks. A higher recovery ratio indicates stronger cyclic recovery of the unsupported rim after roller contact, whereas an early reduction indicates earlier retention of non recovered hoop strain and earlier loss of rim reversibility

4.4.4 Coupling curvature-band conditioning with pass-level stability

This section relates the inherited curvature band condition produced by edge preforming to the wrinkling response measured after the subsequent spinning pass. Figure 4.16 compares the mean curvature band microhardness with the normalized wrinkling index, I_w, for EFB and

EFS blanks formed with backup roller radii R2, R4, and R6. The four panels separate the 40° and 45° flange angles under the constant gap and inclined gap schedules. The horizontal reference lines define the wrinkle free, slight wrinkling, and severe wrinkling ranges used for the experimental classification.

For comparable radius, flange angle, and gap schedule, EFS generally gives higher curvature band microhardness and lower I_w than EFB. This agrees with Table 4.2, where EFS shows higher mean equivalent plastic strain, higher peak equivalent plastic strain, and a higher hardness ratio for most corresponding conditions. The result confirms that the final flange geometry alone cannot describe the blank condition before the subsequent pass. The route used to create the flange also controls the retained mechanical state of the curvature band.

The influence of backup roller radius is also reflected in Figure 4.16. In EFB, changing the radius modifies the local bending severity near the flange root, but the conditioned zone remains comparatively localized. In EFS, the travelling roller contact produces a broader conditioned region through the curvature band. This difference explains why EFS maintains lower I_w values than EFB across the tested radii.

The 40° condition provides the clearest route separation. Under the constant gap schedule, the EFB blanks remain in the severe wrinkling range for all three backup roller radii, whereas the corresponding EFS blanks show reduced wrinkling severity. With the inclined gap schedule, the EFB blanks shift toward the slight wrinkling range, while the EFS blanks approach or reach the wrinkle free range. Thus, the inclined gap schedule improves the support condition during the pass, but it does not remove the route dependent effect introduced by edge preforming.

For the 45° flange angle, both routes show a more stable response. EFS reaches the wrinkle free range for R2, R4, and R6 under both gap schedules, while EFB remains mainly in the slight wrinkling range. This result indicates that the larger flange angle improves pass level stability, but EFS still provides the most favorable response because it carries a stronger and more distributed curvature band condition into the subsequent pass.

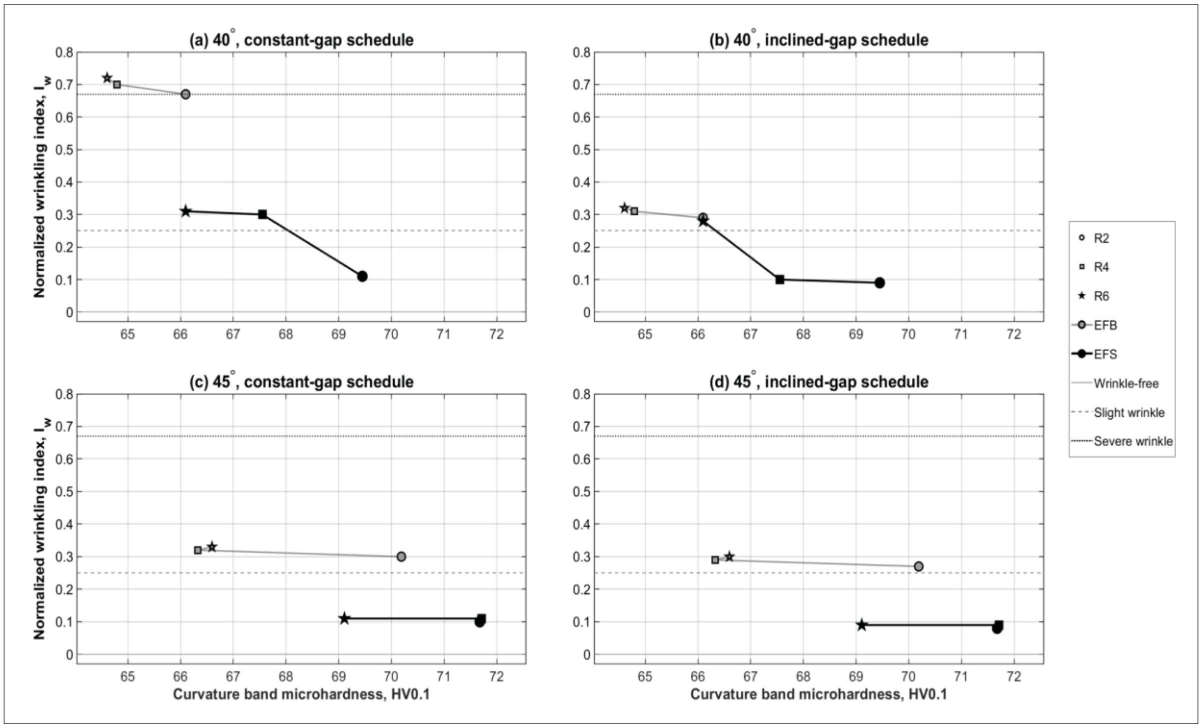

Figure 4.16 Relationship between curvature-band microhardness and normalized wrinkling index during the subsequent spinning pass: (a) 40° constant-gap schedule, (b) 40° inclined-gap schedule, (c) 45° constant-gap schedule, and (d) 45° inclined-gap schedule. The horizontal reference lines indicate the wrinkle-free, slight-wrinkle, and severe-wrinkle class limits. Microhardness is used as the main experimental descriptor of the inherited curvature-band condition, while I_w represents the final pass-level wrinkling response

Figure 4.16 is therefore not a hardness only criterion for wrinkling. Microhardness is an experimental descriptor of retained local strengthening, while the final wrinkling index also depends on pre-strain distribution, flange geometry, gap schedule, and hoop strain recovery. The hoop strain results in Section 4.4.3 support this link because EFS delays the loss of cyclic recovery compared with EFB. Within the investigated material, tooling, geometry, and process window, EFS provides stronger pass level wrinkle suppression than EFB. This finding remains limited to the investigated subsequent spinning pass and does not demonstrate full multi pass conventional spinning formability.

4.5 Discussion

4.5.1 Effect of edge preforming route and backup roller radius on inherited curvature band condition

The inherited curvature band condition is controlled by the combined effect of the edge preforming route and the backup roller radius. Although EFB and EFS both create a flanged edge, the deformation history introduced before the subsequent spinning pass is different. In EFB, the edge is formed mainly by localized bending near the flange root. In EFS, the roller advances along the local surface direction of the backup roller and imposes travelling contact along the edge forming path. Therefore, the visible flange geometry does not fully describe the blank condition carried into the subsequent pass.

The FE strain fields and microhardness measurements show that this route difference changes the mechanical state of the curvature band. EFB produces a localized prestrained zone near the flange root transition, which is consistent with its bending dominated deformation mode. EFS produces a broader conditioned region across the curvature band because the deformation zone moves along the formed edge during roller contact. The hardness measurements follow the same tendency, with EFS generally retaining stronger local strengthening than EFB under comparable flange angle and backup roller radius conditions.

The backup roller radius further modifies the inherited condition. The tested radii R2, R4, and R6 change the local curvature imposed during edge preforming and therefore affect the severity and spatial distribution of the conditioned zone. For EFB, the radius effect is mainly linked to the local bending severity near the flange root. A smaller backup roller radius increases the local curvature demand, whereas a larger radius gives a smoother transition. For EFS, the travelling contact distributes deformation over a larger part of the curvature band, so the difference between routes remains visible across the tested radii.

This combined route and radius effect explains why the preformed blanks cannot be compared only from the final flange angle. The same target flange angle can correspond to different levels and distributions of pre-strain and retained strengthening. The curvature band acts as the transition region between the unsupported rim and the more constrained portion of the blank. Its inherited state therefore affects how the rim responds to repeated circumferential loading and recovery during the subsequent spinning pass.

Within the tested process window, EFS provides the most favourable inherited curvature band condition because it combines higher retained strengthening with a broader prestrained region. EFB still improves the blank condition compared with an unconditioned flat blank, but its deformation remains more concentrated near the flange root. The backup roller radius adjusts the local severity of edge preforming, while the preforming route determines whether the conditioned zone remains localized or extends more broadly through the curvature band. This distinction forms the basis for the route dependent differences in pass level wrinkle suppression discussed in the following sections.

4.5.2 Progressive loss of hoop strain recovery as the mechanism of wrinkle initiation

Wrinkle initiation during the subsequent spinning pass is governed by the progressive loss of hoop strain recovery in the unsupported rim. Under moving roller contact, a rim element is not loaded monotonically. It undergoes repeated contact, strain excursion, unloading, and partial recovery before the next roller passage. For this reason, the maximum compressive hoop strain reached during one cycle does not by itself define the start of instability. A large compressive excursion can still be accommodated when the rim returns close to its previous cyclic reference state. The critical condition begins when the pre-contact hoop strain state shifts progressively from one revolution to the next, indicating that part of the imposed deformation remains stored in the rim.

This mechanism is consistent with the pass resolved hoop strain criterion introduced in Section 4.3.6. The selected rim element is evaluated through the pre-contact, post contact, and next pre-contact states. The contact interval identifies the strain imposed by roller passage, whereas the recovery interval identifies how much of that strain is released before the next cycle. In a stable response, the hoop strain may vary strongly during contact, but the following pre-contact state remains close to a nearly stationary reference level. Wrinkle initiation is identified when this reference state no longer recovers and sustained cycle to cycle drift appears.

Figure 4.14 provides the local evidence for this process. For the representative R6 and 40° condition, the EFB blank shows an earlier loss of cyclic recovery than the EFS blank. In the EFB case, the next pre-contact state does not return to the previous reference level, showing non recovered hoop strain after roller passage. In the EFS case, cyclic recovery is maintained until a later stage of the pass. This delayed drift agrees with the experimental forming states, where EFS shows better wrinkling resistance than the corresponding EFB condition.

Figure 4.15 expresses the same behaviour through the hoop strain recovery ratio. A higher recovery ratio indicates that a larger part of the contact induced hoop strain excursion is recovered before the next roller passage. A reduction in this ratio indicates increasing retention of non recovered deformation in the unsupported rim. The earlier reduction observed for EFB confirms that its rim loses cyclic recovery earlier than EFS. The same tendency appears in the more stable R6 and 45° comparison, supporting the experimental result that EFS remains more resistant to wrinkling under comparable conditions.

The route dependent recovery response is linked to the inherited curvature band condition discussed in Section 4.5.1. EFB creates a more localized prestrained zone near the flange root, whereas EFS produces a broader prestrained and locally strengthened curvature band. This broader conditioned region allows the EFS blank to sustain repeated roller contact over a longer part of the pass before sustained hoop strain drift develops. Therefore, the improved wrinkling resistance of EFS is not explained only by the final flanged shape, but by the mechanical state carried into the subsequent spinning pass.

This analysis also clarifies the role of the final rim profile. The final profile remains the experimental basis for classifying the wrinkling state, but it does not identify when instability starts during the pass. The pass resolved hoop strain history provides this missing temporal information by showing the transition from recoverable cyclic deformation to sustained strain retention. Within the investigated material, geometry, and process window, wrinkle initiation is therefore better described as a progressive loss of rim reversibility than as a direct result of peak compressive hoop strain alone.

4.5.3 Role of flange angle and inclined gap schedule in delaying instability

The experimental results show that flange angle and roller mandrel clearance schedule affect the final rim waviness during the subsequent spinning pass. These two factors mainly modify the support condition applied to the unsupported rim during roller travel. Increasing the target flange angle from 40° to 45° shifts the forming response toward lower wrinkling severity for both EFB and EFS. This trend indicates that a more developed flanged edge provides stronger peripheral support and reduces the tendency of the rim to develop circumferential waviness.

The effect of flange angle is most evident when the 40° and 45° cases are compared under the same preforming route and clearance schedule. At 40°, the rim remains more sensitive to instability, especially for EFB under the constant-gap schedule. At 45°, the response becomes more stable because the flange provides a larger geometric constraint before the subsequent pass begins. However, the increase in flange angle does not make the EFB and EFS responses equivalent. The route used to create the flange still affects the final wrinkling state.

The inclined-gap schedule further reduces rim waviness by increasing local support as the roller advances. Its effect is clearest in the more critical 40° cases, where the constant-gap schedule gives the strongest tendency toward severe wrinkling. Under the inclined-gap schedule, the EFB cases move toward lower wrinkling severity, while the EFS cases approach or maintain the wrinkle-free range. This shows that progressive clearance reduction can delay the growth of rim waviness when the forming condition is close to the wrinkling limit.

The inclined-gap schedule is therefore treated as a clearance variation within the investigated pass. It is not presented as a general toolpath strategy for conventional spinning. Its role here is to modify the local support condition so that the effect of progressive support can be compared with the effect of the inherited preformed state.

The results indicate that flange angle and inclined-gap schedule act as support-related factors. They can delay instability, particularly near the wrinkling limit, but they do not reverse the route-dependent response established by edge preforming. Under comparable flange angle, backup roller radius, and clearance schedule, EFS remains more stable than EFB. This finding is consistent with the broader prestrained and locally strengthened curvature band produced by EFS, which gives the rim greater resistance to the accumulation of non-recovered deformation during the subsequent pass.

4.5.4 Scope of the pass level findings and severe wrinkling morphology

The findings of this study are limited to the wrinkling response observed during the investigated subsequent spinning pass. The tested pass was designed to compare flat, EFB, and EFS blanks under a common toolpath and controlled clearance conditions. Within this framework, a wrinkle free or slight wrinkling classification indicates improved rim stability for the selected pass condition. It does not demonstrate completion of a full conventional spinning route.

This distinction is important because conventional spinning requires both wrinkle control and progressive geometry change over a complete pass sequence. In the present work, cumulative inward material flow, blank diameter reduction, wall thickness evolution over multiple passes, residual stress redistribution after forming, and final part accuracy were not quantified. The results therefore provide evidence of pass level wrinkle suppression, rather than complete process validation for conventional spinning.

The investigated pass is also not treated as a shear spinning forming limit test. Although the roller trajectory follows the conical mandrel direction, the work did not evaluate prescribed wall thickness reduction, sine law thickness evolution, deviation ratio, or shear spinning forming limits. The conical pass was used as a common loading condition for comparing the wrinkling response of the three blank states.

The severe cases shown in Figure 4.13b and Figure 4.13c are classified as critical pass level wrinkling cases, not as successful forming results. Their morphology is best described as severe nonuniform circumferential wrinkling with localized loss of flange stability. This classification is more precise than describing the response as complete workpiece collapse. In spinning, the unsupported rim is loaded by localized moving roller contact rather than by uniform circumferential compression. As a result, small differences in initial geometry, clamping, friction, local thickness, and preforming induced strain can cause some wrinkle peaks to grow faster than others. Once severe waviness develops, the rim no longer maintains a regular circumferential pattern, even though the dominant defect remains flange wrinkling.

The numerical and hardness based analyses are used within the same defined scope. The FE model compares local deformation histories and the loss of hoop strain recovery during the investigated pass. It is not a complete forming limit model. Microhardness mapping describes retained local strengthening in the curvature band, but it does not replace direct measurement of residual stress or the full strain field. Within these limits, the combined evidence shows that edge preforming modifies the blank condition entering the subsequent pass and can reduce wrinkling severity in the selected process window. Extension of this benefit to a complete conventional spinning route requires additional validation of material inflow, diameter reduction, wall thickness evolution, residual stress development, and final geometric accuracy.

4.6 Conclusions

This study examined how the edge preforming route affects the inherited curvature band condition and the subsequent wrinkling response of AA5052-O blanks during one subsequent spinning pass. EFB and EFS were compared using spinning experiments, microhardness mapping, and finite element analysis of hoop strain recovery. The main conclusions are as follows.

- EFB and EFS both modified the flange root and curvature band before the subsequent pass, but they produced different inherited blank conditions. EFB generated a more localized prestrained region near the flange root, while EFS produced a broader conditioned zone through travelling roller contact.

- Microhardness mapping and finite element results showed that EFS generally produced higher retained local strengthening and higher equivalent plastic strain in the curvature band than EFB. This confirms that the visible flange geometry alone is not sufficient to define the blank condition before the subsequent pass.

- The wrinkling classification showed a clear route dependent response within the tested process window. The flat blank was the most critical condition, EFB provided an intermediate improvement, and EFS gave the strongest pass level wrinkle suppression.

- The hoop strain analysis showed that wrinkle initiation was associated with a sustained loss of cyclic recovery rather than the peak compressive hoop strain alone. EFS delayed this loss of recovery more effectively than EFB.

- The inclined gap schedule delayed instability for cases close to the wrinkling limit, but it did not change the route dependent response established by edge preforming.

These findings show that controlling the preforming induced curvature band condition can improve pass level wrinkle suppression. Extension of this benefit to a complete multi-pass conventional spinning route requires separate validation.

4.7 References

[1] Music O, Allwood JM, Kawai K (2010) A review of the mechanics of metal spinning. Journal of Materials Processing Technology 210:3–23. https://doi.org/10.1016/j.jmatprotec.2009.08.021

[2] Xia Q, Shima S, Kotera H, Yasuhuku D (2005) A study of the one-path deep drawing spinning of cups. Journal of Materials Processing Technology 159:397–400. https://doi.org/10.1016/j.jmatprotec.2004.05.027

[3] Wang L, Long H (2011) A study of effects of roller path profiles on tool forces and part wall thickness variation in conventional metal spinning. Journal of Materials Processing Technology 211:2140–2151. https://doi.org/10.1016/j.jmatprotec.2011.07.013

[4] Elizalde S, Coyoy P, Casas C, Puigjaner B, Cabello D, Cabrera JM (2025) Study of the effect of the process parameters on the forming limit in shear spinning processes. The International Journal of Advanced Manufacturing Technology 136:3303–3314. https://doi.org/10.1007/s00170-025-15041-9

[5] Jia Z, Ye T, Han Z, Xiao Y, Ji S (2019) Study on die-less spinning of cone–cylinder combined hollow parts. Journal of Materials Processing Technology 271:488–498. https://doi.org/10.1016/j.jmatprotec.2019.04.028

[6] Russo IM, Cleaver CJ, Allwood JM (2021) Seven principles of toolpath design in conventional metal spinning. Journal of Materials Processing Technology 294:117131. https://doi.org/10.1016/j.jmatprotec.2021.117131

[7] Wu H, Xu W, Shan D, Jin BC (2019) Mechanism of increasing spinnability by multi-pass spinning forming – analysis of damage evolution using a modified GTN model. International Journal of Mechanical Sciences 159:1–19. https://doi.org/10.1016/j.ijmecsci.2019.05.030

[8] Watson M, Long H (2014) Wrinkling failure mechanics in metal spinning. Procedia Engineering 81:2391–2396. https://doi.org/10.1016/j.proeng.2014.10.339

[9] Kobayashi S (1963) Instability in conventional spinning of cones. Transactions of the ASME 85:44–48. https://doi.org/10.1115/1.3667585

[10] Chen SW, Gao PF, Zhan M, Ma F, Zhang HR, Xu RQ (2019) Determination of formability considering wrinkling defect in first-pass conventional spinning with linear roller path. Journal of Materials Processing Technology 265:44-55. https://doi.org/10.1016/j.jmatprotec.2018.10.003

[11] Li ZH, Long H (2022) An analytical model integrated with toolpath design for wrinkling prediction in conventional spinning. Journal of Materials Processing Technology 300:117399. https://doi.org/10.1016/j.jmatprotec.2021.117399

[12] Watson M, Long H, Lu B (2015) Investigation of wrinkling failure mechanics in metal spinning by Box-Behnken design of experiments using finite element method. The International Journal of Advanced Manufacturing Technology 78:981–995. https://doi.org/10.1007/s00170-014-6694-6

[13] Wang L, Long H, Ashley D, Roberts M, White P (2011) Effects of the roller feed ratio on wrinkling failure in conventional spinning of a cylindrical cup. Proceedings of the Institution of Mechanical Engineers, Part B: Journal of Engineering Manufacture 225:1991–2006. https://doi.org/10.1177/0954405410396024

[14] Kong Q, Yu Z, Zhao Y , Wang H, Lin Z (2017) A study of severe flange wrinkling in first-pass conventional spinning of hemispherical part. The International Journal of Advanced Manufacturing Technology 93:3583–3598. https://doi.org/10.1007/s00170-017-0744-9

[15] Gao PF, Yan XG, Li FG, Zhan M, Ma F, Fu MW (2022) Deformation mode and wall thickness variation in conventional spinning of metal sheets. International Journal of Machine Tools and Manufacture 173:103846. https://doi.org/10.1016/j.ijmachtools.2021.103846

[16] Li Z, Long H (2026) Developing a new wrinkling testing method for sheet metal spinning. The International Journal of Advanced Manufacturing Technology 143:6811–6831. https://doi.org/10.1007/s00170-026-17740-3

[17] Ahmed KI, Gadala MS, El-Sebaie MG (2015) Deep spinning of sheet metals. International Journal of Machine Tools and Manufacture 97:72–85. https://doi.org/10.1016/j.ijmachtools.2015.07.005

[18] Yu Z, Zhao Y, Du C, Liu R, Evsyukov SA (2020) Study on flange-constrained spinning process for hemispherical aluminum alloy part. Journal of Materials Processing Technology 278:116515. https://doi.org/10.1016/j.jmatprotec.2019.116515

[19] Nguyen HH, Champliaud H, Le VN (2024) Effect of intermediate path on post-wrinkle initiation of the multi-pass metal spinning process: analysis in the rotating reference frame. Journal of Manufacturing and Materials Processing 8:19. https://doi.org/10.3390/jmmp8010019

[20] Cao Y, Xue Z, Chen X, Raabe D (2008) Correlation between the flow stress and the nominal indentation hardness of soft metals. Scripta Materialia 59:518–521. https://doi.org/10.1016/j.scriptamat.2008.04.039

[21] Wowk D, Pilkey K (2013) An experimental and numerical study of prestrained AA5754 sheet in bending. Journal of Materials Processing Technology 213:1–10. https://doi.org/10.1016/j.jmatprotec.2012.08.002

[22] Tran MV, Champliaud H, Liu Z, Elizalde S, Jahazi M (2026) Wrinkle suppression in metal spinning using flanged-edge blanks: experiments and finite element analysis. The International Journal of Advanced Manufacturing Technology 142:4509–4528. https://doi.org/10.1007/s00170-026-17438-6

[23] Chen SW, Zhan M, Gao PF, Ma F, Zhang HR (2021) A new robust theoretical prediction model for flange wrinkling in conventional spinning. Journal of Materials Processing Technology 288:116849. https://doi.org/10.1016/j.jmatprotec.2020.116849

CHAPTER 5

COMPARATIVE ASSESSMENT OF LOADING-RATE SCALING VERSUS MASS SCALING FOR PREDICTING WRINKLING IN METAL SPINNING

Mai-Van Tran, Sergio Elizalde, Henri Champliaud, Zhaoheng Liu, Mohammad Jahazi

Department of Mechanical Engineering, École de technologie supérieure,
1100 Notre-Dame Ouest, Montréal, Québec, Canada H3C1K3

Article accepted for publication in *Transactions of the Canadian Society of Mechanical Engineering (TCSME)*, March 2026

5.1 Abstract

Explicit dynamic finite element simulations are increasingly used to study defect formation in metal spinning, yet full three-dimensional models remain computationally demanding and often require numerical acceleration. This work compares two widely used acceleration routes in explicit solvers, loading-rate scaling and mass scaling, with emphasis on their influence on wrinkling prediction. An identical process definition and toolpath are implemented in two simulation environments, and the predictions are validated against experiments. Quasi-static fidelity is quantified through the kinetic-to-internal energy ratio, while prediction accuracy is evaluated using the axial force history together with wrinkle-related axial displacement measures, including the axial displacement field at the final stroke position and the peak-to-valley amplitude Δ with peak count. The results show that moderate acceleration, up to a factor of 10 for the present setup, maintains low kinetic contribution and reproduces the experimental force trend and final wrinkle pattern. In contrast, aggressive scaling at a factor of 50 increases inertial contributions, amplifies force deviations, and reduces the reliability of wrinkle predictions. The findings indicate that force histories, interpreted jointly with energy diagnostics and surface metrics, provide a sensitive basis for validation and for selecting acceleration levels in defect-focused spinning simulations. In addition, equal nominal scaling factors do not necessarily correspond to equivalent inertial content when different acceleration mechanisms are used.

Keywords: spinning, rotating reference frame, mass scaling, loading rate, wrinkling

5.2 Introduction

Metal spinning is an incremental rotary forming process used to manufacture thin-walled axisymmetric components with high material utilisation and flexible tooling. Conventional and shear spinning are widely used to form complex shapes through localised deformation under combined compressive and shear stresses, which can improve forming capability for a given material system [1–3]. Despite these advantages, wrinkling remains one of the most persistent defects, especially in passes where compressive circumferential stresses develop in the unsupported flange and interact with bending near the roller contact [2, 3]. Because wrinkling is highly sensitive to boundary conditions, contact constraints, and the evolving stiffness of the deforming region, reliable prediction requires a modelling framework that resolves the transient stress redistribution that precedes and accompanies instability growth [4–7].

Finite element (FE) simulation is therefore a key tool for process understanding and design, but full three-dimensional spinning models remain computationally demanding. The combination of severe contact nonlinearity, large strain, long toolpaths, and small explicit time steps required for stability makes parametric studies expensive, particularly when rotating contact conditions further reduce the stable increment and increase susceptibility to artificial inertia effects [8–14]. This issue is amplified for wrinkling because acceleration can change not only global trends such as force levels, but also instability onset and wrinkle morphology, even when the overall response appears comparable.

To make explicit simulations practical, numerical acceleration is commonly introduced, but it must be applied with care when defect prediction is part of the objective. “Acceleration” refers to numerical techniques used to reduce computational time in explicit simulations by artificially increasing the simulated process rate or the stable time increment, while attempting to preserve quasi-static behavior. So, it does not modify the intended physical process definition. In this work, two acceleration approaches are considered and clearly distinguished. The first is loading-rate scaling (LR), which accelerates the prescribed relative tool motion by reducing the simulated process time while leaving the mass distribution unchanged. The second is mass scaling (MS), which increases the stable explicit time increment by increasing effective inertia in selected regions, thereby reducing the number of increments required. Although both approaches are widely used in incremental forming and spinning, their mechanisms are fundamentally different and equal nominal scaling factors do not imply the same inertial content or the same wrinkling response. For this reason, acceleration levels must be judged using diagnostics and response comparisons rather than the scaling factor alone.

A separate but related modelling choice concerns how the kinematics are represented. In the conventional description, the blank rotates and the roller follows a prescribed axial–radial toolpath (Figure 5.1a). Alternatively, a rotating reference frame (RRF) formulation can reproduce the same relative tool–blank motion while keeping the workpiece stationary and prescribing rotation through the tool motion (Figure 5.1b). This representation can change how rotation and contact updates are handled numerically and therefore must be stated explicitly when interpreting accelerated explicit solutions [15–18]. In the RRF formulation adopted here, LR accelerates the prescribed relative motion in the transformed frame and must not be interpreted as an increase in physical spindle speed.

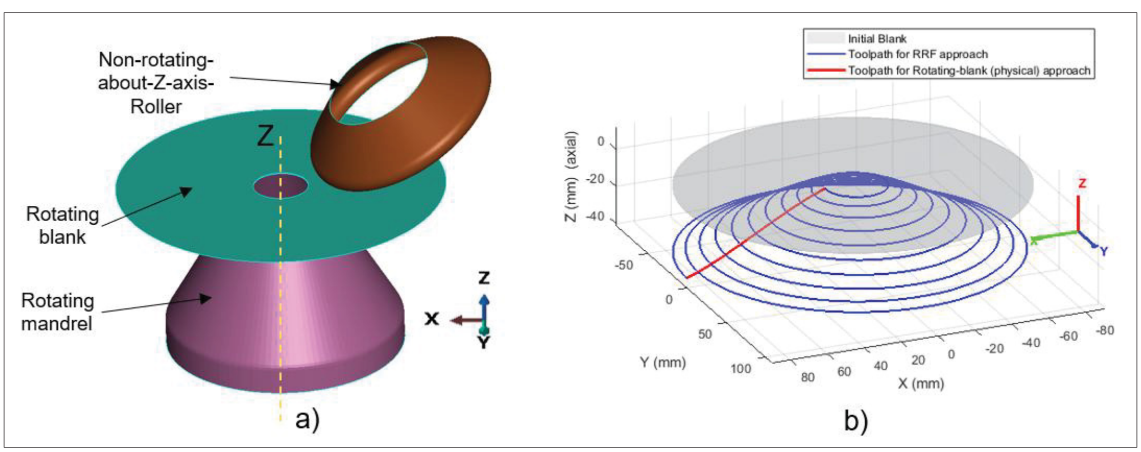

Figure 5.1 (a) Schematic of conventional (physical) spinning and (b) Comparison of toolpaths under RRF and rotating-blank (conventional) kinematic formulations

5.3 Methodology

This study combines explicit three-dimensional FE simulations with a dedicated experimental trial to investigate flange wrinkling during the first pass of conventional spinning. The comparison focuses on wrinkling initiation, the resulting displacement morphology, and the axial force response. It also evaluates how two widely used acceleration approaches in explicit solvers, LR and MS, influence both prediction fidelity and computational efficiency. The experimental and numerical configurations are summarized in Figure 5.2.

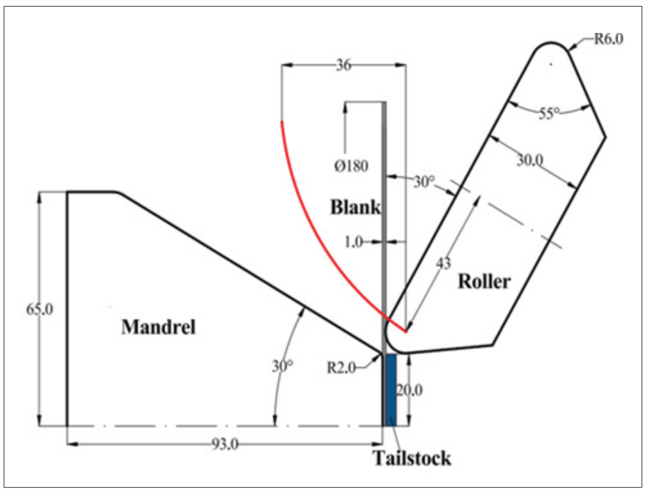

Figure 5.2 Detail of conventional spinning setup for experiment

5.3.1 Study design and scaling matrix

A controlled design matrix is used to evaluate flange wrinkling during the first spinning pass and to quantify how numerical acceleration modifies the stable explicit time increment and the runtime. The numerical goal is to reproduce wrinkling onset and the associated displacement morphology together with the axial force history. Two routes that are commonly used in explicit forming simulations are investigated independently.

LR is applied in LS-DYNA by increasing the prescribed relative motion speed while keeping the physical mass distribution unchanged. For a fixed toolpath length S and a baseline characteristic speed v, the nominal analysis time is

$$T = \frac{S}{v} \tag{5.1}$$

Applying LR with factor α_{LR} increases the imposed speed to

$$v_{LR} = \alpha_{LR}\, v \tag{5.2}$$

so the analysis time becomes

$$T_{LR} = \frac{S}{v_{LR}} = \frac{T_0}{\alpha_{LR}} \tag{5.3}$$

In Eqs. (5.1)–(5.3), S is the total toolpath length associated with the first pass, v is the nominal relative speed used to define the baseline process time, α_{LR} is the LR scaling factor, T_0 is the nominal analysis time, and T_{LR} is the accelerated analysis time. Because the stable explicit time increment is governed primarily by mesh size and material wave speed rather than the imposed process duration, LR reduces the number of increments mainly by shortening the simulated time window. This practice can introduce inertia effects when velocities are increased, which motivates energy-based screening in the present scaling matrix [16].

MS is applied in Abaqus/Explicit by increasing the effective inertia in order to enlarge the stable time increment. In an undamped explicit central difference scheme, stability requires the time increment to remain below a critical threshold that depends on the highest frequencies of the discretized system [15], which can be expressed as

$$\Delta t_{cr} \le \frac{2}{\omega_{\max}} \tag{5.4}$$

where Δt_{cr} is the critical stable time increment and $\omega_{\max}$ is the maximum natural frequency of the discretized system. A useful interpretation follows from the Courant condition, which constrains the stable increment to be smaller than the time required for a dilatational wave to traverse the smallest element dimension (Cocchetti et al. 2013)

$$\Delta t \le \frac{\ell_{\min}}{c_d}. \tag{5.5}$$

In Eq. (5.5), $\ell_{\min}$ is the smallest characteristic element length that controls stability, and c_d is the dilatational wave speed. Using the wave-speed relation adopted introduced here,

$$c_d = \sqrt{\frac{E}{\rho}} \tag{5.6}$$

where E is Young's modulus and ρ is the material density. If MS increases the density in the scaled region by a factor β_{MS}, such that $\rho_{MS} = \beta_{MS}\rho$, then the wave speed decreases to

$$c_{d,MS} = \sqrt{\frac{E}{\rho_{MS}}} = \frac{c_d}{\sqrt{\beta_{MS}}} \tag{5.7}$$

and the stable time increment scales approximately as

$$\Delta t_{MS} \approx \Delta t \sqrt{\beta_{MS}} \tag{5.8}$$

In Eqs. (5.6)–(5.8), β_{MS} is the MS factor applied to density in the selected region, $c_{d,MS}$ is the reduced wave speed after scaling, and Δt_{MS} is the enlarged stable increment. MS can therefore increase the stable time increment efficiently, but it may also alter inertia and dynamic response if applied excessively, which again motivates energy-based checks.

Three scaling levels are examined for each approach, LR = 5, 10, 50 and MS = 5, 10, 50, forming a matched design matrix intended to span from near quasi-static behavior to strongly accelerated conditions. The six cases and the reported Δt_{min} and runtime values are summarized in Table 5.1, together with the solver, acceleration approach, and kinematic formulation.

Table 5.1 Simulation conditions for LR and MS factors

Case ID	Solver	Acceleration approach	Kinematic	Scaling factor	Δt_{min} (s)	Runtime
LDY_LR_5	LS-DYNA	LR	RRF	5	3.5 e-7	28h42’
LDY_LR_10	LS-DYNA	LR	RRF	10	3.5 e-7	17h41’
LDY_LR_50	LS-DYNA	LR	RRF	50	3.5 e-7	4h24’
ABA_MS_5	Abaqus	MS	RRF	5	1.92e-7	55h05’
ABA_MS_10	Abaqus	MS	RRF	10	2.71e-7	42h05’
ABA_MS_50	Abaqus	MS	RRF	50	6.07e-7	17h58’

Energy diagnostics are used as the primary quality screen across the matrix. Monitoring kinetic energy relative to internal energy provides a direct indication of whether inertia becomes dominant. The manuscript adopts the commonly used quasi-static guideline that kinetic energy should remain below roughly 10% of internal energy during the forming stage, and this criterion is applied consistently across all cases.

5.3.2 Finite element model

A three-dimensional explicit model is constructed to reproduce the first spinning pass and to support direct comparison between solvers. The blank is discretized with five integration points through the thickness. The process is defined by a concave toolpath reaching a maximum axial stroke of 36 mm. Material response is represented using an isotropic hardening law in Hollomon form, as given in Eq. (5.9). This choice follows common practice in spinning simulations when the objective is to capture global response and instability trends in the first pass rather than microstructural evolution [2,7]. In the present framework, the Hollomon parameters are calibrated from standard tensile tests before being used in the explicit model [19].

$$\bar{\sigma} = 355\,\varepsilon^{0.29} \tag{5.9}$$

Boundary and loading conditions match the experimental configuration used for validation, with a constrained central region and a free flange where wrinkling develops. Figure 5.1 presents the process geometry and the main modelling features, including the roller path definition and the constrained region, because these conditions directly govern the compressive loading state that promotes flange instability [7–10]. Figure 1b compares the prescribed tool trajectories for the two kinematic descriptions. This side-by-side view clarifies the intended kinematic equivalence while highlighting the modelling distinction that must be considered when interpreting and comparing LR and MS results [16].

In both implementations, the blank is modeled using shell elements with five through thickness integration points and the same discretization to ensure consistent representation of bending and through thickness stress gradients. In LS-DYNA, the blank is discretized using shell element type 26 with hourglass control set to 0.1. Contact interactions between the blank and the tools are defined using a surface-to-surface contact formulation with a Coulomb friction model. Lubricated experimental conditions are represented by assigning low friction coefficients at the interfaces, with a distinction made between mandrel–blank contact and roller–blank contact. The mandrel–blank interface is assigned $\mu = 0.2$ to provide slightly higher friction and limit relative slip of the blank on the mandrel. The interfaces between the blank and the forming roller, and between the blank and the backup roller, are assigned $\mu = 0.01$ to represent well lubricated sliding during forming. In Abaqus Explicit, the same friction coefficients and contact pairs are used to maintain consistent interfacial conditions across solvers.

5.3.3 Acceleration strategies and solver implementation

Two acceleration approaches are examined independently and are not treated as interchangeable, since they modify the numerical time scale through different mechanisms. LR is implemented in LS-DYNA, and MS is implemented in Abaqus/Explicit. Both are used with the same RRF kinematic description so that the intended relative tool–blank motion is defined consistently across solvers. Across both solvers, the process geometry, the prescribed toolpath, the material law, and the mesh are kept identical, while contact enforcement, element formulation and control, and the implementation of MS remain solver dependent.

For LR, the prescribed kinematics are accelerated by multiplying the nominal relative speed v by the LR factor α_{LR}, as defined in Section 5.3.1. This reduces the simulated process duration for the same toolpath length S, while leaving the physical mass distribution unchanged. Because the RRF formulation imposes the relative motion through the tool trajectory, α_{LR} changes the numerical time scale of that prescribed motion and should not be interpreted as a physical increase in spindle speed.

For MS, computational efficiency is increased by enlarging the stable explicit time increment through a controlled increase of effective inertia. The MS factor β_{MS} is applied as a mass increase to raise the stable time increment while maintaining the prescribed relative kinematics in the same RRF description. The square-root dependence of the stable increment on β_{MS} follows directly from the wave-speed argument developed in Section 5.3.1.

To keep reporting consistent across LR and MS, $\Delta t_{\min}$ denotes the minimum stable explicit time increment reported by the solver over the analysis step. This quantity is recorded together with the runtime for each case and is used as a solver-independent indicator of computational gain, while response fidelity is assessed through the same force and wrinkle outputs for all cases. Figure 5.3 summarizes the two solver setups.

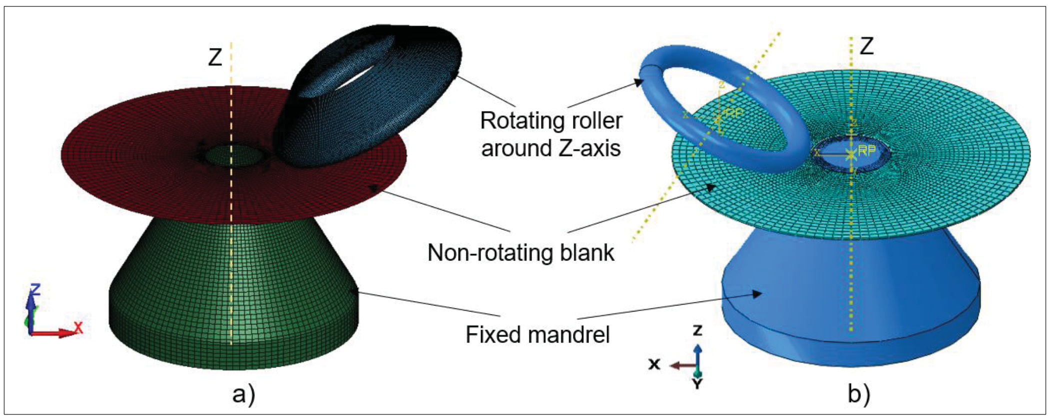

Figure 5.3 FE model and kinematic implementation used in (a) LS-DYNA with LR and (b) Abaqus/Explicit with MS

5.3.4 Mesh strategy

A consistent meshing strategy was adopted in both solvers to enable a direct, solver-to-solver comparison. The blank was discretized using 38 elements along the radial direction with a bias factor of 3.0, and 120 elements in the circumferential direction without bias (Figure 5.4). This resolution was selected to avoid an overly coarse mesh that can mask instability modes, while also limiting excessive refinement that would unnecessarily increase computational cost. The chosen mesh density follows the similar rationale used in [6]. The mesh should be constructed with controlled radial and circumferential subdivisions. It was assessed through a convergence-type strategy, with attention paid to element quality by minimizing aspect ratio so that the solution stabilizes toward the experimental trend. The blank diameter was 180 mm, leading to a large diameter-to-thickness ratio and, consequently, a higher susceptibility to wrinkling. A 30 mm central region was omitted to reduce the total element count without affecting the response, because this inner zone is fully constrained in the simulation. This reduces unnecessary deformable elements in a non-deforming region and helps mitigate excessive element distortion near the inner boundary during the forming pass. Because wrinkling is a bifurcation-sensitive instability, the adopted discretization should be interpreted as a controlled reference mesh for comparing acceleration strategies rather than as proof of strict mesh independence of wrinkle-mode selection.

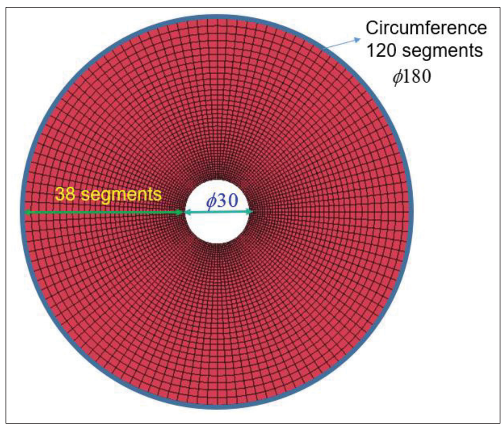

Figure 5.4 Meshing strategy for FE model

5.3.5 Experimental validation

Experiments were conducted on a DENN NTR-25 CNC spinning machine using a setup intended to reproduce the boundary and loading conditions prescribed in the numerical model. The roller followed the same concave toolpath used in the simulations and reached an axial stroke of 36 mm. After forming, the part surface was captured using a laser measurement system and exported as an STL surface for post processing (Figure 5.5a). Wrinkle evaluation used two reference planes, including a plane passing through the axis and center of the part and a bottom reference plane (Figure 5.5b). The circumferential wrinkle profile was extracted from the measured surface, projected onto the measurement reference, and the wrinkle amplitude Δ was defined as the peak-to-valley value of the projected profile (Figure 5.5c).

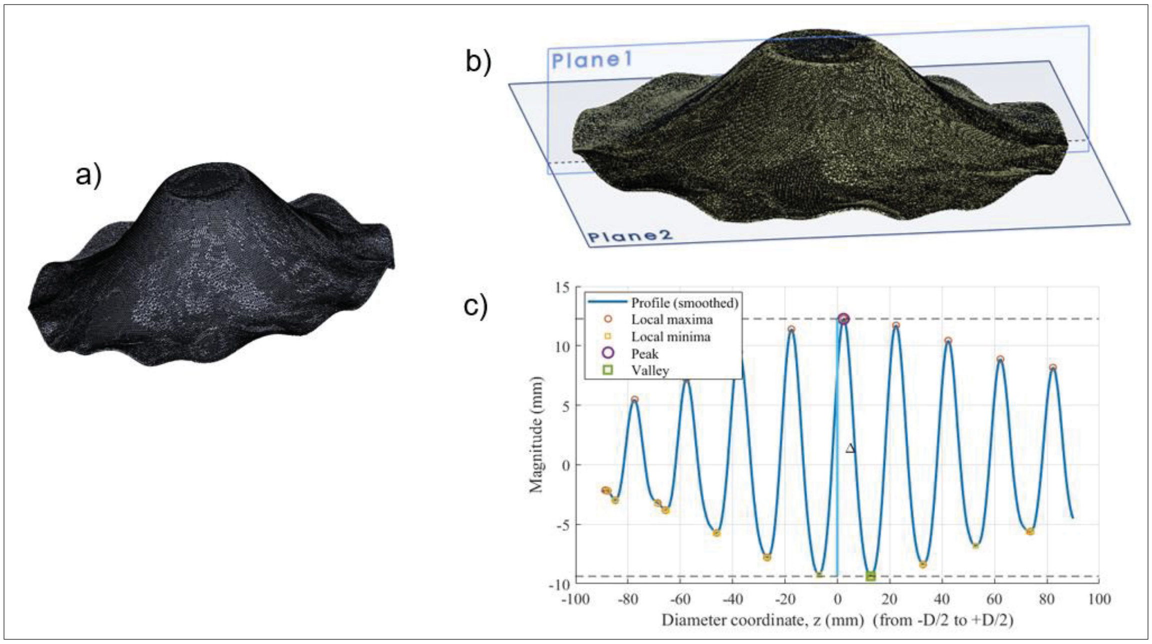

Figure 5.5 Wrinkle measurement procedure, (a) STL surface reconstructed from laser measurement, (b) reference planes used to define the measurement section, and (c) wrinkle amplitude Δ defined as peak–valley of the projected profile

To ensure that differences in Δ and peak count reflect the mechanical response rather than post processing choices, the same profile treatment was applied to simulation and experiment. A rigid offset was removed by subtracting the mean value, then a light circumferential smoothing was applied to reduce measurement noise without altering the dominant wavelength. Wrinkle amplitude was computed from the processed profile as the peak-to-valley range. Peak count was obtained by identifying local maxima along the processed circumferential profile using a consistent prominence-based rule with a minimum spacing criterion. The same peak selection settings were applied for all cases to support direct comparison.

5.4 Results and discussion

The following results build on the observations reported in [19] and extend them through a consistent cross solver comparison against experiments.

5.4.1 Effect of acceleration approach on quasi-static fidelity

A key prerequisite for predicting flange wrinkling with accelerated explicit simulations is to keep inertia secondary to deformation work. Here, quasi-static fidelity is screened using the kinetic to internal energy ratio, with the common guideline that kinetic energy should remain on the order of 10% or less of internal energy during the forming stage.

As shown in Figure 5.6, all cases exhibit a short initial transient near the start of the stroke, where the ratio is elevated because internal energy is still developing while contact and plasticity stabilize. After this early stage, the influence of acceleration becomes clear. For matched moderate scaling, LR5 and MS5 quickly decay to low ratios and remain stable over most of the stroke. A similar behavior is retained at factor 10, where LR10 and MS10 remain close over the main forming interval, indicating that the global energy partition remains compatible with quasi-static response for this setup.

At factor 50, the two approaches separate. LR50 shows a sustained increase in the ratio relative to LR5 and LR10, indicating that aggressive rate increase drives the response toward a more inertia influenced regime. MS50 shows the largest sustained elevation over the pass, confirming that equal nominal factors do not imply comparable inertial content across strategies. Overall, the energy trends support a conservative acceleration window close to 10 for both approaches in the present configuration, since beyond this level kinetic contribution becomes non negligible and the conditions required for reliable wrinkling prediction are progressively lost.

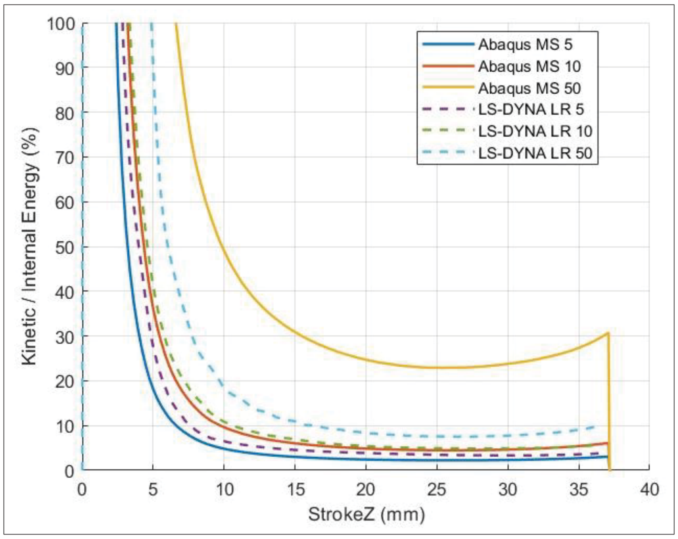

Figure 5.6 Kinetic-to-internal energy ratio along the roller stroke for LR and MS [19]

5.4.2 Axial force response and agreement with experiments

Figure 5.7 compares axial force as a function of roller stroke for all LR and MS cases against the experimental curve. The force rises rapidly at the beginning of the stroke as contact is established and plastic deformation spreads from the roller contact zone. It then reaches a broad maximum and gradually decreases toward the end of the stroke as geometry evolves and the remaining toolpath becomes less resistant. The experimental curve follows the same overall shape with moderate oscillations, which is typical for contact driven incremental forming where local bending and sliding conditions vary continuously.

The moderate acceleration cases provide the closest agreement. LR10 and MS10 reproduce the experimental trend over the full stroke range, including the early rise and the subsequent decay. A small and systematic separation is observed in mid stroke, where MS10 tends to sit slightly above the experimental level and LR10 slightly below. This difference is consistent with the distinct numerical mechanisms behind MS and LR and remains limited at factor 10, without changing the qualitative form of the force evolution.

At factor 50, deviations become pronounced. LR50 shows a strong amplification of the peak force and larger fluctuations during the high force interval, indicating that inertia distorts force transmission and the contact driven structural response under aggressive rate increase. MS50 also elevates the force peak relative to experiment, although its overall decay trend remains closer in shape than LR50. This contrast highlights that apparent curve shape agreement alone is not sufficient. For wrinkling focused studies, the force history must be interpreted together with energy diagnostics, since similar force trends can arise from either quasi-static deformation or inertia influenced response.

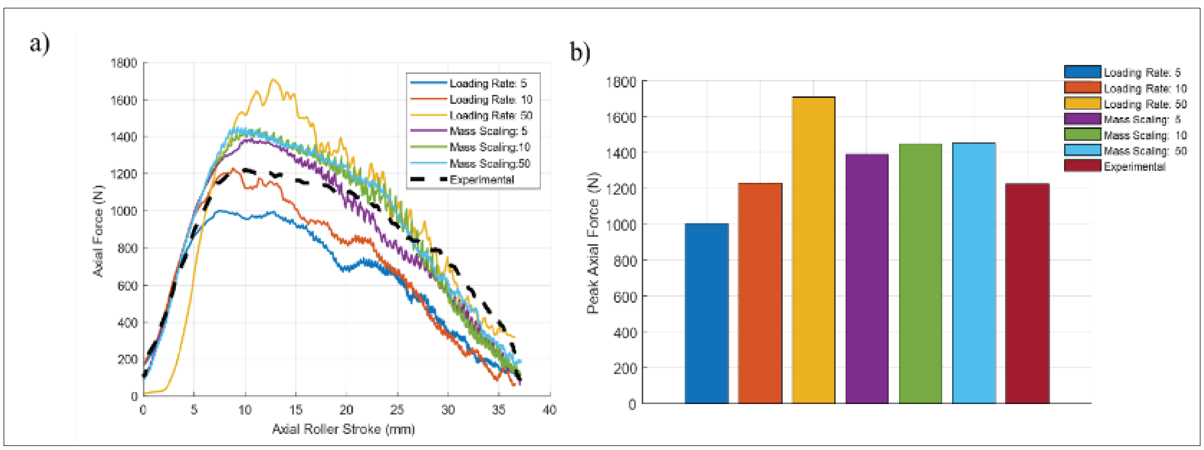

Figure 5.7 Axial force response along the roller stroke, (a) force–stroke curves for LR and MS compared with the experiment, and (b) comparison of peak axial force for each case [19]

The peak force summary in Figure 5.7b reinforces these points. The peak force is more sensitive to extreme LR than to extreme MS, and both LR10 and MS10 remain close to the experimental peak when compared with the much larger spread observed at factor 50. Taken together, the force results support factor 10 as a practical ceiling for reliable response prediction in the present configuration when defect prediction is part of the objective.

5.4.3 Wrinkling onset and displacement morphology

Wrinkling development is assessed using two complementary measures. First, Figure 5.8 tracks the evolution of wrinkle amplitude, Δ, together with the corresponding peak count along the roller stroke for LR10 and MS10. Peak count is extracted from the projected circumferential profile using the same post processing procedure defined in Section 5.3.5, including the smoothing and peak selection settings, so that differences between LR and MS reflect the response rather than case dependent tuning. Second, Figure 5.9 compares the axial displacement field at the final stroke position against the experimentally measured part. The experimental surface is acquired after forming and therefore provides a final state reference for the deformed morphology, whereas the trends in Figure 5.8 are obtained directly from the simulations along the roller stroke, allowing the temporal development of the wrinkle field to be evaluated.

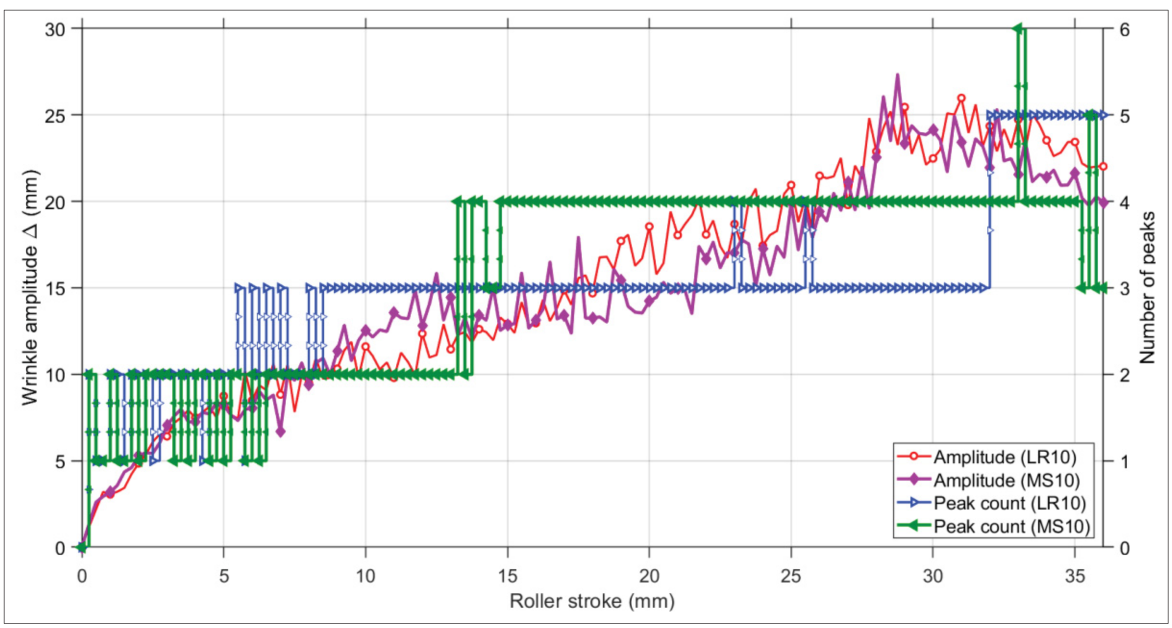

Figure 5.8 Wrinkling onset descriptors versus roller stroke: wrinkle amplitude evolution and corresponding number of peaks between LR10 and MS10

Figure 5.8 indicates that both LR10 and MS10 capture a similar progression of wrinkle severity over most of the toolpath. Following an initial rise early in the stroke, Δ increases progressively as forming proceeds, which is consistent with wrinkling growth in a free flange subjected to circumferential compression and bending as the deformation zone advances. Although the overall growth trend is comparable, the two cases separate near the end of the pass. Both reach their highest amplitudes late in the stroke, but MS10 exhibits a clearer late-stage reduction in Δ, whereas LR10 retains a larger residual amplitude at the final position. This behavior shows that wrinkle severity does not necessarily increase monotonically, and that changes in geometry and contact conditions during the pass can partially smooth the flange once wrinkles have formed.

Peak count adds further resolution to this comparison. LR10 shows a limited number of step changes before stabilizing, while MS10 reaches a higher peak count earlier, remains elevated for much of the stroke, and then undergoes additional late-stage changes, including a reduction near the end of the stroke. These stepwise variations are consistent with circumferential mode adjustments as flange stiffness and geometry evolve. The late- stage reduction in peak count for MS10 coincides with the reduction in Δ, and this combination also increases the sensitivity of peak detection because shallow undulations can merge or become indistinguishable in the projected profile even when a periodic pattern is still visible in the full field. For this reason, Δ and peak count are interpreted together when comparing accelerated simulations. To mitigate post processing sensitivity when amplitudes are small, the same filtering and peak prominence settings are applied across cases and robustness is checked by varying the smoothing window.

Figure 5.9 provides a final state morphology comparison that complements the stroke based trends. The experiment shows a circumferentially periodic displacement pattern concentrated near the free flange, with a smoother response in the constrained central region. Both LR10 and MS10 reproduce this dominant morphology, including the localization near the edge and the overall periodicity, indicating that both accelerated simulations capture the region that is most prone to instability and the principal wrinkle layout. The remaining differences are primarily quantitative. In line with the late-stage divergence observed in Figure 5.8, MS10 shows stronger circumferential waviness than LR10, while LR10 appears slightly attenuated relative to the experiment. Taken together with the energy and force diagnostics presented in Sections 5.4.1 and 5.4.2, these results support the interpretation that modest differences in inertial contribution and stress redistribution at the same nominal factor can translate into noticeable differences in wrinkle growth and late-stage smoothing once the wrinkle field is fully developed.

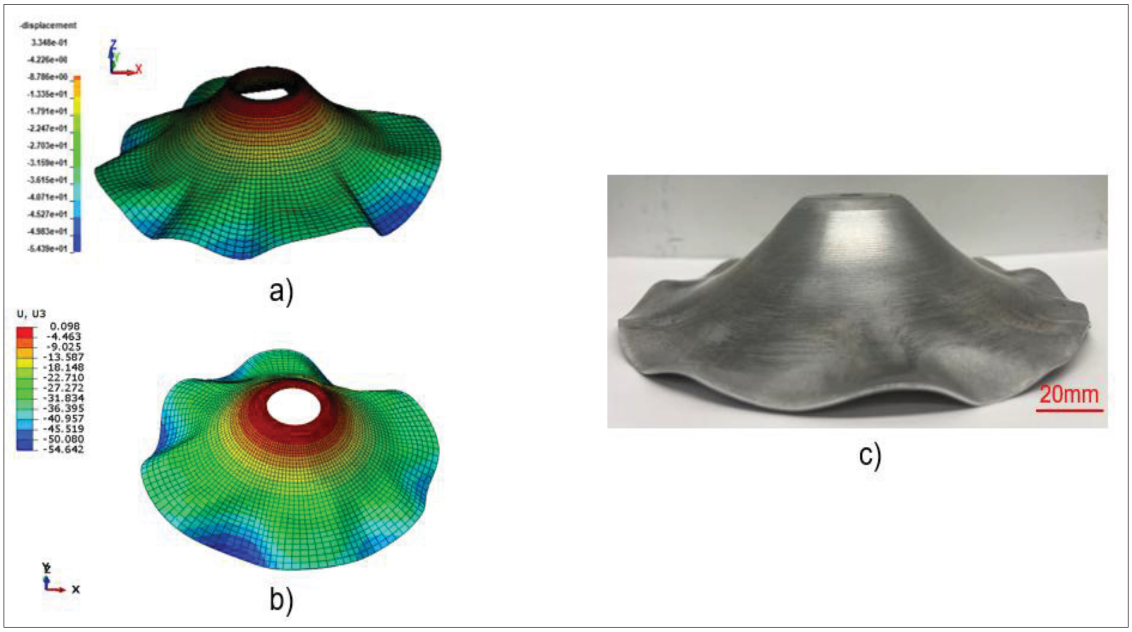

Figure 5.9 Simulation results showing the axial displacement field at the end of stroke (a) LR 10, (b) MS 10, and (c) sample obtained from the experimental trial

Although the present analysis is limited to the first pass of conventional spinning, the main numerical implication is broader for incremental rotary forming. In processes such as power spinning or flow forming, explicit simulations are likewise governed by the balance between computational efficiency and artificial inertia when numerical acceleration is introduced. The present results therefore suggest that loading-rate scaling and mass scaling should not be regarded as equivalent solely because they share the same nominal factor; their acceptability should instead be judged from combined energy, force, and surface-morphology diagnostics. At the same time, the quantitative threshold identified here should not be transferred directly to other processes or configurations, since differences in thickness reduction, material flow, boundary support, and solver implementation can modify both inertia sensitivity and defect development. In addition, because wrinkling is a bifurcation-sensitive instability, the present comparison should be understood as applying to the adopted discretization and process definition, and a broader mesh-sensitivity assessment would be useful in future work to examine the influence of mesh density and topology on wrinkle-mode selection.

5.5 Conclusion

This study compared two common acceleration strategies for explicit three-dimensional metal spinning simulation, namely loading-rate scaling in LS-DYNA and mass scaling in Abaqus/Explicit, under the same process definition and a common rotating-reference-frame interpretation. The simulations were evaluated against experiments using the kinetic-to-internal-energy ratio, axial force history, and wrinkle-related displacement measures.

The results show that acceleration must remain moderate when wrinkling prediction is required. For scaling factors up to 10, both approaches preserved acceptable quasi-static fidelity and reproduced the main experimental trends in axial force and final wrinkle pattern. Under the present configuration, a factor of 10 therefore represents a practical upper limit for achieving computational gain without losing meaningful defect prediction capability.

At a factor of 50, inertial effects became significant and the numerical response departed from the experiments. The force history became distorted, and the wrinkle-related displacement field became less reliable because instability development was increasingly influenced by dynamic effects. The results also show that equal nominal scaling factors in loading-rate scaling and mass scaling do not imply equivalent inertial content or equivalent wrinkling outcomes.

Overall, force history is a robust primary validation metric, while wrinkle amplitude and peak count provide useful complementary indicators once the global loading response is captured. The present conclusions are limited to the adopted geometry, material, toolpath, and discretization. Extension to other forming configurations and related incremental rotary processes remains an important topic for future work.

5.6 References

[1] Music, O., Allwood, J.M., Kawai, K. (2010). A review of the mechanics of metal spinning. *Journal of Materials Processing Technology*, 210(1), 3–23. https://doi.org/10.1016/j.jmatprotec.2009.08.021

[2] Wong, C.C., Dean, T.A., Lin, J. (2003). A review of spinning, shear forming and flow forming processes. *International Journal of Machine Tools and Manufacture*, 43, 1419–1435.

https://doi.org/10.1016/S0890-6955(03)00172-X

[3] Xia, Q., Xiao, G., Long, H., Cheng, X., Sheng, X. (2014). A review of process advancement of novel metal spinning. *International Journal of Machine Tools and Manufacture*, 85, 100–121. https://doi.org/10.1016/j.ijmachtools.2014.05.005

[4] Kobayashi, S. (1963). Instability in conventional spinning of cones. *Transactions of the ASME, Journal of Engineering for Industry*, 85(1), 44–48. https://doi.org/10.1115/1.3667585

[5] Kawka, M., Olejnik, L., Rosochowski, A., Sunaga, H., Makinouchi, A. (2001). Simulation of wrinkling in sheet metal forming. *Journal of Materials Processing Technology*, 109, 283–289. https://doi.org/10.1016/S0924-0136(00)00813-X

[6] Nguyen, H.H., Champliaud, H., Le, V.N. (2024). Effect of intermediate path on post wrinkle initiation of the multi pass metal spinning process, analysis in the rotating reference frame. *Journal of Manufacturing and Materials Processing*, 8(1), 19.

https://doi.org/10.3390/jmmp8010019

[7] Watson, M., Long, H., Lu, B. (2015). Investigation of wrinkling failure mechanics in metal spinning by Box Behnken design of experiments using finite element method. *International Journal of Advanced Manufacturing Technology*, 78, 981–995. https://doi.org/10.1007/s00170-014-6694-6

[8] Quigley, E., Monaghan, J. (2002). Enhanced finite element models of metal spinning. *Journal of Materials Processing Technology*, 121, 43–49. https://doi.org/10.1016/S0924-0136(01)01138-4

[9] Sebastiani, G., Brosius, A., Ewers, R., Kleiner, M., Klimmek, C. (2006). Numerical investigation on dynamic effects during sheet metal spinning by explicit finite element analysis. *Journal of Materials Processing Technology*, 177, 401–403.

https://doi.org/10.1016/j.jmatprotec.2006.04.080

[10] Rentsch, B., Manopulo, N., Hora, P. (2017). Numerical modelling, validation and analysis of multi pass sheet metal spinning processes. *International Journal of Material Forming*, 10, 641–651. https://doi.org/10.1007/s12289-016-1308-5

[11] Essa, K., Hartley, P. (2009). Numerical simulation of single and dual pass conventional spinning processes. *International Journal of Material Forming*, 2(4), 271–281.

https://doi.org/10.1007/s12289-009-0602-x

[12] Ablat, M.A., Qattawi, A. (2017). Numerical simulation of sheet metal forming, a review. *International Journal of Advanced Manufacturing Technology*, 89, 1235–1250. https://doi.org/10.1007/s00170-016-9103-5

[13] Awiszus, B., Härtel, S. (2011). Numerical simulation of non circular spinning, a rotationally non symmetric spinning process. *Production Engineering Research and Development*, 5(6), 605–612. https://doi.org/10.1007/s11740-011-0335-9

[14] Keneshlou, M., Biglari, F.R., Shafaie, M. (2023). A numerical and experimental analysis of noncircular blank spinning. *Journal of Manufacturing Processes*, 94, 159–182 https://doi.org/10.1016/j.jmapro.2023.03.045

[15] Cocchetti, G., Pagani, M., Perego, U. (2013). Selective MS and critical time step estimate for explicit dynamics analyses with solid shell elements. *Computers and Structures*, 127, 39–52. https://doi.org/10.1016/j.compstruc.2012.10.021

[16] Korolakina, A-E.C., Bouchard, P-O., Mocellin K., Veen S.V.D., Lepied, A. (2025). Assessment of tool kinematics, MS effects, and similarity theory in metal spinning simulation. *Journal of Manufacturing Processes*, 151, 234–250. https://doi.org/10.1016/j.jmapro.2025.06.069

[17] Zhai, Z., Zhan, M., Shi, Z., Dong, Y., Fan, X. (2025). Acceleration of sheet metal spinning simulation by multi mesh method. *Chinese Journal of Aeronautics*. 38(7), 103251. https://doi.org/10.1016/j.cja.2024.09.027

[18] Suresh, K., Regalla, S.P. (2014). Effect of time scaling and mass scaling in numerical simulation of incremental forming. *Applied Mechanics and Materials*, 612, 105–110. https://doi.org/10.4028/www.scientific.net/AMM.612.105

[19] Tran, M.-V., Elizalde, S., Champliaud, H., Liu, Z., Jahazi, M. (2025). *Wrinkling prediction in metal spinning through numerical simulation: impact of loading rate and mass scaling*. Proceedings of the CSME-CFDSC-CSR 2025 Congress, May 25–28, Montréal, Québec, Canada. https://espace2.etsmtl.ca/id/eprint/32515/

[20] Tran, M.-V., Champliaud, H., Liu, Z., Elizalde, S., Jahazi, M. (2026). Wrinkle suppression in metal spinning using Flanged-Edge blanks: experiments and finite element analysis. *Int J Adv Manuf Technol* 142, 4509–4528. https://doi.org/10.1007/s00170-026-17438-6

CONCLUSION

In this thesis, controlled experiments and three-dimensional explicit finite element simulations were combined to investigate flange wrinkling during the first pass of conventional metal spinning and to evaluate an edge-preforming route aimed at improving stability without changing the final forming objective. The work uses consistent evidence sources across the studies, including surface geometry measurements for defect characterization and microhardness mapping for reconstructing the prestrain and strengthening footprint introduced by the edge conditioning step. The main conclusions are summarized below in four complementary aspects.

1. Edge preforming as a practical route for suppressing first-pass flange wrinkling

The thesis confirms that conditioning the blank edge prior to conventional spinning can significantly delay or suppress the circumferential buckling modes that develop in the unsupported rim during the first pass. When the spinning conditions are kept comparable, a pre-formed flanged edge provides a markedly more stable response than a flat edge. This improvement is consistent with the role of rim rigidity in governing instability, since geometric reinforcement shifts material farther from the neutral axis and increases the resistance of the rim to out-of-plane deformation. The thesis also shows that the stabilizing effect is not generic but depends on the selected edge geometry, and in particular on the parameters that control the added rigidity, such as flange angle and flange length.

2. Mechanical reinforcement through controlled edge pre-straining and its measurable footprint

Beyond geometric reinforcement, the thesis demonstrates that edge preforming introduces a strengthened band at the flange root that can be treated as an engineered stiffness field rather than as a secondary shaping step. Two edge pre-straining routes are examined under comparable objectives, namely edge forming by bending and edge forming by spinning. Both routes increase hardening near the outer flange and generate a distinct strengthened curvature band, but they do so with different spatial signatures. The edge forming by spinning route produces a stronger and wider hardened region than bending, indicating that the strain path and the affected material volume are different even when the final geometry is similar. These differences justify the use of compact descriptors of the curvature-band strengthening to compare preforming conditions and to support a mechanistic interpretation of wrinkling sensitivity in the subsequent spinning pass.

3. A consistent experimental and numerical framework for connecting process design to wrinkling response

A central methodological outcome of the thesis is the use of a consistent framework to connect process design, prestrain history, and wrinkling response. Experimentally, wrinkling is treated as a measurable surface instability rather than a qualitative observation, and surface geometry measurements are used to support direct comparisons across conditions. In parallel, explicit three-dimensional FE simulations are used not only to reproduce final shapes, but also to extract histories of stress and strain in rim-relevant locations and to interpret how preforming modifies the transient loading path that precedes instability. Taken together, the combined approach provides a coherent basis for linking edge conditioning choices to first-pass stability outcomes using evidence that remains consistent across chapters.

4. Numerical acceleration and its influence on defect-focused prediction reliability

Because explicit spinning simulations are computationally demanding, the thesis includes a focused assessment of numerical acceleration practices when the objective is defect prediction. The comparison between loading-rate scaling and mass scaling shows that moderate acceleration can preserve quasi-static fidelity and maintain reliable wrinkling predictions, while overly aggressive acceleration increases inertial influence and reduces the reliability of predicted wrinkle morphology even when some global measures appear acceptable. The thesis further shows that judging acceleration levels requires more than checking force trends alone, and that energy diagnostics interpreted together with surface and displacement-based wrinkle metrics provide a more sensitive and defensible validation basis for defect-focused simulations.

Overall, the thesis establishes experimentally anchored guidance for designing edge-conditioned blanks to improve first-pass stability in conventional spinning and provides a validated set of analysis tools to interpret wrinkling through coupled geometry, strengthening footprint, and stress–strain history evidence.

RECOMMENDATIONS

The following research directions are suggested to extend the contributions of this thesis and to strengthen both process design guidance and defect-prediction practice.

1. Extension of the stability map to broader geometries and material conditions

Future work should extend the edge-conditioning design space beyond the current family of axisymmetric geometries and the investigated material condition. Systematic variation of blank size and thickness, alloy temper, and forming severity would help generalize the stability trends and clarify how edge reinforcement competes with other limiting mechanisms such as thinning or local damage when the process window is expanded.

2. Optimization-oriented design of edge geometry conditioning

While the thesis demonstrates the strong influence of flange geometry on stability, future studies could develop optimization-oriented design maps that balance stability improvement with practical constraints such as manufacturability, dimensional tolerances, and downstream forming requirements. This includes exploring multi-stage edge shaping routes and assessing how preformed edge geometry interacts with toolpath choices in the subsequent spinning pass.

3. Deeper linkage between prestrain footprints, residual fields, and instability evolution

Microhardness mapping provides a practical indicator of strengthening and an accessible way to reconstruct a spatial prestrain footprint. Future work should complement this approach with additional characterization of residual stress and through-thickness gradients to better isolate how the combined residual and hardening fields influence strain recovery, stress redistribution, and instability evolution during spinning. This would also support stronger mechanistic discrimination between edge pre-straining routes.

4. Defect-focused best practices for accelerated explicit simulations

The acceleration assessment in this thesis motivates a broader set of defect-focused modelling guidelines. Future work should evaluate additional diagnostics and scaling strategies, including localized or adaptive acceleration schemes, and establish clearer acceptance criteria that remain robust across solvers and kinematic formulations. Particular emphasis should remain on practices that preserve wrinkle morphology and onset sensitivity rather than only matching global force histories.

5. Toward reduced-order predictive criteria supported by validated simulations

Finally, the combined experimental and simulation evidence developed in this thesis provides a strong foundation for reduced-order predictive criteria that can be used for process planning. Future work should aim to translate the observed relationships between edge rigidity, strengthened curvature-band descriptors, and wrinkling outcomes into practical predictive maps that can support rapid design decisions without requiring full three-dimensional simulations for every candidate condition.

LIST OF BIBLIOGRAPHICAL REFERENCES

1. Website https://globalmetalspinning.com (Figure 1.1)
2. Runge M, "*Spinning and flow forming"* [Pollitt DH, Trans.]. Leifield GmbH; 1994. (Figure 1.2)
3. Wang, L., Long, H., Ashley, D., Roberts, M., White, P., "*Effects of the roller feed ratio on wrinkling failure in conventional spinning of a cylindrical cup*," Proceedings of the Institution of Mechanical Engineers, Part B: Journal of Engineering Manufacture, 225(11) (2011) 1991–2006. (Figure 1.3)

BIBLIOGRAPHY

Belytschko, T., Liu, W.K., Moran, B. *Nonlinear Finite Elements for Continua and Structures*. Wiley (2000).

Chen, S.W., Zhan, M., Gao, P.F., Ma, F., Zhang, H.R. A new robust theoretical prediction model for flange wrinkling in conventional spinning. *Journal of Materials Processing Technology* 288 (2021) 116849. https://doi.org/10.1016/j.jmatprotec.2020.116849

Gao, P.F., Yan, X.G., Li, F.G., Zhan, M., Ma, F., Fu, M.W. Deformation mode and wall thickness variation in conventional spinning of metal sheets. *International Journal of Machine Tools and Manufacture* 173 (2022) 103846. https://doi.org/10.1016/j.ijmachtools.2021.103846

Suresh, K., Regalla, S.P. (2014). Effect of time scaling and mass scaling in numerical simulation of incremental forming. *Applied Mechanics and Materials*, 612, 105–110. https://doi.org/10.4028/www.scientific.net/AMM.612.105

Kobayashi, S. Instability in conventional spinning of cones. *Journal of Engineering for Industry* 85 (1963) 44–48. https://doi.org/10.1115/1.3667585

Kong, Q., Yu, Z., Zhao, Y., Wang, H., Lin, Z. A study of severe flange wrinkling in first pass conventional spinning of hemispherical part. *International Journal of Advanced Manufacturing Technology* 93 (2017) 3583–3598. https://doi.org/10.1007/s00170-017-0744-9

Korolakina, A-E.C., Bouchard, P-O., Mocellin K., Veen S.V.D., Lepied, A. (2025). Assessment of tool kinematics, mass scaling effects, and similarity theory in metal spinning simulation. *Journal of Manufacturing Processes*, 151, 234–250. https://doi.org/10.1016/j.jmapro.2025.06.069

Li, Z.H., Long, H. An analytical model integrated with toolpath design for wrinkling prediction in conventional spinning. *Journal of Materials Processing Technology* 300 (2022) 117399. https://doi.org/10.1016/j.jmatprotec.2021.117399

Music, O., Allwood, J.M., Kawai, K. A review of the mechanics of metal spinning. *Journal of Materials Processing Technology* 210 (2010) 3–23. https://doi.org/10.1016/j.jmatprotec.2009.08.021

Tran, M.V., Champliaud, H., Liu, Z., Elizalde, S., Jahazi, M. Wrinkle suppression in metal spinning using flanged edge blanks: experiments and finite element analysis. *International Journal of Advanced Manufacturing Technology* 142 (2026) 4509–4528. https://doi.org/10.1007/s00170-026-17438-6

Wang, L. Analysis of material deformation and wrinkling failure in conventional metal spinning process. PhD thesis, Durham University (2012), https://etheses.durham.ac.uk/id/eprint/3537/

Wong, C.C., Dean, T.A., Lin, J. A review of spinning, shear forming and flow forming processes. *International Journal of Machine Tools and Manufacture* 43 (2003) 1419–1435. https://doi.org/10.1016/S0890-6955(03)00172-X

Xia, Q., Xiao, G., Long, H., Cheng, X., Sheng, X.. A review of process advancement of novel metal spinning. *International Journal of Machine Tools and Manufacture* 85 (2014) 100–121. https://doi.org/10.1016/j.ijmachtools.2014.05.005

Yu, Z., Zhao, Y., Du, C., Liu, R., Evsyukov, S.A. Study on flange constrained spinning process for hemispherical aluminum alloy part. *Journal of Materials Processing Technology* 278 (2020) 116515. https://doi.org/10.1016/j.jmatprotec.2019.116515

LIST OF PUBLICATIONS

International journals

Tran, MV., Champliaud, H., Liu, Z., Elizalde S., Jahazi, M., Wrinkle suppression in metal spinning using Flanged-Edge blanks: experiments and finite element analysis. *Int J Adv Manuf Technol* 142, 4509–4528 (2026). https://doi.org/10.1007/s00170-026-17438-6

International conferences

Tran, Mai-Van, Elizalde, Sergio, Champliaud, Henri, Liu, Zhaoheng and Jahazi, Mohammad. 2025. « Wrinkling prediction in metal spinning through numerical simulation: Impact of loading rate and mass scaling ». In *Proceedings of the CSME-CFDSC-CSR 2025 International Congress* (Montreal, QC, Canada, May 25-28, 2025) Coll. « Progress in Canadian Mechanical Engineering », vol. 8.